

# COMPARING UNSTABLE CISLUNAR ORBITS FOR EFFICIENT TRANSFERS TO DEEP-SPACE TARGETS

by

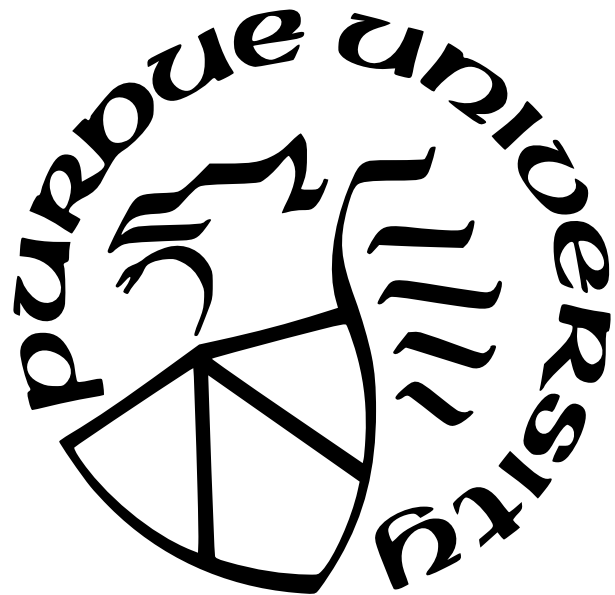
**Jonathan Richmond**

A Thesis

*Submitted to the Faculty of Purdue University*

*In Partial Fulfillment of the Requirements for the degree of*

Master of Science in Aeronautics and Astronautics



School of Aeronautics and Astronautics

West Lafayette, Indiana

December 2024

**THE PURDUE UNIVERSITY GRADUATE SCHOOL  
STATEMENT OF COMMITTEE APPROVAL**

**Dr. Kathleen C. Howell, Chair**

School of Aeronautics and Astronautics

**Dr. Carolin Frueh**

School of Aeronautics and Astronautics

**Dr. Kenshiro Oguri**

School of Aeronautics and Astronautics

**Approved by:**

Dr. Gregory A. Blaisdell

ADD DEDICATION

## **ACKNOWLEDGMENTS**

ADD ACKNOWLEDGEMENTS

## TABLE OF CONTENTS

LIST OF TABLES . . . . .	8
LIST OF FIGURES . . . . .	9
LIST OF SYMBOLS . . . . .	12
ABBREVIATIONS . . . . .	16
ABSTRACT . . . . .	17
1 INTRODUCTION . . . . .	18
1.1 Motivation . . . . .	18
1.2 Research Objectives . . . . .	19
1.3 Previous Contributions . . . . .	21
1.4 Overview of Current Work . . . . .	23
2 DYNAMICAL MODELS . . . . .	25
2.1 Coordinate Frames . . . . .	25
2.1.1 Barycentric Rotating and Inertial Frames . . . . .	25
2.1.2 The Ecliptic J2000 Primary-Centered Inertial Frame . . . . .	26
2.2 The Two-Body Problem . . . . .	27
2.2.1 Equations of Motion . . . . .	27
2.2.2 Conic Sections . . . . .	29
2.2.3 Keplerian Orbital Elements . . . . .	30
Cartesian state to Keplerian orbital elements . . . . .	30
Keplerian orbital elements to Cartesian state . . . . .	32
2.2.4 Kepler's Equation . . . . .	33
2.3 The Circular Restricted Three-Body Problem . . . . .	34
2.3.1 Equations of Motion . . . . .	34
2.3.2 Nondimensionalized Values . . . . .	36
2.3.3 Equilibrium Points . . . . .	37
2.3.4 Jacobi Constant . . . . .	37
2.4 Patched Dynamical Models . . . . .	38
2.4.1 The Patched 2BP-CR3BP Model . . . . .	39
2.4.2 The Blended CR3BP Model . . . . .	40
2.5 Coordinate Frame Transformations . . . . .	42
2.5.1 Barycentric Rotating Frame - Primary-Centric Arbitrary Inertial Frame . . . . .	42
2.5.2 Barycentric Rotating Frame - Ecliptic J2000 Inertial Frame . . . . .	44
3 CR3BP DYNAMICAL STRUCTURES . . . . .	46
3.1 Differential Corrections . . . . .	46
3.1.1 State Transition Matrix . . . . .	46
3.1.2 Multi-Variable Newton-Raphson Method . . . . .	48
3.1.3 Central Difference Method . . . . .	49
3.2 Periodic Orbits . . . . .	50

3.2.1	Lyapunov Orbits . . . . .	51
	A Lyapunov Targeter . . . . .	51
	Lyapunov Initial Guess . . . . .	52
	Converged Lyapunov Orbit . . . . .	53
	Natural Parameter Continuation . . . . .	54
3.2.2	Orbital Stability . . . . .	55
	Monodromy Matrix . . . . .	55
	Stability Index . . . . .	56
	Time Constant . . . . .	57
	Bifurcations . . . . .	58
	New Family Generation from Bifurcation . . . . .	59
3.2.3	Halo Orbits . . . . .	59
	A Halo Targeter . . . . .	59
	Converged Halo Families . . . . .	60
3.2.4	Butterfly Orbits . . . . .	61
3.2.5	Axial Orbits . . . . .	63
	An Axial Targeter . . . . .	63
	Converged Axial Families . . . . .	64
3.2.6	Vertical Orbits . . . . .	64
	A Vertical Targeter . . . . .	64
	Converged Vertical Families . . . . .	65
3.2.7	Equilateral Long Period Orbits . . . . .	67
	A Planar Equilateral Orbit Targeter . . . . .	67
	Equilateral Long Period Orbit Initial Guess . . . . .	69
	Converged Equilateral Long Period Orbit Families . . . . .	70
3.2.8	Equilateral Axial Orbits . . . . .	70
	A Spatial Equilateral Orbit Targeter . . . . .	70
	Converged Equilateral Axial Families . . . . .	71
3.2.9	Resonant Orbits . . . . .	72
	Converged 2:1a Resonant Orbit Family . . . . .	72
	Converged 3:4 Resonant Orbit Family . . . . .	73
3.3	Invariant Manifolds . . . . .	73
3.3.1	Approximating a Manifold Arc . . . . .	75
3.3.2	Manifold Time-of-Flight . . . . .	78
3.4	Poincaré Maps . . . . .	79
4	CISLUNAR-MARS TRAJECTORY CONSTRUCTION . . . . .	81
4.1	Near-Ballistic Transfers between the Earth-Moon and Sun-Earth Systems . .	81
4.1.1	Methodology . . . . .	82
4.1.2	Example . . . . .	85
4.2	The Moon-to-Moon Analytical Transfer Method . . . . .	86
4.2.1	Methodology . . . . .	87
4.2.2	Example . . . . .	93
4.3	End-to-End Transfers . . . . .	96
4.3.1	"Direct" Transfers . . . . .	96

4.3.2	Transfers with Staging Orbit . . . . .	97
4.3.3	Transfer Tradespace . . . . .	99
4.4	Keplerian Hohmann Transfer . . . . .	99
5	CISLUNAR DEPARTURE ORBIT COMPARISON . . . . .	105
5.1	Comparing Transfers via Intermediate Sun-Earth Halos to Direct Transfers .	105
5.1.1	Cost Function . . . . .	105
5.1.2	Comparison of Selected Transfers . . . . .	107
5.2	Comparing Cislunar Departure Families . . . . .	107
5.3	Comparison to Previous Work . . . . .	107
6	CONCLUSION . . . . .	108
	REFERENCES . . . . .	109
A	End-to-End Transfer Tradespaces . . . . .	114
A.1	Lyapunov Orbits . . . . .	114

## LIST OF TABLES

2.1	Characteristic values of relevant CR3BP systems. . . . .	36
3.1	Manifold-related values of relevant CR3BP systems. . . . .	77
4.1	MMAT sphere of influence radii of relevant CR3BP systems. . . . .	88

## LIST OF FIGURES

2.1	Barycentric rotating and inertial frames in a CR3BP system. . . . .	26
2.2	Earth-centered Ecliptic J2000 inertial frame. . . . .	27
2.3	Two-body problem in a barycentric inertial frame. . . . .	28
2.4	Orientation and location along an orbit in an inertial frame using Keplerian orbital elements. . . . .	31
2.5	Definition of eccentric anomaly and the auxiliary circle. . . . .	32
2.6	CR3BP barycentric rotating frame with Lagrange points. . . . .	37
2.7	<i>XY</i> -Projection of the Patched 2BP-CR3BP Model . . . . .	40
2.8	Patched 2BP-CR3BP sphere of influence around Earth, encompassing a large portion of the Sun-Earth $L_2$ Lyapunov family. . . . .	41
2.9	<i>xy</i> -Projection of the Blended CR3BP Model . . . . .	41
3.1	Simple Targeting Example. . . . .	50
3.2	Converged periodic Lyapunov orbit in the Earth-Moon barycentric rotating frame. . . . .	53
3.3	Earth-Moon $L_1$ Lyapunov orbit family. . . . .	54
3.4	Earth-Moon $L_2$ Lyapunov orbit family. . . . .	55
3.5	Earth-Moon Lyapunov family stability index evolution. . . . .	57
3.6	Earth-Moon Lyapunov family time constant evolution. . . . .	58
3.7	Earth-Moon $L_1$ southern halo orbit family. . . . .	61
3.8	Earth-Moon $L_2$ southern halo orbit family. . . . .	62
3.9	Earth-Moon Halo family stability index evolution. . . . .	62
3.10	Earth-Moon butterfly family. . . . .	63
3.11	Earth-Moon butterfly family stability index evolution. . . . .	64
3.12	Earth-Moon $L_1$ northeast axial orbit family. . . . .	65
3.13	Earth-Moon $L_2$ northwest axial orbit family. . . . .	66
3.14	Earth-Moon axial family stability index evolution. . . . .	66
3.15	Earth-Moon $L_1$ vertical orbit family. . . . .	67
3.16	Earth-Moon $L_2$ vertical orbit family. . . . .	68
3.17	Earth-Moon vertical family stability index evolution. . . . .	68
3.18	Earth-Moon $L_4$ and $L_5$ equilateral long period orbit families. . . . .	70

3.19	Earth-Moon equilateral long period orbit family stability index evolution. . . . .	71
3.20	Earth-Moon $L_4$ and $L_5$ equilateral axial families. . . . .	72
3.21	Earth-Moon equilateral axial family stability index evolution. . . . .	73
3.22	Earth-Moon 2:1a resonant orbit family. . . . .	74
3.23	Earth-Moon 2:1a resonant orbit family stability index evolution. . . . .	75
3.24	Earth-Moon 3:4 resonant orbit family. . . . .	76
3.25	Earth-Moon 3:4 resonant orbit family stability index evolution. . . . .	77
3.26	Earth-Moon $L_1$ Lyapunov Manifolds ( $C = 3.05$ ). . . . .	78
3.27	Earth-Moon $L_2$ Halo Manifolds ( $C = 3.08$ ). . . . .	79
3.28	Poincaré map. . . . .	80
4.1	Earth-Moon and Sun-Earth manifolds intersecting at the hyperplane in the Sun-Earth rotating frame. . . . .	83
4.2	The hyperplane phase plots for Figure 4.1. . . . .	84
4.3	Hyperplane phase plots with a near intersection after varying the parameters. . . . .	85
4.4	Initial guess for near-ballistic Earth-Moon to Sun-Earth transfer using phase plots in the Sun-Earth rotating frame. . . . .	86
4.5	Converged near-ballistic tranfer between Earth-Moon and Sun-Earth halo orbits in the Sun-Earth rotating frame. . . . .	87
4.6	Representation of the distant, two-burn MMAT with a plane change (adapted from Canales[33]). . . . .	91
4.7	Representation of the two feasible arrival ellipse orientations. The top images are $XY$ -plane views while the bottom are $XZ$ -plane views. . . . .	92
4.8	MMAT departure CR3BP arc in the Sun-Earth barycentric rotating frame. . . . .	94
4.9	MMAT arrival CR3BP arc in the Sun-Mars barycentric rotating frame. . . . .	95
4.10	Evolution along the MMAT family continued by the initial epoch. . . . .	96
4.11	Minimum- $\Delta v$ MMAT in the Sun-centered Ecliptic J2000 frame. . . . .	97
4.12	Minimum-TOF MMAT in the Sun-centered Ecliptic J2000 frame. . . . .	98
4.13	"Direct" departure CR3BP arc. . . . .	99
4.14	"Direct" MMAT in the Sun-centered Ecliptic J2000 frame. . . . .	100
4.15	Departure unstable manifold arc in the Earth-Moon barycentric rotating frame. . . . .	101
4.16	Departure CR3BP arc with staging orbit in the Sun-Earth barycentric rotating frame. . . . .	102

4.17	MMAT with staging orbit in the Sun-centered Ecliptic J2000 frame.	103
4.18	Tradespace of both solution categories originating from the same Earth-Moon departure orbit.	103
4.19	Hohmann transfer between Earth and Mars.	104
5.1	Transfer tradespace departing from an Earth-Moon $L_1$ northern halo orbit ( $JC = 3.07$ ).	106
5.2	Transfer tradespace departing from an Earth-Moon $L_2$ northern halo orbit ( $JC = 3.13$ ).	107
A.1	Transfer tradespace departing from an Earth-Moon $L_1$ Lyapunov orbit ( $JC = 3.13$ ).	114
A.2	Transfer tradespace departing from an Earth-Moon $L_1$ Lyapunov orbit ( $JC = 3.1$ ).	114
A.3	Transfer tradespace departing from an Earth-Moon $L_1$ Lyapunov orbit ( $JC = 3.07$ ).	115
A.4	Transfer tradespace departing from an Earth-Moon $L_1$ Lyapunov orbit ( $JC = 3.03$ ).	115
A.5	Transfer tradespace departing from an Earth-Moon $L_1$ Lyapunov orbit ( $JC = 3.0$ ).	115
A.6	Transfer tradespace departing from an Earth-Moon $L_1$ Lyapunov orbit ( $JC = 2.98$ ).	116
A.7	Transfer tradespace departing from an Earth-Moon $L_1$ northern halo orbit ( $JC = 3.13$ ).	116
A.8	Transfer tradespace departing from an Earth-Moon $L_1$ northern halo orbit ( $JC = 3.1$ ).	116
A.9	Transfer tradespace departing from an Earth-Moon $L_1$ northern halo orbit ( $JC = 3.07$ ).	117
A.10	Transfer tradespace departing from an Earth-Moon $L_1$ northern halo orbit ( $JC = 3.03$ ).	117
A.11	Transfer tradespace departing from an Earth-Moon $L_2$ northern halo orbit ( $JC = 3.13$ ).	117
A.12	Transfer tradespace departing from an Earth-Moon $L_2$ northern halo orbit ( $JC = 3.1$ ).	118
A.13	Transfer tradespace departing from an Earth-Moon $L_2$ northern halo orbit ( $JC = 3.07$ ).	118
A.14	Transfer tradespace departing from an Earth-Moon $L_2$ northern halo orbit ( $JC = 3.03$ ).	118

## LIST OF SYMBOLS

*Variables*

$a$	Semimajor axis [km]
$B$	Barycenter
$C$	Jacobi constant
$d$	Manifold step-off distance
$d_{SoI}$	Sphere of influence gravitational ratio
$DF$	Jacobian matrix
$E$	Eccentric anomaly [rad (deg)]
$\mathcal{E}$	Specific mechanical energy [km <sup>2</sup> /s <sup>2</sup> ]
$e$	Eccentricity
$\bar{e}$	Eccentricity vector in $\mathbb{R}^3$
$\bar{F}$	Constraint vector
$\bar{F}_g$	Gravitational force vector in $\mathbb{R}^3$ [kN]
$G$	Universal gravitational constant [kN*km <sup>2</sup> /kg <sup>2</sup> ]
$\tilde{G}$	Normalized gravitational constant
$g$	Gravitational acceleration
$\bar{h}$	Specific angular momentum vector in $\mathbb{R}^3$ [km <sup>2</sup> /s]
$i$	Inclination [rad (deg)]
$J$	Cost function cost
$L$	Lagrange (equilibrium) point
$l^*$	Characteristic length [km]
$M$	Mean anomaly [rad (deg)]
$m$	Mass [kg]
$m^*$	Characteristic mass [kg]
$MI$	Momentum integral
$n$	Mean motion [rad/s (deg/s)]
$\tilde{n}$	Normalized mean motion
$\bar{n}$	Node vector in $\mathbb{R}^3$

$P$	Primary
$\mathbb{P}$	Period [s]
$\mathcal{P}_b$	Bridge ratio
$\bar{Q}$	Inertial state vector in $\mathbb{R}^6$
$\bar{q}$	Rotating state vector in $\mathbb{R}^6$
$\bar{R}$	Inertial position vector in $\mathbb{R}^3$ [km]
$r$	Distance [kg]
$\bar{r}$	Position vector in $\mathbb{R}^3$ [km]
$\dot{\bar{r}}$	Velocity vector in $\mathbb{R}^3$ [km/s]
$\ddot{\bar{r}}$	Acceleration vector in $\mathbb{R}^3$ [km/s <sup>2</sup> ]
$r_a$	Radius of apoapsis [km]
$r_p$	Radius of periapsis [km]
$r_{SoI}$	Sphere of influence radius
$s/c$	Spacecraft
$T$	Epoch [s]
$t$	Time [s]
$t^*$	Characteristic time [s]
$TOF$	Time-of-flight [s]
$U$	Pseudo-potential
$v$	Velocity [km/s]
$\bar{v}$	Velocity vector in $\mathbb{R}^3$ [km]
$v_r$	Radial velocity [lm/s]
$X$	Position along the $\hat{X}$ -axis in an inertial frame [km]
$\bar{X}$	Free variable vector
$\ddot{X}$	Acceleration along the $\hat{X}$ -axis in an inertial frame [km/s <sup>2</sup> ]
$x$	Position along the $\hat{x}$ -axis in a rotating frame
$\dot{x}$	Velocity along the $\hat{x}$ -axis in a rotating frame
$\ddot{x}$	Acceleration along the $\hat{x}$ -axis in a rotating frame
$Y$	Position along the $\hat{Y}$ -axis in an inertial frame [km]

$\ddot{Y}$	Acceleration along the $\hat{Y}$ -axis in an inertial frame [km/s <sup>2</sup> ]
$y$	Position along the $\hat{y}$ -axis in a rotating frame
$\dot{y}$	Velocity along the $\hat{y}$ -axis in a rotating frame
$\ddot{y}$	Acceleration along the $\hat{y}$ -axis in a rotating frame
$Z$	Position along the $\hat{Z}$ -axis in an inertial frame [km]
$\ddot{Z}$	Acceleration along the $\hat{Z}$ -axis in an inertial frame [km/s <sup>2</sup> ]
$z$	Position along the $\hat{z}$ -axis in a rotating frame
$\dot{z}$	Velocity along the $\hat{z}$ -axis in a rotating frame
$\ddot{z}$	Acceleration along the $\hat{z}$ -axis in a rotating frame
$\Delta v$	Change in velocity that characterizes a maneuver
$\epsilon$	Machine tolerance
$\theta$	True anomaly [rad (deg)]
$\kappa$	Small perturbation
$\lambda$	Eigenvalue
$\mu$	CR3BP mass ratio
$\mu_{2BP}$	Two-body gravitational constant [kN*km <sup>2</sup> /kg]
$\bar{\nu}$	Eigenvector in $\mathbb{R}^6$
$\bar{P}$	Inertial position vector in $\mathbb{R}^3$
$\dot{\rho}$	Barycentric rotating velocity
$\bar{\rho}$	Barycentric rotating position vector in $\mathbb{R}^3$
$\dot{\bar{\rho}}$	Barycentric rotating velocity vector in $\mathbb{R}^3$
$\Sigma$	Hyperplane
$\varsigma$	Stability index
$\tau$	Time
$\Upsilon$	Time constant
$\Phi$	State transition matrix
$\phi$	State transition matrix element
$\Omega$	Right ascension of ascending node (RAAN) [rad (deg)]
$\omega$	Argument of periapsis [rad (deg)]

$\bar{\omega}$  Angular velocity vector in  $\mathbb{R}^3$

*Coordinate Frames*

$\{\hat{X}, \hat{Y}, \hat{Z}\}$  Arbitrary inertial coordinate frame

$\{\hat{X}_{Ec}, \hat{Y}_{Ec}, \hat{Z}_{Ec}\}$  Ecliptic J2000 inertial coordinate frame

$\{\hat{x}, \hat{y}, \hat{z}\}$  Rotating coordinate frame

## ABBREVIATIONS

2BP	2-Body Problem
BCR4BP	Bicircular Restricted 4-Body Problem
CR3BP	Circular Restricted 3-Body Problem
DRO	Distant retrograde orbit
ER3BP	Elliptic Restricted 3-Body Problem
HFEM	High-fidelity ephemeris model
HR3BP	Hills Restricted 3-Body Problem
HR4BP	Hills Restricted 4-Body Problem
MMAT	Moon-to-moon analytical transfer
NAIF	Navigation and Ancillary Information Facility
NASA	National Aeronautics and Space Administration
NRHO	Near-rectilinear halo orbit
QBCR4BP	Quasi-Bicircular Restricted 4-Body Problem
RAAN	Right ascension of ascending node
SoI	Sphere of influence
STM	State transition matrix
SVD	Singular value decomposition
TOF	Time-of-flight

## **ABSTRACT**

ADD ABSTRACT

# 1. INTRODUCTION

## 1.1 Motivation

In recent years, international interest in cislunar missions and operations has rapidly increased. This is evidenced by the development of infrastructure for the National Aeronautics and Space Administration's (NASA) Gateway program, a long-term hub that will reside in an Earth-Moon Near-Rectilinear Halo Orbit (NRHO) in the lunar vicinity[1]. While there are a lot of exciting opportunities for cislunar missions, periodic orbits and dynamical structures in this region of space can also be exploited as stepping stones on the way to deep-space exploration. In its 2022 Strategic Plan, NASA outlines goals to "Extend human presence to the Moon and on towards Mars for sustainable long-term exploration, development, and utilization" and "Enhance space access and services"[2], that are further supported by its "Moon to Mars Objectives" document released that same year[3]. These documents support the idea that operations and infrastructure in the cislunar region can be employed to support future missions to Mars and other deep-space targets.

Unlike Earth orbits, periodic orbits and trajectories in cislunar space exist in a complex multi-body dynamical regime that is significantly affected by gravitational forces from both the Earth and the Moon (and in some cases the Sun). While the addition of these forces introduces new challenges to the trajectory design process, it also provides opportunities to leverage elements of dynamical systems theory in ways that are not possible with standard Keplerian dynamics. These elements include unstable families of periodic orbits with stable and unstable invariant manifolds that are useful for constructing transfers between orbits. These techniques are currently employed to design missions in the cislunar region and similar strategies can be adapted and applied to construct transfers between cislunar orbits and deep-space targets residing outside of the Earth region.

NASA's goal of establishing a permanent presence on Mars necessitates more efficient and adaptable transfer strategies for missions since traditional approaches have high maneuver costs and are inflexible. In the past, NASA and other space agencies have designed and executed uncrewed interplanetary missions to Mars. However, their goal to develop a human presence on Mars in the near future requires an increase in both crewed and un-

crewed missions to the Martian vicinity, highlighting the need for low-cost, reliable transfer strategies. Traditionally, uncrewed interplanetary missions depart directly from the Earth with high-energy transfers[4]. Not only do these solutions have a high propellant cost, but they are also point solutions that need to be recomputed whenever a mission parameter changes. As humankind prepares for sustained exploration of Mars, the development of more cost-effective and flexible mission strategies is crucial to ensure success.

An alternative option is to depart from a cislunar orbit, perhaps after refueling at a servicing depot, decreasing the propellant costs for both the launch from the surface of Earth and the interplanetary transfer. The past successful applications of multi-body dynamical systems theory to cislunar transfer design suggest that these techniques can also be applied to deep-space transfers with similar performance. Utilizing unstable periodic orbit families and invariant manifold theory allows for lower-energy and lower-cost departures from the Earth-Moon system. After departure, patched dynamical models and existing transfer techniques are employed to complete the construction of end-to-end transfers from the Earth-Moon system to deep-space destinations. One consequence of this approach is that invariant manifolds often increase the trajectory time-of-flight. While long times-of-flight are not desirable characteristics for manned missions due to radiation and other concerns, it is an acceptable trade-off for cargo and supply missions. Consequently, rather than focusing on optimizing the interplanetary transfer itself, comparing available unstable periodic orbit families leads to insight into time-efficient departures from the Earth-Moon system. The exploitation of simplified dynamical models also provides families of transfers instead of point solutions, adding flexibility to the mission design process. Incorporating these dynamical techniques into mission planning offers a more flexible approach to deep-space transfers.

## 1.2 Research Objectives

To sustain an increase in missions to Mars and other deep-space targets, a framework for lower-cost transfers from the Earth region is necessary. One promising avenue to decrease propellant costs is to utilize invariant manifold theory for low-energy departures from unstable multi-body periodic orbits in the cislunar region. Since the application of multi-

body dynamical systems theory to cislunar mission design is relatively new, little is known about the departure characteristics for families of unstable periodic orbits modeled in the Earth-Moon Circular Restricted 3-Body Problem (CR3BP). Additionally, previous work has determined that invariant manifolds from one Sun-planet CR3BP system do not connect to manifolds in other systems in a practical amount of time[5]. Consequently, new transfer design methodologies must be developed to connect manifolds from planetary systems. Finally, since the current standard methods for interplanetary transfers produce only point solutions, it would be beneficial to have new flexible methodologies that provide families of transfers. Developing these new methodologies that connect invariant manifolds across Sun-planet systems is key to achieving lower-energy deep-space transfers.

Consequently, this investigation aims to develop a design methodology for end-to-end transfers to deep-space targets that provides families of solutions to compare the departure characteristics of unstable Earth-Moon CR3BP periodic orbit families. This goal is broken down into the following objectives:

1. **Establish a low-energy transfer design methodology between the cislunar region and Mars that utilizes CR3BP invariant manifolds.** This new transfer methodology includes a solution for bridging the gap between the invariant manifolds of Sun-planet CR3BP systems. Employing the CR3BP and patched models, the resulting solutions also exist in families, providing flexible mission design.
2. **Compare transfers that stage in intermediate Sun-Earth halo orbits to "direct" transfers.** Immediately once a trajectory departs the Earth-Moon CR3BP, it is in a region of space that is modeled by the Sun-Earth CR3BP. Sun-Earth invariant manifolds may depart their system faster than Earth-Moon manifolds that are propagated in the Sun-Earth model. Consequently, transfers that arrive at an intermediate Sun-Earth staging orbit are compared to those that take a more direct trajectory to determine the classification that has more favorable departure characteristics.
3. **Analyze and compare the Earth-Moon departure characteristics of various unstable CR3BP periodic orbit families within the framework of this investigation.** The ultimate goal of this investigation is to compare families of unstable

Earth-Moon orbits to determine the ones that provide low-energy transfers to Mars with lower times-of-flight. The results inform future interplanetary and deep-space mission designs and lend insight into cislunar departure dynamics.

To demonstrate the transfer methodologies, all the end-to-end cislunar-to-Mars transfers in this investigation depart from various Earth-Moon CR3BP orbits but arrive at the same Sun-Mars  $L_1$  northern halo orbit. Although this investigation primarily investigates cislunar-to-Mars transfers, the techniques and developed methodologies apply to many other applications involving CR3BP systems and other deep-space targets.

### 1.3 Previous Contributions

Traditionally, missions to Mars and other deep-space targets employ direct, impulsive transfers that depart from the Earth or low Earth orbit. Porkchop plots are often applied in tandem with patched conics to quickly provide point initial guesses for various epochs[4]. Earth flybys have also been proposed by Landau and Longuski to reduce propellant requirements[6], while Fritz and Turkoglu harness gravity-assist maneuvers around other bodies[7]. While they are practical strategies for fast transfers, these traditional methods highlight the need for innovative techniques to reduce propellant costs and increase mission flexibility.

The application of multi-body dynamics to space trajectory design has evolved significantly since its origins, leading to its application in several notable missions. One of the biggest breakthroughs in multi-body astrodynamics occurred with the development of the CR3BP by Euler in 1722[8]. However, it took centuries before this model was finally incorporated into trajectory design in the late 20th century. Some notable missions that have utilized multi-body dynamics include the International Sun-Earth Explorer-3 (ISEE-3)[9], Genesis[10], ARTEMIS[11], and CAPSTONE[12]. Currently, this model and associated techniques are also being employed to design the baseline trajectory and operations for NASA's Gateway hub[1], [13], [14]. Dynamical systems theory continues to play an increasing role in spacecraft mission design, offering new possibilities for future exploration.

Within the context of interplanetary transfers and missions to deep-space targets, although missions applying multi-body dynamical systems theory have yet to be flown, sev-

eral authors have developed/proposed multi-body dynamics methodologies. Miele and Wang exploit the dynamics of a circular-restricted 4-body problem to numerically optimize transfers between Keplerian LEO and low Mars orbits[15]. Going a step further, Conte starts from a lunar distant retrograde orbit (DRO), a stable CR3BP orbit, but still employs pork-chop plots to design direct transfers to low Mars orbits[16], while Esper and Aldrin harness aero-braking to arrive into a Phobos DRO[17]. Interplanetary transfer design strategies utilizing multi-body invariant manifolds started to appear around 2005 with Topputo et al., who investigated transfers between CR3BP Sun-Earth and Sun-Mars Lyapunov orbits[18]. Nakamiya et al. conducted a similar investigation between Sun-Earth and Sun-Mars halo orbits in the Hills restricted 3-body problem (HR3BP)[19]. Haibin et al. added gravity assists and pseudo-manifolds to aid in the transfer process between Sun-Earth and Sun-Mars halo orbits in the CR3BP[20], while Kakoi et al. investigated transfers from Earth-Moon CR3BP halo orbits to Mars[21]. To depart from a stable CR3BP orbit, Cavallari et al. utilize Earth-Moon Lyapunov manifolds to facilitate transfers between lunar DROs and Sun-Mars Lyapunov orbits[22]. Most recently in 2022, Scantamburlo et al. investigated Lyapunov manifolds in the Elliptic Restricted 3-Body Problem (ER3BP) to connect the Sun-Earth and Sun-Mars systems[23], and Canales et al. employed a semi-analytical moon-to-moon transfer design methodology to construct trajectories between CR3BP Sun-Earth and Sun-Mars halo orbits[24], [25]. Taking a slightly different approach, Lu et al.[26], Shimane and Ho[27], and Singh and Negi[28] investigated the application of low-thrust maneuvers (instead of impulsive) to connect the invariant manifolds of Sun-planet systems. Almost all of these previous studies treat the Sun-Earth and Sun-Mars systems as coplanar, and none of them include analyses of other periodic orbit families besides Lyapunovs and halos.

Several authors have also investigated connecting Earth-Moon to Sun-Earth orbits in their respective CR3BP systems. Masdemont et al. go directly to CR3BP Sun-Earth libration point orbits from Keplerian lunar orbits[29]. The previous study by Kakoi et al. utilizes a patched CR3BP model to ballistically connect Earth-Moon and Sun-Earth halo orbits in their actual respective planes[21]. Guo and Lei conducted a similar investigation to CR3BP Sun-Earth libration point orbits[30], whereas Pasquale et al. investigated heliocentric escape options[31]. Finally, other authors have also investigated connections in other

dynamical models, such as Boudad et al. with the Bi-Circular Restricted 4-Body Problem (BCR4BP)[32]. These studies demonstrate the growing interest in leveraging multi-body dynamical systems theory to connect various space regimes, offering valuable insights for future mission designs.

## 1.4 Overview of Current Work

The main goal of this investigation is to compare families of unstable periodic orbits in the Earth-Moon CR3BP to determine the ones that have desirable system departure characteristics. A transfer design methodology is developed between the Earth-Moon and Sun-Mars CR3BP systems that utilizes invariant manifolds to facilitate the orbit family comparison. This methodology consists of two transfer types: one that stages at an intermediate Sun-Earth halo orbit and one that is direct. Both types produce families of transfers instead of just point solutions, allowing for more flexible mission designs. The resulting methodology and results apply to other deep-space targets besides Mars, such as Venus or asteroids, and provide insight into general low-energy interplanetary transfers.

The following chapters elaborate on the cislunar-to-Mars transfer design methodology and the CR3BP Earth-Moon unstable orbit family analysis:

- **Chapter 2: Dynamical Models**

This chapter introduces the dynamical models and coordinate frames that are employed in this investigation. The 2-Body Problem (2BP) and CR3BP are the main dynamical models utilized, with patched and blended model combinations that describe transitions between the systems. Within the CR3BP, the barycentric synodic rotating frame is primarily employed to represent trajectories, but a Sun-centered Ecliptic J2000 frame best represents the interplanetary transfers in their entirety.

- **Chapter 3: CR3BP Dynamical Structures**

The techniques from dynamical systems theory that are applied in this investigation are described here. These numerical techniques and dynamical structures are utilized in both the transfer design process and the subsequent analysis of the system departure characteristics. This chapter also includes examples of the unstable CR3BP periodic

orbit families that appear throughout this investigation, as well as procedures for generating invariant manifolds from them.

- **Chapter 4: Cislunar-to-Mars Trajectory Construction**

Two existing transfer methodologies are adapted and combined to form the end-to-end cislunar-to-Mars transfer strategy. All of the transfers utilize a version of the moon-to-moon analytical transfer (MMAT) method developed by Canales[33]. If transfers stage at an intermediate Sun-Earth orbit, near-ballistic transfers between the Earth-Moon orbits and the Sun-Earth halo orbits are constructed similarly to Kakoi’s methodology[34]. This chapter also explains Hohmann transfers and their utility in designing direct transfers between the Earth and Mars.

- **Chapter 5: Cislunar Departure Orbit Comparison**

With a fully developed end-to-end transfer strategy, cislunar-to-Mars trajectories are constructed, originating from a variety of unstable Earth-Moon orbits. Several periodic orbit families, and orbits at different Jacobi constants (energy levels) within these families, are analyzed to determine those that provide favorable system departure characteristics compared to the others. This chapter also includes a comparison between the direct transfers and those that utilize intermediate staging orbits. It concludes with a comparison of the transfer results to those from the existing literature, including Hohmann transfers.

- **Chapter 6: Conclusion**

The main results and conclusions of the investigation are summarized along with recommendations for potential future work.

## 2. DYNAMICAL MODELS

This analysis relies on the utilization of two primary dynamical models: The 2-body problem (2BP) and the circular restricted 3-body problem (CR3BP). The 2BP serves as a model for spacecraft dynamics when their motion is solely governed by the gravitational influence of a single body, primarily applied to the study of heliocentric arcs within this investigation. In cases where the dynamics are significantly influenced by the gravitational forces of two bodies, as exemplified in Sun-planet or the Earth-Moon systems, the CR3BP offers a more accurate description of the spacecraft's motion.

### 2.1 Coordinate Frames

In this investigation, Cartesian coordinate frames are employed to represent three-dimensional vector quantities. These frames may remain fixed in space (inertial) or rotate about the origin at a constant angular rate (rotating). The choice of coordinate frame depends on the specific application as it can be advantageous to position the origin at the center of mass of the system (barycenter) or align it with a primary body of interest.

#### 2.1.1 Barycentric Rotating and Inertial Frames

In a CR3BP system, the motion of a spacecraft is best depicted within a rotating frame with its origin at the system barycenter. The  $\hat{x}$ -axis is defined to extend from the barycenter toward the smaller primary body, while the  $\hat{z}$ -axis aligns with the system's angular momentum vector. Completing the triad, the  $\hat{y}$ -axis is  $\hat{y} = \hat{z} \times \hat{x}$ . This frame rotates about the barycenter at a constant angular rate identical to that of the primary bodies.

Additionally, an arbitrary barycentric inertial frame can be similarly defined using the rotating axes at a specific instance in time, denoted as  $\hat{X}$ ,  $\hat{Y}$ , and  $\hat{Z}$ . As time progresses, the inertial frame remains fixed in space, whereas the rotating frame revolves around the shared origin with the primaries. In Figure 2.1, the barycentric  $\{\hat{x}, \hat{y}, \hat{z}\}$  rotating frame and  $\{\hat{X}, \hat{Y}, \hat{Z}\}$  inertial frames for an example CR3BP system are illustrated, with their common origin centered at the barycenter of the primaries,  $P_1$  and  $P_2$ . The angle between the two

frames is denoted here by  $\theta$  and it increases at a constant rate of  $n$ . It is important to note that both the  $\hat{Z}$ - and  $\hat{z}$ -axes adhere to the right-hand frame convention, pointing out of the page.

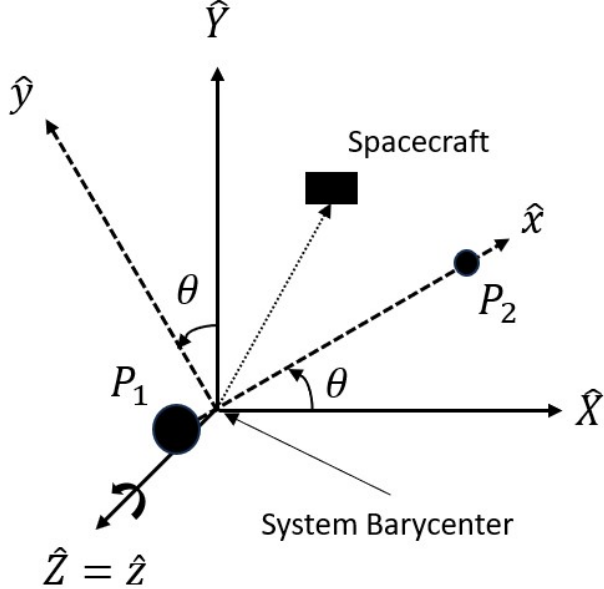


**Figure 2.1.** Barycentric rotating and inertial frames in a CR3BP system.

### 2.1.2 The Ecliptic J2000 Primary-Centered Inertial Frame

A commonly used primary-centered inertial frame is the Ecliptic J2000. As the name implies, this frame is established with its origin at the center of a primary body and the Sun-Earth orbital plane on January 1, 2000 as the  $\hat{X}_{Ec}\hat{Y}_{Ec}$ -plane. The  $\hat{X}_{Ec}$ -axis is directed towards the vernal equinox, which is the line of intersection between the Earth's equatorial and ecliptic planes on January 1, 2000. The  $\hat{Z}_{Ec}$ -axis is orthogonal to the ecliptic plane, and the  $\hat{Y}_{Ec}$ -axis completes the triad, defined as  $\hat{Y}_{Ec} = \hat{Z}_{Ec} \times \hat{X}_{Ec}$ .

Since the frame is centered on a primary, it applies to both the 2BP and CR3BP, making it also valuable for patched dynamical models. The construction of this coordinate frame, as depicted in Figure 2.2, is computed using the Navigation and Ancillary Information Facility's (NAIF) SPICE ephemeris toolkit[35].

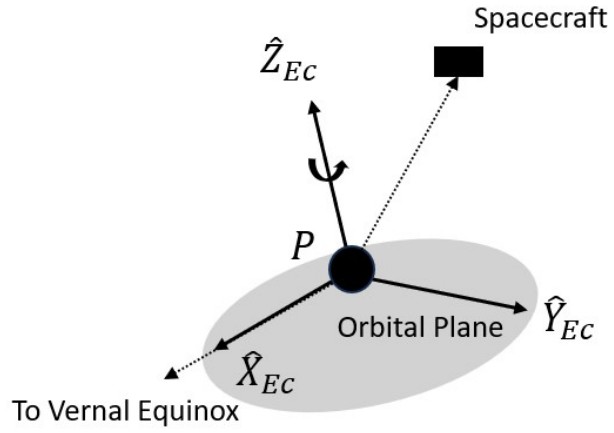


**Figure 2.2.** Earth-centered Ecliptic J2000 inertial frame.

## 2.2 The Two-Body Problem

This investigation treats the motion of spacecraft in heliocentric space, specifically when they are far from planets and moons, as a 2-body Problem, governed by a single gravitational force. This section provides a brief overview of key aspects of 2BP dynamics, Keplerian orbital elements, and Kepler's Equation. For a more comprehensive derivation of the 2BP, refer to Chapters 1 and 2 of Vallado's *Fundamentals of Astrodynamics and Applications*[36]. Additionally, Canales highlights the background information relevant to understanding the transfer methodologies presented in this analysis[33].

### 2.2.1 Equations of Motion

The 2BP involves two point masses—a primary body and a spacecraft—that exert gravitational forces on each other. Since no external forces act on this system, the center of mass of the bodies moves at a constant velocity and serves as the origin for an inertial coordinate frame. In this inertial frame, the gravitational force that the primary body exerts on the spacecraft, denoted as  $\bar{F}_{g_{P \rightarrow s/c}}$ , is expressed as:

$$\bar{F}_{g_{P \rightarrow s/c}} = -\frac{Gm_P m_{s/c}}{r_{P \rightarrow s/c}^3} \bar{r}_{P \rightarrow s/c}, \quad (2.1)$$

where  $G$  is the universal gravitational constant ( $6.67384 \times 10^{-20}$  kN\*km $^2$ /kg $^2$ ),  $m_P$  and  $m_S$  are the masses of the primary body and spacecraft, respectively,  $r_{P \rightarrow s/c}$  is the distance from the primary body to the spacecraft, and  $\bar{r}_{P \rightarrow s/c} = \bar{r}_{s/c} - \bar{r}_P$  is the position vector from the primary body to the spacecraft in the inertial frame, as illustrated in Figure 2.3.

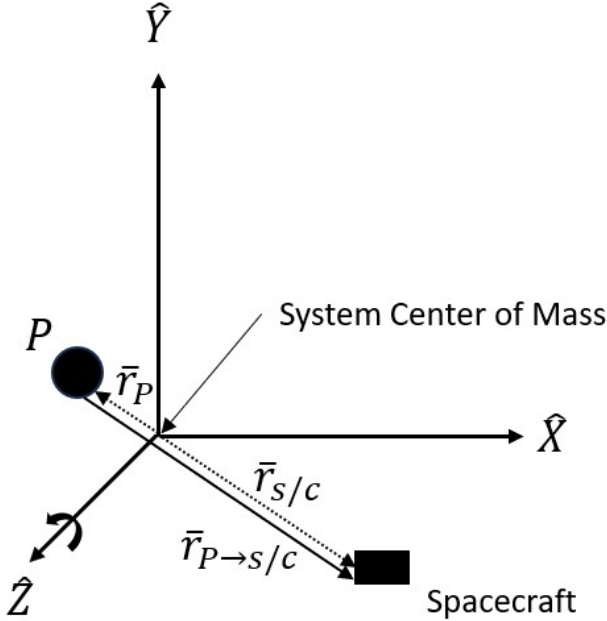


**Figure 2.3.** Two-body problem in a barycentric inertial frame.

Assuming that the mass of the spacecraft is negligible compared to the mass of the primary body, the nonlinear relative equation of motion for the 2BP is derived[33], [36]:

$$\ddot{\bar{r}}_{P \rightarrow s/c} = -\frac{\mu_{2BP}}{r_{P \rightarrow s/c}^3} \bar{r}_{P \rightarrow s/c}, \quad (2.2)$$

where  $\ddot{\bar{r}}_{P \rightarrow s/c}$  is the inertial acceleration of the spacecraft relative to the primary body and  $\mu_{2BP} = Gm_P$ . This vector equation can also be expressed as  $\hat{X}$ ,  $\hat{Y}$ , and  $\hat{Z}$  scalar equations in the inertial frame:

$$\ddot{X} = -\frac{\mu_{2BP}}{r_{P \rightarrow s/c}^3} (X_{s/c} - X_P), \quad (2.3)$$

$$\ddot{Y} = -\frac{\mu_{2BP}}{r_{P \rightarrow s/c}^3} (Y_{s/c} - Y_P), \quad (2.4)$$

$$\ddot{Z} = -\frac{\mu_{2BP}}{r_{P \rightarrow s/c}^3} (Z_{s/c} - Z_P). \quad (2.5)$$

### 2.2.2 Conic Sections

Instead of relying on numerical propagation of the nonlinear equations of motion, space-craft motion in the 2BP can be effectively represented analytically using conic sections. This section provides a concise overview of conic motion in the 2BP.

Two essential constants characterize conic orbits: specific angular momentum  $\bar{h}$  and specific mechanical energy  $\mathcal{E}$ :

$$\bar{h} = \bar{r}_{P \rightarrow s/c} \times \dot{\bar{r}}_{P \rightarrow s/c}, \quad (2.6)$$

$$\mathcal{E} = \frac{v_{P \rightarrow s/c}^2}{2} - \frac{\mu_{2BP}}{r_{P \rightarrow s/c}}, \quad (2.7)$$

where  $v_{P \rightarrow s/c} = \|\dot{\bar{r}}_{P \rightarrow s/c}\|_2$  is the spacecraft velocity in the inertial frame relative to the primary body.

Kepler's first law, asserting that orbital motion is conic, provides the trajectory equation for the 2BP:

$$r_{P \rightarrow s/c} = \frac{a(1 - e^2)}{1 + e \cos(\theta)}, \quad (2.8)$$

where  $a$  represents the orbit semimajor axis,  $e$  is the orbit eccentricity, and  $\theta$  denotes the orbit true anomaly. These three elements will be elaborated upon in a later subsection. Equation (2.8) can also be employed to compute the periapsis and apoapsis distances,  $r_p$  and  $r_a$  respectively:

$$r_p = a(1 - e), \quad (2.9)$$

$$r_a = a(1 + e). \quad (2.10)$$

The eccentricity can also be used to determine the type of conic section:

- $e = 0$ : Circular orbit (a special case of an ellipse).
- $0 < e < 1$ : Elliptical orbit.
- $e = 1$ : Parabola.

- $e > 1$ : Hyperbola.

This investigation focuses on circles and ellipses with  $0 \leq e < 1$ .

Similarly, Kepler's third law provides the orbit period  $\mathbb{P}$  and, consequently, the mean motion  $n$ :

$$\mathbb{P} = 2\pi\sqrt{\frac{a^3}{\mu_{2BP}}}, \quad (2.11)$$

$$n = \frac{2\pi}{\mathbb{P}} = \sqrt{\frac{\mu_{2BP}}{a^3}}. \quad (2.12)$$

### 2.2.3 Keplerian Orbital Elements

Instead of specifying the six-dimensional state of a spacecraft in a 2BP elliptical orbit using Cartesian coordinates, six orbital elements can be employed to articulate the size, shape, orientation, and current location along the orbit. In addition to the semimajor axis  $a$  and eccentricity  $e$ , which were introduced earlier and describe the size and shape of the ellipse, three angles characterize the orientation of the orbit with respect to an inertial frame, as depicted in Figure 2.4:

- **Inclination**  $i$  signifies the tilt of the orbital plane relative to the inertial  $\hat{X}_{Ec}\hat{Y}_{Ec}$ -plane.
- **Right ascension of the ascending node** (RAAN)  $\Omega$  denotes the angle between the  $\hat{X}_{Ec}$ -axis and the ascending node, where the orbit crosses the  $\hat{X}_{Ec}\hat{Y}_{Ec}$ -plane in the positive  $\hat{Z}_{Ec}$  direction.
- **Argument of periapsis**  $\omega$  is the angle between the ascending node and the periapsis.

Finally, the true anomaly  $\theta$  defines the spacecraft's position relative to the orbit's periapsis.

#### Cartesian state to Keplerian orbital elements

To convert from a Cartesian state vector to Keplerian orbital elements, start by calculating the inclination from angular momentum:

$$i = \arccos\left(\frac{h_Z}{\|h\|}\right) \quad (2.13)$$

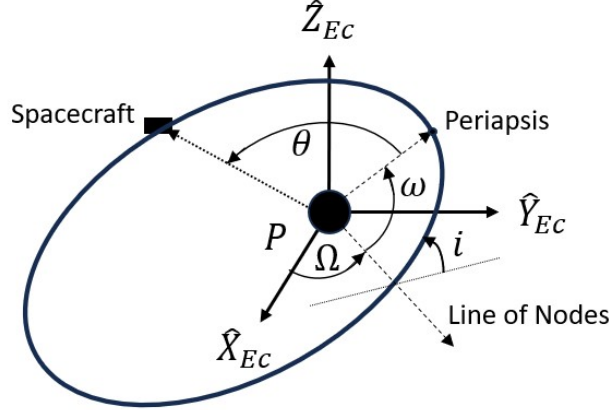


**Figure 2.4.** Orientation and location along an orbit in an inertial frame using Keplerian orbital elements.

Using the node vector  $\bar{n}$ :

$$\bar{n} = \hat{Z}_{Ec} \times \bar{h}, \quad (2.14)$$

the RAAN becomes:

$$\Omega = \begin{cases} \arccos\left(\frac{n_X}{\|\bar{n}\|}\right) & n_Y \geq 0 \\ 2\pi - \arccos\left(\frac{n_X}{\|\bar{n}\|}\right) & n_Y < 0 \end{cases}. \quad (2.15)$$

The eccentricity vector  $\bar{e}$  is also calculated from the angular momentum:

$$\bar{e} = \frac{\dot{\bar{r}}_{P \rightarrow s/c} \times \bar{h}}{\mu_{2BP}} - \frac{\bar{r}_{P \rightarrow s/c}}{r_{P \rightarrow s/c}}, \quad (2.16)$$

and

$$e = \|\bar{e}\|. \quad (2.17)$$

The remaining three orbital elements are calculated as follows:

$$a = \frac{\|\bar{h}\|}{\mu_{2BP}(1 - e^2)}, \quad (2.18)$$

$$\omega = \begin{cases} \arccos\left(\frac{\bar{n} \cdot \bar{e}}{\|\bar{n}\|e}\right) & e_Z \geq 0 \\ 2\pi - \arccos\left(\frac{\bar{n} \cdot \bar{e}}{\|\bar{n}\|e}\right) & e_Z < 0 \end{cases}, \quad (2.19)$$

$$\theta = \begin{cases} \arccos\left(\frac{\bar{e} \cdot \dot{r}_{P \rightarrow s/c}}{e r_{P \rightarrow s/c}}\right) & v_r \geq 0 \\ 2\pi - \arccos\left(\frac{\bar{e} \cdot \dot{r}_{P \rightarrow s/c}}{e r_{P \rightarrow s/c}}\right) & v_r < 0 \end{cases}, \quad (2.20)$$

where

$$v_r = \frac{\dot{r}_{P \rightarrow s/c} \cdot \bar{r}_{P \rightarrow s/c}}{r_{P \rightarrow s/c}}. \quad (2.21)$$

### Keplerian orbital elements to Cartesian state

Similarly, the Cartesian state vector can be obtained from the Keplerian orbital elements. First, the eccentric anomaly  $E$  is needed, which is the angle made by the eccentricity vector pointing to periapsis and the vector from the center of the ellipse to the point directly above the spacecraft location (perpendicular to the eccentricity vector) on an auxiliary circle drawn tangent to the ellipse. The eccentric anomaly and the auxiliary circle are illustrated in Figure 2.5, along with the eccentricity vector and semimajor axis.

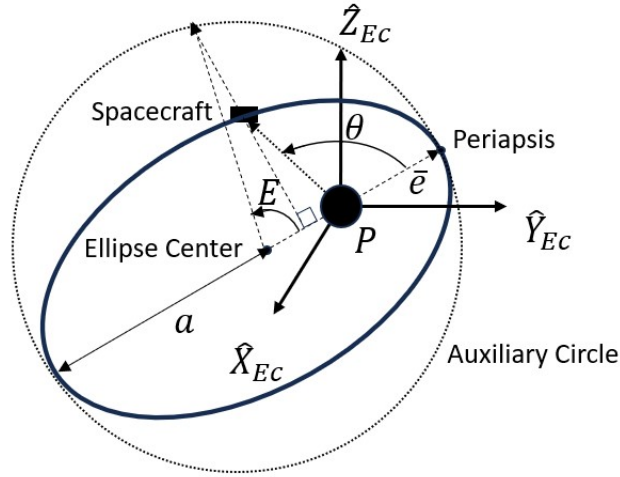


**Figure 2.5.** Definition of eccentric anomaly and the auxiliary circle.

The eccentric anomaly can be related to the true anomaly,

$$E = \arctan\left(\frac{\sqrt{1 - e^2} \sin(\theta)}{e + \cos(\theta)}\right), \quad (2.22)$$

which can then be used to calculate the distance from the primary:

$$r_{P \rightarrow s/c} = a(1 - e \cos(E)). \quad (2.23)$$

This can be used to generate position and velocity magnitude vectors:

$$\bar{r}_0 = \begin{bmatrix} r_{P \rightarrow s/c} \cos(\theta) \\ r_{P \rightarrow s/c} \sin(\theta) \\ 0 \end{bmatrix}, \quad (2.24)$$

$$\dot{\bar{r}}_0 = \sqrt{\frac{\mu_{2BPA}}{r_{P \rightarrow s/c}}} \begin{bmatrix} -\sin(E) \\ \sqrt{1-e^2} \cos(E) \\ 0 \end{bmatrix}. \quad (2.25)$$

These vectors will need to be rotated relative to the inertial frame axes according to the inclination, RAAN, and argument of periapsis:

$$C = \begin{bmatrix} \cos(\Omega) \cos(\omega) - \cos(i) \sin(\Omega) \sin(\omega) & -\cos(\Omega) \sin(\omega) - \cos(i) \sin(\Omega) \cos(\omega) & 0 \\ \sin(\Omega) \cos(\omega) + \cos(i) \cos(\Omega) \sin(\omega) & -\sin(\Omega) \sin(\omega) + \cos(i) \cos(\Omega) \cos(\omega) & 0 \\ \sin(i) \sin(\omega) & \sin(i) \cos(\omega) & 0 \end{bmatrix}, \quad (2.26)$$

$$\bar{r}_{P \rightarrow s/c} = C \bar{r}_0, \quad (2.27)$$

$$\dot{\bar{r}}_{P \rightarrow s/c} = C \dot{\bar{r}}_0. \quad (2.28)$$

#### 2.2.4 Kepler's Equation

If the difference in true anomaly between two points on an orbit is known, Kepler's equation becomes a valuable tool for calculating the time-of-flight between these points. The mean anomaly  $M$  serves as a measure of how much of the orbit has been traversed past periapsis with respect to time:

$$M = \frac{2\pi(t - t_p)}{P}, \quad (2.29)$$

where  $(t - t_p)$  represents the time since periaxis.

Kepler's equation establishes a connection between the mean and eccentric anomalies, thereby linking the eccentric anomaly to time:

$$M = E - e \sin(E). \quad (2.30)$$

To determine eccentric anomalies given corresponding true anomalies, employ Equation (2.22), and subsequently, using Kepler's equation (Equation (2.30)), convert them to mean anomalies. The difference in mean anomalies with Equation (2.29) provides the time-of-flight between the two points along the orbit.

## 2.3 The Circular Restricted Three-Body Problem

When a spacecraft is significantly impacted by the gravitational force of two celestial bodies the circular restricted 3-body problem better approximates the spacecraft's motion compared to two-body problems. Therefore, this investigation uses the CR3BP to model the Earth-Moon and Sun-planet systems when appropriate. The CR3BP is an autonomous model (its dynamics are time-invariant) that provides insight into the dynamical structures present in the system without some of the complexities of a higher-fidelity ephemeris model.

### 2.3.1 Equations of Motion

The CR3BP consists of three primary bodies, two celestial bodies and a massless spacecraft. The two celestial bodies exert gravitational forces on each other and the satellite; however, the satellite does not affect the other two bodies.

The two celestial bodies are treated as point masses and assumed to move in circular orbits, with a constant angular velocity, around their barycenter  $B$ . Assuming that no other forces are acting on the system,  $B$  can be considered an inertial point, and similar to the 2BP, Newton's Laws can be expressed relative to that point. Unlike the 2BP, there is currently no analytical solution to represent the dynamics of the CR3BP. Consequently, all trajectories

in this model must be numerically propagated in time using nonlinear, coupled equations of motion.

It is also useful and common practice to represent these equations and visualize them in a barycentric rotating coordinate frame,  $\{\hat{x}, \hat{y}, \hat{z}\}$ , as shown by the dashed lines in Figure 2.1 and described in Section 2.1. In this frame, the two celestial primaries remain fixed, while the spacecraft moves relative to them in three-dimensional configuration space.

A single mass ratio  $\mu$  characterizes a CR3BP system:

$$\mu = \frac{m_2}{m_1 + m_2}, \quad (2.31)$$

where  $m_1$  and  $m_2$  are the masses of the larger and smaller celestial primaries, respectively. In the barycentric rotating frame,  $P_1$  is located at  $x = -\mu$  and  $P_2$  is located at  $x = 1 - \mu$ . Using this parameter, a pseudo-potential function  $U$  describes the gravitational forces on the system expressed in the barycentric rotating frame:

$$U = \frac{1}{2}(x^2 + y^2) + \frac{1 - \mu}{d} + \frac{\mu}{r}, \quad (2.32)$$

$$d = \sqrt{(x + \mu)^2 + y^2 + z^2}, \quad (2.33)$$

$$r = \sqrt{(x - 1 + \mu)^2 + y^2 + z^2}, \quad (2.34)$$

where here,  $d$  and  $r$  are the distances from  $P_1$  and  $P_2$ , respectively. From the pseudo-potential, the scalar nonlinear equations of motion are expressed in the barycentric rotating frame:

$$\ddot{x} = 2\dot{y} + \frac{\partial U}{\partial x} = 2\dot{y} + x - \frac{(1 - \mu)(x + \mu)}{d^3} - \frac{\mu(x - 1 + \mu)}{r^3}, \quad (2.35)$$

$$\ddot{y} = -2\dot{x} + \frac{\partial U}{\partial y} = -2\dot{x} + y - \frac{(1 - \mu)y}{d^3} - \frac{\mu y}{r^3}, \quad (2.36)$$

$$\ddot{z} = \frac{\partial U}{\partial z} = -\frac{(1 - \mu)z}{d^3} - \frac{\mu z}{r^3}. \quad (2.37)$$

Many authors provide detailed derivations for these equations of motion; one useful reference is Zimovan's Ph.D. dissertation[37].

### 2.3.2 Nondimensionalized Values

Since planetary systems deal with massive distance and velocity scales, it is often helpful in computations to use normalized length, time, and mass values with nondimensional units. Each CR3BP system has characteristic values that are used in this normalization process:

- **Characteristic length**  $l^*$  is the distance between the celestial primaries.
- **Characteristic time**  $t^*$  is selected so that the mean motion of these primaries is unity ( $\tilde{n} = 1$ ). This results in the primaries having circular orbital periods of  $2\pi$  nondimensional units.
- **Characteristic mass**  $m^*$  is the sum of the masses of these two bodies.

These definitions result in the following equations:

$$l^* = r_{12}, \quad (2.38)$$

$$m^* = m_1 + m_2, \quad (2.39)$$

$$t^* = \sqrt{\frac{l^{*3}}{Gm^*}}, \quad (2.40)$$

$$\tilde{G} = G \frac{l^{*3}}{m^* t^{*2}} = 1, \quad (2.41)$$

which are used to normalize all dimensional values in the problem. Table 2.1 shows the mass ratios and characteristic values for the three CR3BP systems used in this investigation.

**Table 2.1.** Characteristic values of relevant CR3BP systems.

CR3BP System	$\mu$	$l^* [\text{km}]$	$t^* [\text{s}]$	$m^* [\text{kg}]$
Earth-Moon	$1.21506 \times 10^{-2}$	$3.84748 \times 10^5$	$3.75700 \times 10^5$	$6.04604 \times 10^{24}$
Sun-Earth	$3.00348 \times 10^{-6}$	$1.49598 \times 10^8$	$5.02264 \times 10^6$	$1.98855 \times 10^{30}$
Sun-Mars	$3.22715 \times 10^{-7}$	$2.27941 \times 10^8$	$9.44664 \times 10^6$	$1.98855 \times 10^{30}$

### 2.3.3 Equilibrium Points

In the barycentric rotating frame, there are five equilibrium points (also called libration or Lagrange points) where there is no net acceleration (i.e., the pseudo-potential acceleration is balanced by the centrifugal acceleration). Thus, a spacecraft at these positions with no initial velocity would remain stationary in this model. All five Lagrange points lie in the  $xy$ -plane. Three Lagrange points lie along the axis of the two celestial primaries and are called the collinear equilibrium points:  $L_1$  is between the two bodies,  $L_2$  is past the smaller body, and  $L_3$  is past the larger body. A Newton-Raphson algorithm can be used to find the location of these points for a given mass ratio.  $L_4$  and  $L_5$  are equilateral equilibrium points because they form equilateral triangles with the primary bodies. Their locations can be determined through geometric relationships. The energy level (or corresponding Jacobi constant, introduced in the next section) increases through points 1-4 ( $L_4$  and  $L_5$  are at the same energy level). Figure 2.6 shows the layout of the Lagrange points in a generic CR3BP barycentric rotating frame.

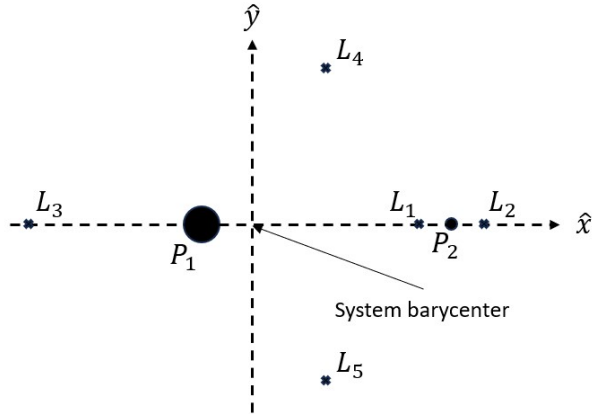


**Figure 2.6.** CR3BP barycentric rotating frame with Lagrange points.

### 2.3.4 Jacobi Constant

One reason that the CR3BP does not have a closed-form analytical solution like the 2BP is there are not enough integrals of the motion, at least that have been discovered to

date. However, there is one such constant of the motion in the rotating frame, denoted as the Jacobi constant, and it proves useful as an analogy to energy. The derivation is as follows[37]:

$$\nabla U \cdot \dot{\vec{r}} = \frac{\partial U}{\partial x} \dot{x} + \frac{\partial U}{\partial y} \dot{y} + \frac{\partial U}{\partial z} \dot{z} = (\ddot{x} - 2\dot{y})\dot{x} + (\ddot{y} + 2\dot{x})\dot{y} + \ddot{z}\dot{z}, \quad (2.42)$$

where  $\dot{\vec{r}}$  is the rotating velocity vector. The middle of Equation (2.42) is equivalent to the total nondimensional time derivative of the pseudo-potential:

$$\frac{dU}{d\tau} = \ddot{x}\dot{x} + \ddot{y}\dot{y} + \ddot{z}\dot{z}, \quad (2.43)$$

where  $\tau$  is nondimensional time. Integrating and rearranging this equation provides the Jacobi constant as a function of rotating position and velocity:

$$C = 2U - \dot{\rho}^2, \quad (2.44)$$

where  $C$  is the Jacobi constant.

This definition of the Jacobi constant is consistent with the Hamiltonian of the system, which is time-invariant in the CR3BP[13]. Note also that as the Jacobi constant increases, the energy of the trajectory decreases.

## 2.4 Patched Dynamical Models

A variety of methods exist to model the gravitational forces of three (or more) celestial bodies in dynamical systems. While a high-fidelity ephemeris model (HFEM) provides the best accuracy, some models utilize simplifying assumptions to reduce computations and gain more insight into the dynamics of the system while maintaining adequate fidelity. For including all of the bodies in one model, there exist several 4-body problems that differ in layout, coherency, and fidelity. Some of the more prominent options are the (BCR4BP)[38], Hills restricted 4-body problem (HR4BP)[39], and quasi-bicircular restricted 4-body problem (QBCR4BP)[40]. A different approach, and the one used in this investigation, is to patch

together 2BP and CR3BP models to build a larger model to represent the dynamics. Two such patched models are outlined here.

### 2.4.1 The Patched 2BP-CR3BP Model

A patched 2BP-CR3BP model is used to describe trajectories as they move between CR3BP systems via a 2BP system. An example from this investigation is leaving the Sun-Earth CR3BP into heliocentric space (modeled as a 2BP) before entering the Sun-Mars CR3BP. While the spacecraft is near a planet, it is modeled in the Sun-planet CR3BP. But once it reaches a specified distance from that planet, it is modeled instead using Keplerian 2BP motion around the Sun[33]. The interface location between the two models is called the sphere of influence (SoI) since it represents where the gravitational influence of the planet becomes negligible compared to that of the Sun.

Trajectories computed in this model are best represented by using an inertial coordinate frame, centered on the focus of the 2BP, the Sun in this example. In this investigation, trajectories in the 2BP-CR3BP patched model are shown in the Sun-centered Ecliptic J2000 Inertial Frame, as described in Section 2.1.2. Although the Sun-Earth CR3BP is coplanar with this inertial frame, the Sun-Mars CR3BP system is not and Mars is considered to be located at its respective orbital inclination. The *XY*-projection of an example 2BP-CR3BP patched model system is shown in Figure 2.7.

The radius of the SoI is a design parameter dependent on the application. For this patched model, an SoI is desired such that CR3BP periodic orbits around the Lagrange points are included, demonstrated in Figure 2.8. By defining a gravitational ratio:

$$d_{SoI} = \frac{g_2}{g_1}, \quad (2.45)$$

where  $g_i$  is the gravitational acceleration of the respective primary body at a specified location, an SoI radius from the planet can be chosen so that  $d_{SoI}$  is sufficiently small, i.e., the osculating (instantaneous) orbital elements remain near constant in the CR3BP[33].

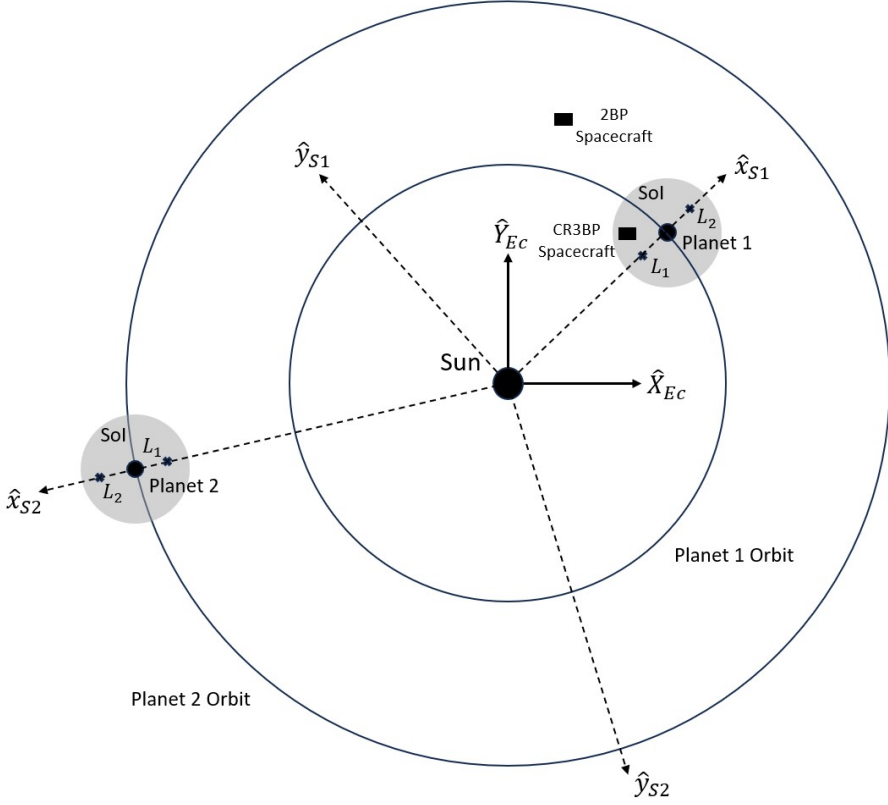


**Figure 2.7.** *XY*-Projection of the Patched 2BP-CR3BP Model

#### 2.4.2 The Blended CR3BP Model

Two CR3BP models can be blended to form a 4-body model if one of the primary bodies is present in both models. For example, a Sun-Earth CR3BP can be blended with an Earth-Moon CR3BP to form a Sun-Earth-Moon 4-body problem (here, the Earth is the common primary). This method incorporates the difference in inclinations between the two CR3BP models but is now a time-dependent model[21]. Similar to the patched 2BP-CR3BP model, the boundary between the two models is at an SoI, now around the smaller primary of the smaller CR3BP model (the Moon in this example).

Unlike the patched model above, this model is best represented in the barycentric rotating frame of the larger CR3BP model (the Sun-Earth rotating frame in this example). Since the blended model is time-dependent, the portion of the trajectory computed in the smaller

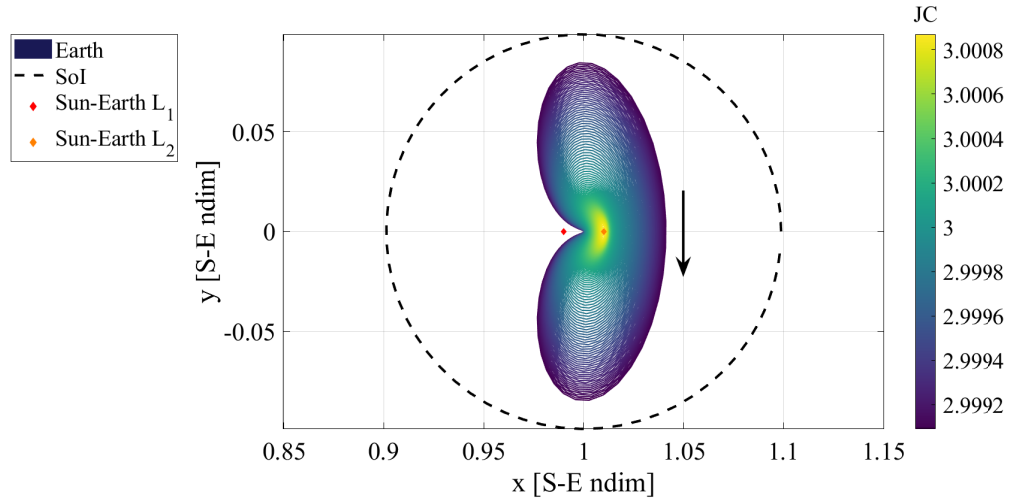


**Figure 2.8.** Patched 2BP-CR3BP sphere of influence around Earth, encompassing a large portion of the Sun-Earth  $L_2$  Lyapunov family.

CR3BP will be shifted when represented in the larger model depending on the epoch. The  $xy$ -projection of an example blended system is shown in Figure 2.9.

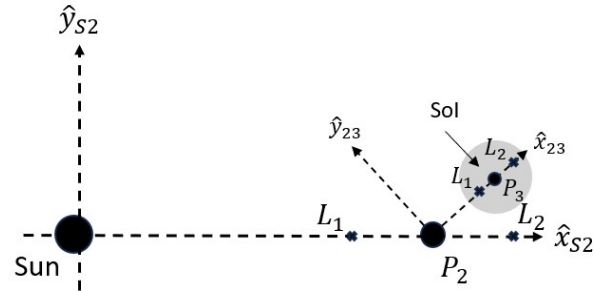


**Figure 2.9.**  $xy$ -Projection of the Blended CR3BP Model

The SoI radius used for the blended model is different from that used for the patched model. As mentioned before, this SoI is centered around the second primary of the smaller system and the gravitational accelerations being compared are the first primary of the larger

system and the smaller primary of the second system (e.g., the Sun and the Moon). A blended CR3BP SoI radius is defined as:

$$r_{SoI} = l_{12}^* \left( \frac{m_3}{m_1} \right)^{2/5}, \quad (2.46)$$

where the primaries are numbered in order of decreasing mass[41].

## 2.5 Coordinate Frame Transformations

Since the patched and blended models used in this investigation use a variety of models centered around different bodies, it is helpful to be able to view any trajectories in multiple reference frames. As mentioned previously, reference frames can be inertial or rotating, and an important component of interplanetary trajectory design is the ability to transform states and trajectories between these two types of frames. A few representative examples of coordinate frame transformations follow.

### 2.5.1 Barycentric Rotating Frame - Primary-Centric Arbitrary Inertial Frame

Most trajectories in a CR3BP are constructed in the barycentric rotating frame where Equation (2.35)-Equation (2.37) are defined (see Figure 2.1). However, it can also be beneficial to view these in an inertial frame centered on one of the primary gravitational bodies. An arbitrary inertial frame can be defined where the inertial unit vectors  $\{\hat{X}, \hat{Y}, \hat{Z}\}$  are equivalent to the rotating unit vectors  $\{\hat{x}, \hat{y}, \hat{z}\}$  at time  $t_0$  (although the frame centers may be in different locations).

The following steps will transform (nondimensionalized) states from the barycentric rotating frame to a primary-centric arbitrary inertial frame:

1. Translate the position states from barycentric to primary-centric:

$$\bar{\rho}_{P \rightarrow s/c} = \bar{\rho}_{s/c} - \bar{\rho}_P. \quad (2.47)$$

2. Rotate the states depending on time since  $t_0$

Recall that the mean motion  $n$  of the rotating frame is constant. When nondimensionalized in the CR3BP,  $\tilde{n} = 1$  and therefore the rotation angle is just  $\tau - \tau_0$ . Since the  $\hat{z}$ - and  $\hat{Z}$ -axes coincide for an arbitrary inertial frame, a simple rotation matrix can be used to rotate the position states:

$$\bar{P} = \begin{bmatrix} \cos(\tau - \tau_0) & -\sin(\tau - \tau_0) & 0 \\ \sin(\tau - \tau_0) & \cos(\tau - \tau_0) & 0 \\ 0 & 0 & 1 \end{bmatrix} \bar{\rho} = {}^I C^R \bar{\rho}, \quad (2.48)$$

where  $\bar{\rho}$  is the rotating position and  $\bar{P}$  is the inertial position.

Basic kinematics can be used to compute the velocity in the rotating frame relative to an inertial observer:

$$\frac{{}^I d\bar{\rho}}{d\tau} = \frac{{}^R d\bar{\rho}}{d\tau} + {}^I \bar{\omega}^R \times \bar{\rho} = \dot{\bar{\rho}} + \hat{z} \times \bar{\rho}, \quad (2.49)$$

where  ${}^I \bar{\omega}^R = \tilde{n} \hat{z}$  is the angular velocity relating the two frames. Therefore:

$$\frac{{}^I d\bar{\rho}}{d\tau} = (\dot{x} - y) \hat{x} + (\dot{y} + x) \hat{y} + \dot{z} \hat{z}. \quad (2.50)$$

Using the rotation matrix  ${}^I C^R$  from Equation (2.48), Equation (2.50) can be written in a matrix form and combined with the position rotation to achieve full state rotation:

$$\bar{Q} = \begin{bmatrix} {}^I C^R & \bar{0} \\ {}^I \dot{C}^R & {}^I C^R \end{bmatrix} \bar{q}, \quad (2.51)$$

where  $\bar{q}$  is the rotating state and  $\bar{Q}$  is the inertial state.

### 3. Dimensionalize the states if desired (see Section 2.3.2).

To transform a primary-centric arbitrary inertial state to a barycentric rotating state, just reverse the above states (nondimensionalizing if necessary) and invert the state rotation matrix.

### 2.5.2 Barycentric Rotating Frame - Ecliptic J2000 Inertial Frame

When designing a trajectory across multiple systems, it is often useful to view each part of the trajectory in a common inertial reference frame. In this investigation, the Earth Ecliptic J2000 inertial frame, introduced in Section 2.1.2 (Figure 2.2), is used as the common frame for interplanetary trajectories.

The transformation between barycentric rotating frame states and a primary-centric Ecliptic J2000 inertial frame states follows a similar process to the arbitrary inertial frame. However, since this frame is defined by a particular epoch (January 1, 2000), the frame rotation is epoch-dependent:

1. To properly compare the rotating frame to the Ecliptic J2000 inertial frame, the location of the second primary in its orbit at each epoch of the trajectory is needed. This is obtained by retrieving the orbital elements of the second primary at a selected initial epoch from SPICE[35]. These orbital elements are then modified to match the CR3BP orbit assumptions ( $a = l^*$  and  $e = 0$ ). Since the mean motion/angular velocity in the CR3Bp is constant at  $\tilde{n} = 1$ :

$$\theta = \tau - \tau_0 + \theta_0, \quad (2.52)$$

where  $\theta_0$  is the true anomaly at the initial epoch  $t = 0$  obtained from SPICE. These updated orbital elements are then used to calculate the full state vector (in dimensional units) of the second primary relative to the first using Equation (2.22)-Equation (2.28).

2. Dimensionalize the trajectory states, times, and angular velocity (see Section 2.3.2).
3. At each time, translate the position states from barycentric to primary-centric using Equation (2.47) (note that dimensional values should be used).
4. Define the instantaneous state rotation matrix using the second primary's Ecliptic J2000 state vector and angular momentum  $\bar{h}$  (Equation (2.6)) at each time:

$$\hat{x} = \frac{\bar{R}_{P_1 \rightarrow P_2}}{|\bar{R}_{P_1 \rightarrow P_2}|}, \quad (2.53)$$

$$\hat{z} = \frac{\bar{h}}{|\bar{h}|}, \quad (2.54)$$

$$\hat{y} = \hat{z} \times \hat{x}, \quad (2.55)$$

$${}^{Ec}C^R = \begin{bmatrix} \hat{x} & \hat{y} & \hat{z} \end{bmatrix}. \quad (2.56)$$

The full state rotation matrix can be found through the same process used in Section 2.5.1, using a dimensional angular velocity:

$${}^{Ec}\dot{C}^R = \begin{bmatrix} n\hat{y} & -n\hat{x} & \bar{0} \end{bmatrix}. \quad (2.57)$$

in Equation (2.51) with dimensional values.

5. Nondimensionalize the states if desired.

States can be transformed from a primary-centric Ecliptic J2000 inertial frame to a barycentric rotating frame by reversing the above steps and inverting the state rotation matrix. This becomes a useful tool when designing interplanetary trajectories using multi-body dynamics.

### 3. CR3BP DYNAMICAL STRUCTURES

As mentioned in the previous chapter, there is no analytical solution to the CR3BP. Instead, trajectories are propagated using numerical methods. Various numerical techniques are applied to find existing dynamical structures in the model, such as periodic orbits and invariant manifolds, and obtain corresponding initial conditions for propagation. These include differential corrections, natural parameter continuation, eigen decomposition, and Poincaré mapping.

#### 3.1 Differential Corrections

Differential corrections are used to compute solutions in targeting problems that satisfy the provided constraints on the initial condition and the trajectory arc. To do so, it is necessary to be able to relate downstream states to the initial condition.

##### 3.1.1 State Transition Matrix

The state transition matrix (STM) relates variations in an initial state,  $\bar{q}_0 = \bar{q}(t_0)$ , to variations in a downstream state  $\bar{q}(t)$ . Starting from a first-order Taylor series expansion about the baseline trajectory arc, the linear variational equation is derived:

$$\partial \dot{\bar{q}}(t) = A(t) \partial \bar{q}(t), \quad (3.1)$$

where  $A(t)$  is the Jacobian matrix for the equations of motion with respect to the state at time  $t$ . A full derivation for the CR3BP  $A(t)$  matrix can be found in Zimovan, but the result is given here[37]:

$$A(t) = \begin{bmatrix} \frac{\partial x}{\partial x_0} & \frac{\partial x}{\partial y_0} & \frac{\partial x}{\partial z_0} & \frac{\partial x}{\partial \dot{x}_0} & \frac{\partial x}{\partial \dot{y}_0} & \frac{\partial x}{\partial \dot{z}_0} \\ \frac{\partial y}{\partial x_0} & \frac{\partial y}{\partial y_0} & \frac{\partial y}{\partial z_0} & \frac{\partial y}{\partial \dot{x}_0} & \frac{\partial y}{\partial \dot{y}_0} & \frac{\partial y}{\partial \dot{z}_0} \\ \frac{\partial z}{\partial x_0} & \frac{\partial z}{\partial y_0} & \frac{\partial z}{\partial z_0} & \frac{\partial z}{\partial \dot{x}_0} & \frac{\partial z}{\partial \dot{y}_0} & \frac{\partial z}{\partial \dot{z}_0} \\ \frac{\partial \dot{x}}{\partial x_0} & \frac{\partial \dot{x}}{\partial y_0} & \frac{\partial \dot{x}}{\partial z_0} & \frac{\partial \dot{x}}{\partial \dot{x}_0} & \frac{\partial \dot{x}}{\partial \dot{y}_0} & \frac{\partial \dot{x}}{\partial \dot{z}_0} \\ \frac{\partial \dot{y}}{\partial x_0} & \frac{\partial \dot{y}}{\partial y_0} & \frac{\partial \dot{y}}{\partial z_0} & \frac{\partial \dot{y}}{\partial \dot{x}_0} & \frac{\partial \dot{y}}{\partial \dot{y}_0} & \frac{\partial \dot{y}}{\partial \dot{z}_0} \\ \frac{\partial \dot{z}}{\partial x_0} & \frac{\partial \dot{z}}{\partial y_0} & \frac{\partial \dot{z}}{\partial z_0} & \frac{\partial \dot{z}}{\partial \dot{x}_0} & \frac{\partial \dot{z}}{\partial \dot{y}_0} & \frac{\partial \dot{z}}{\partial \dot{z}_0} \end{bmatrix} = \begin{bmatrix} 0 & 0 & 0 & 1 & 0 & 0 \\ 0 & 0 & 0 & 0 & 1 & 0 \\ 0 & 0 & 0 & 0 & 0 & 1 \\ \frac{\partial U}{\partial x \partial x} & \frac{\partial U}{\partial x \partial y} & \frac{\partial U}{\partial x \partial z} & 0 & 2n & 0 \\ \frac{\partial U}{\partial y \partial x} & \frac{\partial U}{\partial y \partial y} & \frac{\partial U}{\partial y \partial z} & -2n & 0 & 0 \\ \frac{\partial U}{\partial z \partial x} & \frac{\partial U}{\partial z \partial y} & \frac{\partial U}{\partial z \partial z} & 0 & 0 & 0 \end{bmatrix}, \quad (3.2)$$

$$\frac{\partial U}{\partial x \partial x} = 1 - \frac{1-\mu}{d^3} - \frac{\mu}{r^3} + \frac{3(1-\mu)(x+\mu)^2}{d^5} + \frac{3\mu(x-1+\mu)^2}{r^5}, \quad (3.3)$$

$$\frac{\partial U}{\partial x \partial y} = \frac{\partial U}{\partial y \partial x} = \frac{3(1-\mu)(x+\mu)y}{d^5} + \frac{3\mu(x-1+\mu)y}{r^5}, \quad (3.4)$$

$$\frac{\partial U}{\partial x \partial z} = \frac{\partial U}{\partial z \partial x} = \frac{3(1-\mu)(x+\mu)z}{d^5} + \frac{3\mu(x-1+\mu)z}{r^5}, \quad (3.5)$$

$$\frac{\partial U}{\partial y \partial y} = 1 - \frac{1-\mu}{d^3} - \frac{\mu}{r^3} + \frac{3(1-\mu)y^2}{d^5} + \frac{3\mu y^2}{r^5}, \quad (3.6)$$

$$\frac{\partial U}{\partial y \partial z} = \frac{\partial U}{\partial z \partial y} = \frac{3(1-\mu)yz}{d^5} + \frac{3\mu yz}{r^5}, \quad (3.7)$$

$$\frac{\partial U}{\partial z \partial z} = -\frac{1-\mu}{d^3} - \frac{\mu}{r^3} + \frac{3(1-\mu)z^2}{d^5} + \frac{3\mu z^2}{r^5}. \quad (3.8)$$

The solution to Equation (3.1):

$$\partial \bar{q}(t) = \frac{\partial \bar{q}(t)}{\partial \bar{q}_0} \partial \bar{q}_0, \quad (3.9)$$

can be rearranged to provide the STM  $\Phi(t, t_0)$ :

$$\Phi(t, t_0) = \frac{\partial \bar{q}(t)}{\partial \bar{q}_0}. \quad (3.10)$$

The equation of motion for the STM can be appended to the CR3BP equations of motion when propagating:

$$\dot{\Phi}(t, t_0) = A(t)\Phi(t, t_0), \quad (3.11)$$

with an initial condition of  $\Phi(t_0, t_0) = I_{6 \times 6}$ .

### 3.1.2 Multi-Variable Newton-Raphson Method

Targeting problems require iterative approaches where an initial guess is updated until it meets a set of constraints to solve a boundary value problem. This investigation uses a multi-variable Newton-Raphson method as a differential corrections process for single-shooting targeting problems, applying analytical or numerical partial derivatives of constraints with respect to the initial conditions.

If  $\bar{X}$  is the free variable vector and  $\bar{F}(\bar{X})$  is the constraint vector, dependent on the free variables, then the goal of the targeting problem is to find  $\bar{X}$  such that  $\bar{F}(\bar{X}) = \bar{0}$  (to a chosen tolerance). Example free variable and constraint vectors will be introduced in future sections of this chapter and document. Under the Newton-Raphson method, the update equation is again provided by a first-order Taylor series expansion about the initial condition  $\bar{X}_0$ :

$$\bar{F}(\bar{X}) = \bar{F}(\bar{X}_0) + DF(\bar{X}_0)(\bar{X} - \bar{X}_0) = \bar{0}, \quad (3.12)$$

where  $DF(\bar{X})$  is the Jacobian matrix containing the partial derivatives of the constraint vector with respect to the free variable vector.

With this update equation, the next iteration on the initial conditions can be computed. If the number of free variables matches the number of constraints:

$$\bar{X} = \bar{X}_0 - DF(\bar{X}_0)^{-1}\bar{F}(\bar{X}_0), \quad (3.13)$$

and this becomes the new iteration of the initial conditions. Ideally, upon each iteration, the norm of the constraint vector should approach closer to the tolerance. If the number of free variables is greater than the number of constraints, a minimum-norm solution can be used:

$$\bar{X} = \bar{X}_0 - DF(\bar{X}_0)^T (DF(\bar{X}_0)DF(\bar{X}_0)^T)^{-1} \bar{F}(\bar{X}_0). \quad (3.14)$$

When the number of free variables is less than the number of constraints, a least squares solution can be used, but that is not addressed in this investigation.

As a simple targeting example, consider the following planar boundary value problem in Figure 3.1. The objective is to vary the initial velocity and time-of-flight (TOF) to target a desired final position  $\bar{\rho}_d$ . This results in a free variable vector:

$$\bar{X} = \begin{bmatrix} \dot{x}_0 & \dot{y}_0 & \tau \end{bmatrix}^T, \quad (3.15)$$

and constraint vector:

$$\bar{F}(\bar{X}) = \begin{bmatrix} x_f - x_d & y_f - y_d \end{bmatrix}^T = \bar{0}. \quad (3.16)$$

The Jacobian matrix is comprised of the partial derivatives of the constraint vector with respect to the free variable vector, in this case, a combination of the STM and time derivatives:

$$DF(\bar{X}) = \begin{bmatrix} \frac{\partial(x_f - x_d)}{\partial \dot{x}_0} & \frac{\partial(x_f - x_d)}{\partial \dot{y}_0} & \frac{\partial(x_f - x_d)}{\partial \tau} \\ \frac{\partial(y_f - y_d)}{\partial \dot{x}_0} & \frac{\partial(y_f - y_d)}{\partial \dot{y}_0} & \frac{\partial(y_f - y_d)}{\partial \tau} \end{bmatrix} = \begin{bmatrix} \phi_{14} & \phi_{15} & \dot{x}_f \\ \phi_{24} & \phi_{25} & \dot{y}_f \end{bmatrix}, \quad (3.17)$$

where  $\phi$  are elements of the STM of the propagated arc. These vectors and the Jacobian matrix can then be used in Equation (3.14) to iteratively solve for the free variable vector that satisfies the constraint vector and solves the provided boundary value problem.

### 3.1.3 Central Difference Method

The Newton-Raphson method uses partial derivatives to solve a targeting problem iteratively. These partial derivatives can be provided analytically (like in the previous example) or numerically using an approximation method such as central differencing. The numerical

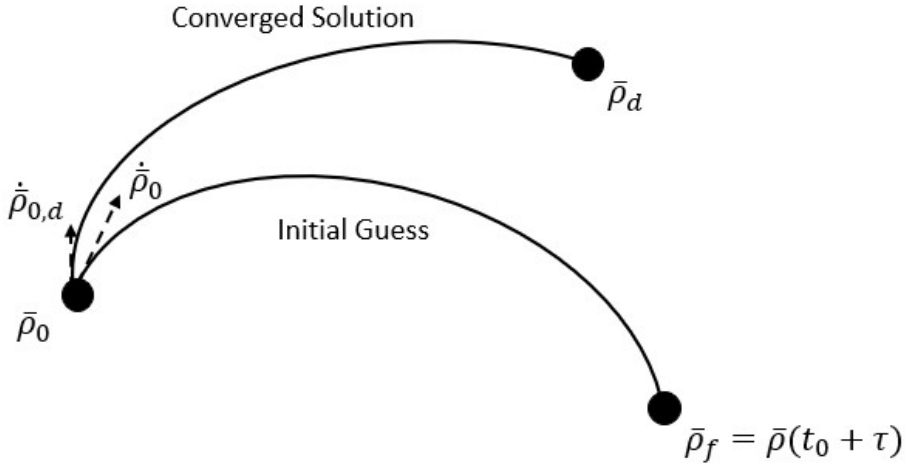


**Figure 3.1.** Simple Targeting Example.

approach is used in this investigation to check analytical partial derivatives or when the analytical partials are overly complicated.

The central difference method approximates the slope of the solution at discretized points just before and after the initial condition:

$$D\bar{F}_i(\bar{X}_0) = \frac{\partial \bar{F}(\bar{X}_0)}{\partial X_i} = \frac{\bar{F}(X_i + \kappa) - \bar{F}(X_i - \kappa)}{2\kappa}, \quad (3.18)$$

where  $X_i$  is one of the components of the free variable vector and  $\kappa$  is a small perturbation (this investigation uses the square root of the machine tolerance,  $\sqrt{\epsilon}$ ). Each variable in the free variable vector is perturbed in both directions by  $\kappa$ , one at a time, and the constraint vector is evaluated at each new free variable vector and substituted into Equation (3.18) above. Perturbing all of the free variables individually makes up the numerical Jacobian matrix:

$$DF(\bar{X}_0) = \begin{bmatrix} D\bar{F}_1(\bar{X}_0) & \dots & D\bar{F}_m(\bar{X}_0) \end{bmatrix}. \quad (3.19)$$

### 3.2 Periodic Orbits

Using the multi-variable Newton-Raphson scheme described above, periodic solutions can be targeted in a CR3BP system. In the CR3BP, these periodic solutions exist as members

of families that share similar geometric characteristics. Some of these orbit families are symmetric about a plane or axis in the rotating frame and this information can be utilized in the targeting process. In addition, the initial conditions for these families can be obtained through a variety of methods including linear variational equations about the Lagrange points and bifurcations from other orbit families. All of the orbit families used in this investigation and shown here were selected for their relative instability in the Earth-Moon CR3BP. For some example initial conditions for these orbit families and others, see NASA Jet Propulsion Laboratory's CR3BP orbit database[42].

### 3.2.1 Lyapunov Orbits

#### A Lyapunov Targeter

To demonstrate the periodic orbit targeting process, the Newton-Raphson scheme will be used to solve for a periodic orbit in the  $xy$ -plane of the rotating frame around the first Lagrange point. This family of solutions is known as the  $L_1$  Lyapunov family and they are symmetric about the  $xz$ -plane. Therefore, instead of targeting the full orbit, it is only necessary to target half of it, from one perpendicular crossing of the  $xz$ -plane to the next. To target one of these orbits at a specified energy level (Jacobi constant), consider the free variable vector:

$$\bar{X} = \begin{bmatrix} x_0 & \dot{y}_0 & \tau \end{bmatrix}^T. \quad (3.20)$$

Since the boundary value problem being solved starts from a perpendicular crossing, it is only necessary to allow  $x_0$  and  $\dot{y}_0$  to vary as the rest of the initial states will all be 0. In Equation (3.20),  $\tau$  represents the nondimensional propagation time (TOF) of the initial conditions. To target another perpendicular crossing for the endpoint of the trajectory arc, the following constraint vector is used:

$$\bar{F}(\bar{X}) = \begin{bmatrix} y_f & \dot{x}_f & C - C_d \end{bmatrix}^T = \bar{0}, \quad (3.21)$$

where  $C$  is the Jacobi constant of the propagated arc and  $C_d$  is the desired Jacobi constant. The Jacobian matrix is then comprised of partial derivatives from the STM, time derivatives, and partial derivatives of the Jacobi constant with respect to state variables:

$$DF(\bar{X}) = \begin{bmatrix} \frac{\partial y_f}{\partial x_0} & \frac{\partial y_f}{\partial \dot{y}_0} & \frac{\partial y_f}{\partial \tau} \\ \frac{\partial \dot{x}_f}{\partial x_0} & \frac{\partial \dot{x}_f}{\partial \dot{y}_0} & \frac{\partial \dot{x}_f}{\partial \tau} \\ \frac{\partial(C-C_d)}{\partial x_0} & \frac{\partial(C-C_d)}{\partial \dot{y}_0} & \frac{\partial(C-C_d)}{\partial \tau} \end{bmatrix} = \begin{bmatrix} \phi_{21} & \phi_{25} & \dot{y}_f \\ \phi_{41} & \phi_{45} & \ddot{x}_f \\ 2x_0 - \frac{2(x_0+\mu)(1-\mu)}{d^3} - \frac{2\mu(x_0-1+\mu)}{r^3} & -2\dot{y}_0 & 0 \end{bmatrix}. \quad (3.22)$$

This Jacobian matrix can then be used with Equation (3.13) to iteratively solve for the free variable vector  $\bar{X}$  that solves the provided problem. This provides the initial state and half of the propagation time for a periodic Lyapunov orbit.

### Lyapunov Initial Guess

An initial guess for a Lyapunov orbit close to the Lagrange point can come from variational equations of motion, linearized about the equilibrium point:

$$x_0 = x_L + \xi, \quad (3.23)$$

$$\dot{y}_0 = -\beta_3 \xi s, \quad (3.24)$$

where  $\xi$  is a chosen variation from the  $x$ -value of the Lagrange point,

$$\beta_1 = 2 - \frac{\frac{\partial U}{\partial x \partial x} + \frac{\partial U}{\partial y \partial y}}{2}, \quad (3.25)$$

$$\beta_2 = \sqrt{-\frac{\partial U}{\partial x \partial x} \frac{\partial U}{\partial y \partial y}}, \quad (3.26)$$

$$s = \sqrt{\beta_1 + \sqrt{\beta_1^2 + \beta_2^2}}, \quad (3.27)$$

$$\beta_3 = \frac{s^2 + \frac{\partial U}{\partial x \partial x}}{2s}. \quad (3.28)$$

The last part of the initial guess for the free variable vector is the half-period of the orbit  $\tau$ . This can be approximated by propagating the initial state guess until it reaches the  $x$ -axis.

### Converged Lyapunov Orbit

The linear variational equations only approximate the dynamics very close to the Lagrange point. Using  $\xi = 0.005$  as the initial variation in the  $x$ -direction from the  $L_1$  Lagrange point in the Earth-Moon system:

$$\bar{X}_0 = \begin{bmatrix} 0.841915 & -0.0418614 & 1.29755 \end{bmatrix}^T, \quad (3.29)$$

and from the guess for the initial state,  $C_d = 3.186877$ . This initial free variable guess is propagated using the CR3BP equations of motion and is represented by the dashed curve in Figure 3.2. After targeting a perpendicular crossing using the targeter described above, the solution can be propagated (for  $2\tau$ ) to obtain the full periodic Lyapunov orbit, shown as a closed, solid curve in Figure 3.2. Note that while the energy of the converged solution matches that of the initial guess, the  $x$ - and  $y$ -values have shifted slightly.

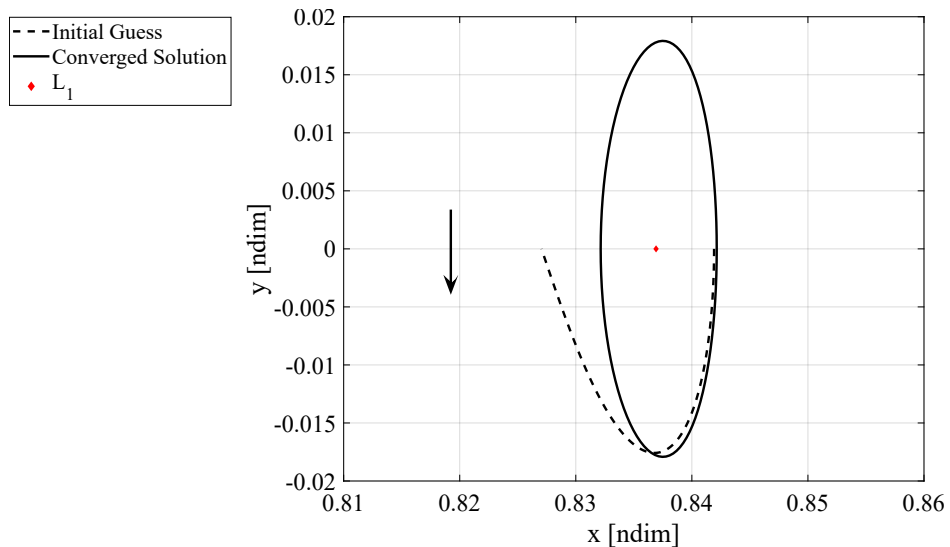


**Figure 3.2.** Converged periodic Lyapunov orbit in the Earth-Moon barycentric rotating frame.

## Natural Parameter Continuation

The process described above produces a single solution near the Lagrange point. To compute more solutions (orbits) in the family, especially further away from the Lagrange point where the linear variational equations no longer apply, converged solutions can be used in a continuation scheme to find other family members. This investigation utilizes natural parameter continuation, where one of the parameters of a converged solution is changed by a small amount. This new guess for an orbit is then converged, and a new solution is obtained. This continuation process can then be repeated until the scheme reaches a natural/dynamical end or a desired orbit is reached. Natural parameters of the orbit include (but are not limited to) components of the initial state, the period, or the Jacobi constant. Figure 3.3 shows a large portion of the  $L_1$  Lyapunov family in the Earth-Moon system, continued in Jacobi constant from the orbit in Figure 3.2. Lyapunov families also exist about  $L_2$  and  $L_3$  and can be computed via the same process. Since  $L_2$  Lyapunovs are also used in this investigation, they are shown in Figure 3.4.

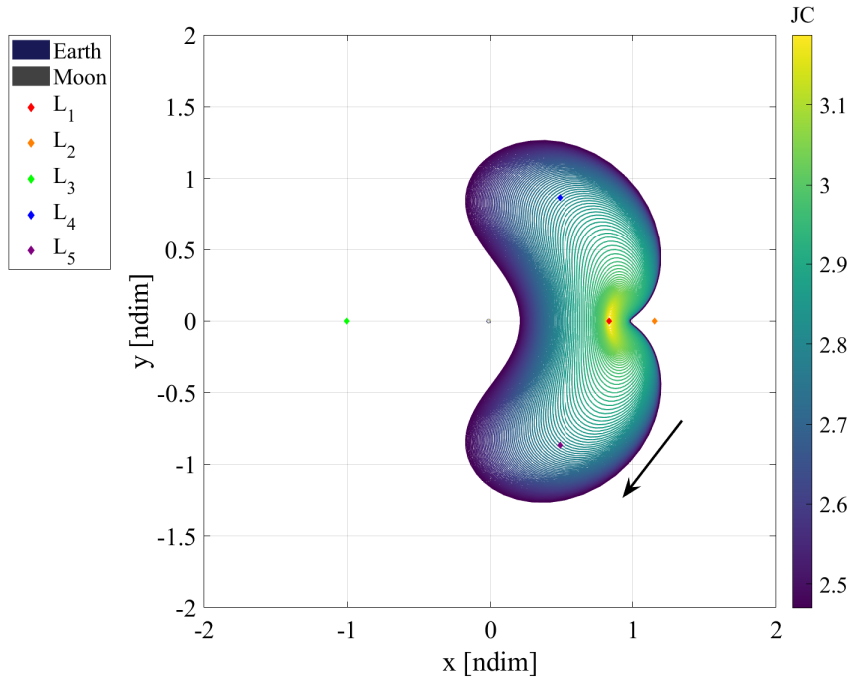


**Figure 3.3.** Earth-Moon  $L_1$  Lyapunov orbit family.

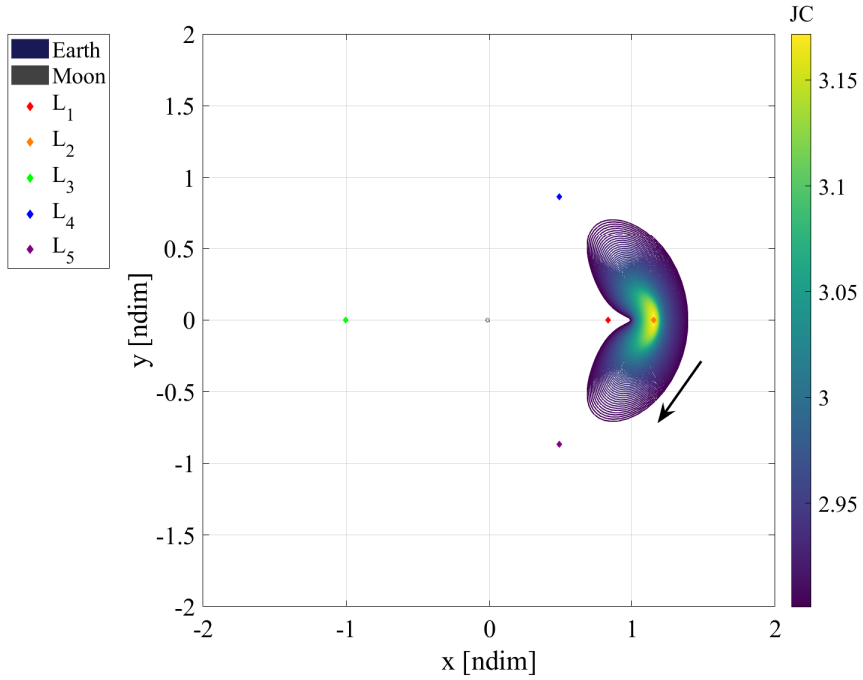


**Figure 3.4.** Earth-Moon  $L_2$  Lyapunov orbit family.

### 3.2.2 Orbital Stability

Before discussing other orbit families, it is important to introduce orbital stability as it leads to orbit family bifurcations and another way to generate new orbit families. Orbital stability helps describe the characteristics of the orbit and the surrounding dynamics. The stability of an orbit also determines the best transfer design strategies to minimize the  $\Delta v$  cost.

#### Monodromy Matrix

The STM of one revolution of a periodic orbit in the CR3BP,  $\Phi(t_0 + \mathbb{P}, t_0)$ , is called the monodromy matrix, and discretely maps the linear growth of perturbations. Some useful properties of the monodromy matrix are that it is symplectic, it has a determinant of 1, and its eigenvalues occur in reciprocal pairs[43]. Since the trajectory is periodic, two of the eigenvalues (one pair) are always 1, denoted the trivial pair, and correspond to the trajectory's periodicity and membership in a family of solutions.

The stability of the orbit is characterized by the remaining two pairs of eigenvalues. Since the monodromy matrix is a discrete-time mapping, eigenvalues that lie within the unit circle (magnitude less than 1) in the complex plane are stable and those outside the unit circle are unstable. Perturbations in the stable subspace will flow back toward the orbit, while perturbations in the unstable subspace will depart the orbit. If the eigenvalues lie directly on the unit circle, then the corresponding flow is in the center subspace and remains bounded around the orbit. When the stability of an eigenvalue pair changes, it can indicate a change in the characteristics of orbits within a family and sometimes leads to a bifurcation in the family, discussed later.

The overall stability of the orbit is then determined by all of the eigenvalues of its monodromy matrix. If any of the eigenvalues are unstable (greater than 1), then the orbit is considered linearly unstable. Note that the existence of an unstable eigenvalue implies the existence of a stable eigenvalue because of the reciprocal pairs. Otherwise, the orbit is considered marginally stable and all of the eigenvalues reside on the unit circle. Throughout an orbit family, while the stability of the members may change, the eigenvalues experience a smooth (but not necessarily monotonic) evolution.

## Stability Index

A variety of metrics exist to more succinctly portray the stability of orbits, rather than viewing all of the eigenvalues. One such metric is a stability index, of which there are a variety of definitions whose usefulness vary depending on the application. In this investigation, the focus is on just the overall stability of the orbit — whether it is unstable or marginally stable — so a metric that can quickly differentiate between these behaviors suffices. Therefore, the following definition is used[44]:

$$\varsigma = \|\bar{\lambda}\|_\infty, \quad (3.30)$$

where  $\bar{\lambda}$  is a vector of the eigenvalues of the monodromy matrix and the infinity norm returns the magnitude of the largest (magnitude) element of the vector. With this definition,  $\varsigma > 1$  indicates an unstable orbit and  $\varsigma = 1$  indicates one that is marginally stable. Other definitions can be found in Zimovan Spreen's work[43].

Like the eigenvalues themselves, the evolution of the stability index over an orbit family is smooth. Figure 3.5 shows the stability indices for the members of the  $L_1$  (a) and  $L_2$  (b) Lyapunov families from Figure 3.3 and Figure 3.4. A larger stability index means that the orbit has a higher instability and perturbations will experience faster growth. Note that all of the members of both of these families are unstable. However, there are stability changes among individual eigenvalues within each family that can lead to bifurcations.

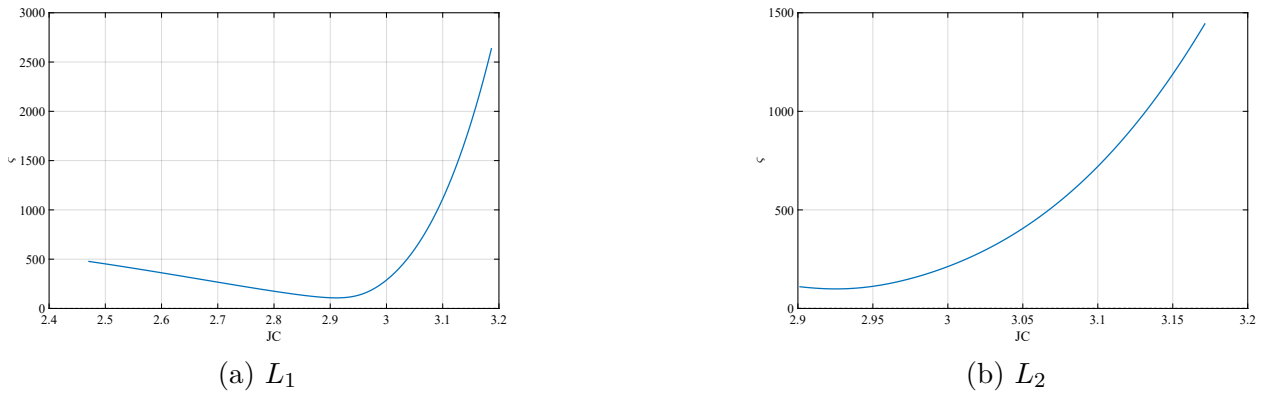


**Figure 3.5.** Earth-Moon Lyapunov family stability index evolution.

### Time Constant

Another useful metric of stability is the time constant, which approximates how long it takes, in time units or in orbit revolutions, for a perturbation to grow by a factor of e:

$$\Upsilon = \frac{1}{\ln \zeta}, \quad (3.31)$$

where the dimensions are orbit revolutions. This equation can be multiplied by the period of the orbit  $\mathbb{P}$  to produce the time constant in time units. Figure 3.6 shows the time constant evolution of both Lyapunov families in orbit revolutions. Note that a larger time constant indicates that it takes longer for a perturbation, meaning that the orbit is less unstable, and a marginally stable orbit has an infinite time constant.

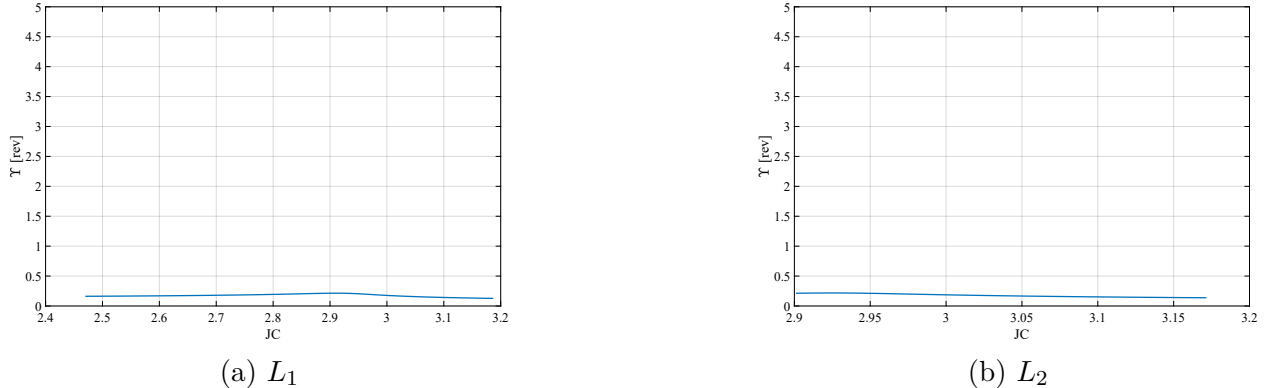


**Figure 3.6.** Earth-Moon Lyapunov family time constant evolution.

## Bifurcations

Within the context of the CR3BP, bifurcation theory can be used to detect changes in orbit stability characteristics within a family that can sometimes lead to the generation of orbit families that branch off from the original family. Zimovan Spreen provides a more thorough analysis of how bifurcation theory can be applied to the CR3BP so only the information most relevant to this investigation will be provided here[43].

Two main bifurcation types are relevant to the orbits used in this analysis:

- **Tangent bifurcations** occur when an eigenvalue pair goes to 1, either from the unit circle or the real axis. With a cyclic fold tangent bifurcation, which occurs at an extremum in the Jacobi constant, the stability of the eigenvalues changes, but there is no new family of solutions created. Pitchfork tangent bifurcations produce two new families that have the same stability as the original family. The last subtype, transcritical tangent bifurcations, produce a new family and a change in the eigenvalue stability of the original family.
- **Period-multiplying bifurcations** occur when an eigenvalue pair reaches a root of 1 ( $\sqrt{1}$ ,  $\sqrt[3]{1}$ ,  $\sqrt[7]{1}$ , etc.). In general, this produces a new family with a period of  $m$  times the original, but not necessarily a change in stability. The most commonly seen subtype is the period-doubling bifurcation, where the pair of eigenvalues meets at  $-1$ ,

either from the unit circle or the real axis. This results in a change in the stability of the eigenvalues and a new family that has double the period of the original family.

There are other methods of detecting bifurcations beyond examining the evolution of the eigenvalues such as Broucke stability or bifurcation diagrams that are also described in Zimovan Spreen[43].

### New Family Generation from Bifurcation

To find the initial conditions for an orbit in a new family from a bifurcation, first, the precise bifurcating orbit (within a tolerance) must be obtained. This can be done through a simple bisection algorithm. The Jacobian matrix of this bifurcating orbit should have an additional nullspace compared to the other orbits in the family since another pair of eigenvalues (besides the trivial pair) is at 1. Note that for a period-multiplying bifurcation, the orbit must be propagated for  $m$  revolutions to obtain the proper Jacobian matrix. When this is the case, one of the nullspace vectors points in the direction of continuing the old family, while the other vector indicates a direction for the new family.

Using a singular value decomposition (SVD), this new nullspace direction can be identified by the right singular vector of  $DF$  that corresponds to the additional nullspace. Stepping in this direction from the bifurcating orbit's initial conditions and correcting for a periodic solution should result in a new periodic orbit belonging to the new family. This approach is also known as pseudo-arc length continuation and the new member can then be continued using any scheme to obtain the new family.

#### 3.2.3 Halo Orbits

##### A Halo Targeter

Similar to Lyapunov orbits, halo orbits are symmetric about the  $xz$ -plane although they are spatial in the rotating frame and not limited to the  $xy$ -plane. This again allows for targeting only half of the periodic orbit, from one perpendicular crossing to the next. Since

there is now a  $z$ -component to the orbits, it is helpful to introduce a new free variable and constraint for the halo targeter:

$$\bar{X} = \begin{bmatrix} x_0 & z_0 & \dot{y}_0 & \tau \end{bmatrix}^T, \quad (3.32)$$

$$\bar{F}(\bar{X}) = \begin{bmatrix} y_f & \dot{x}_f & \dot{z}_f & C - C_d \end{bmatrix}^T = \bar{0}, \quad (3.33)$$

$$DF(\bar{X}) = \begin{bmatrix} \phi_{21} & \phi_{23} & \phi_{25} & \dot{y}_f \\ \phi_{41} & \phi_{43} & \phi_{45} & \ddot{x}_f \\ \phi_{61} & \phi_{63} & \phi_{65} & \ddot{z}_f \\ 2x_0 - \frac{2(x_0 + \mu)(1 - \mu)}{d^3} - \frac{2\mu(x_0 - 1 + \mu)}{r^3} & -\frac{2z_0(1 - \mu)}{d^3} - \frac{2z_0\mu}{r^3} & -2\dot{y}_0 & 0 \end{bmatrix}. \quad (3.34)$$

The result of this targeting will provide the initial state ( $y_0 = \dot{x}_0 = \dot{z}_0 = 0$ ) and half of the propagation time for a periodic halo orbit.

## Converged Halo Families

The initial guess for a halo orbit comes from a bifurcating orbit in a Lyapunov family. At  $C \approx 3.174352$ , the  $L_1$  Lyapunov family has a tangent bifurcation and the  $L_1$  halo family is formed. The pseudo-arc length method for generating an initial guess can be used as described above to obtain the initial guess for the initial state, propagation time, and Jacobi constant. Using natural parameter continuation, more of the family is produced, shown in Figure 3.7. Since the Lyapunov orbit can bifurcate above or below the  $xy$ -plane, two halves of the family are formed. Figure 3.7 is denoted the  $L_1$  southern halos because most of the orbit is spent south (in the rotating frame) of the Moon.

Figure 3.8 shows the  $L_2$  southern halo family, generated in the same way as the  $L_1$  halos but from the  $L_2$  Lyapunov family. Note that these halo families are not monotonic in Jacobi constant. The stability indices for both families are shown in Figure 3.9.  $L_3$  halos also exist, but are not used in this investigation.

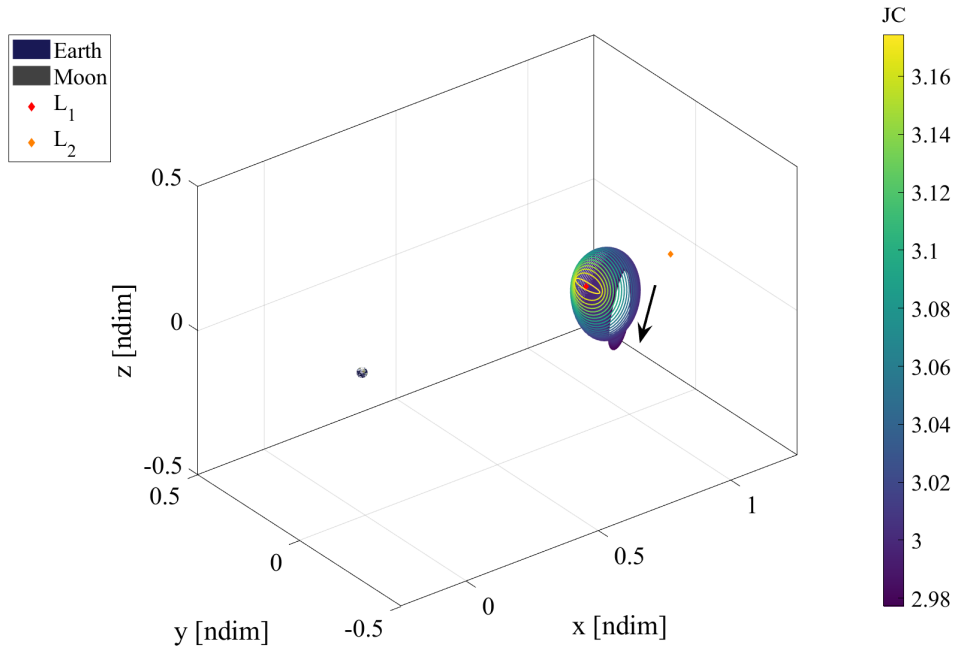


**Figure 3.7.** Earth-Moon  $L_1$  southern halo orbit family.

### 3.2.4 Butterfly Orbits

Butterfly orbits is another name for the  $P_2HO_1 L_2$  orbit family: the period-doubling bifurcation from the  $L_2$  halo family with the smallest perilune[43]. Conveniently, the same targeter can be used for this family as with the halos above. The same pseudo-arc length method can also be used to obtain the initial guess from the bifurcating halo, remembering to double the period of the orbit first. A portion of this family is shown in Figure 3.10 and the stability indices are shown in Figure 3.11.

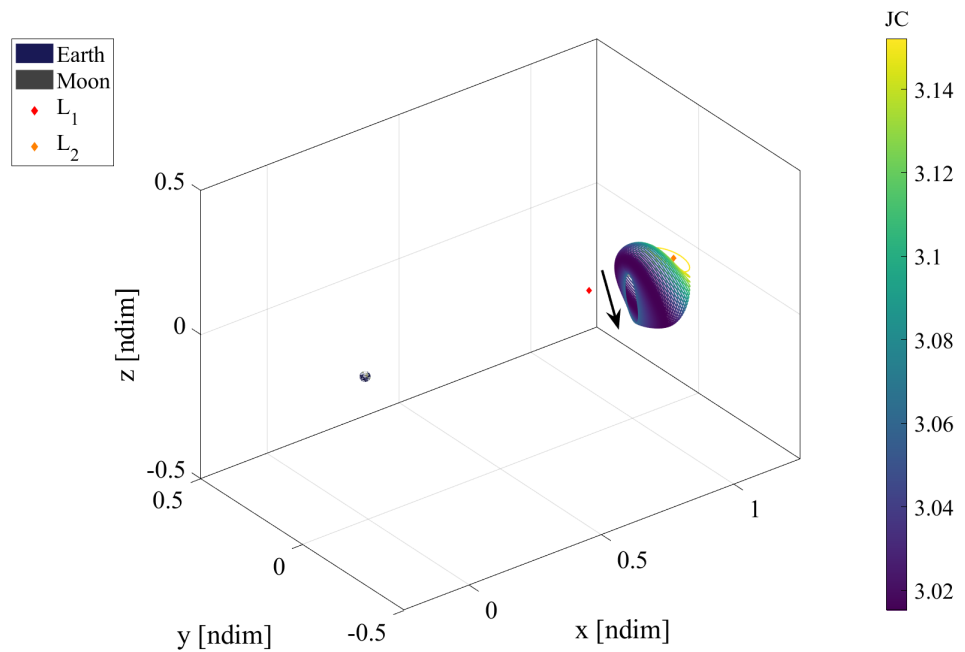


**Figure 3.8.** Earth-Moon  $L_2$  southern halo orbit family.

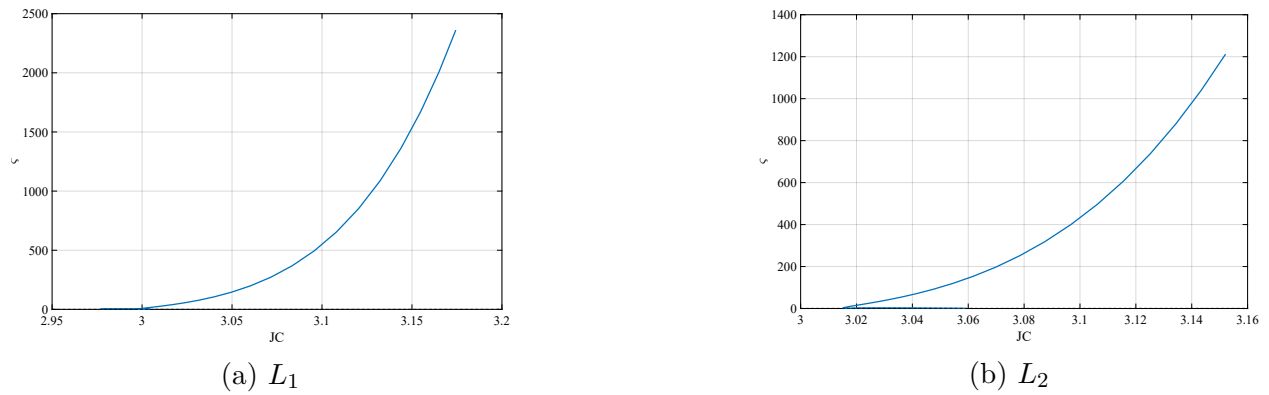


**Figure 3.9.** Earth-Moon Halo family stability index evolution.

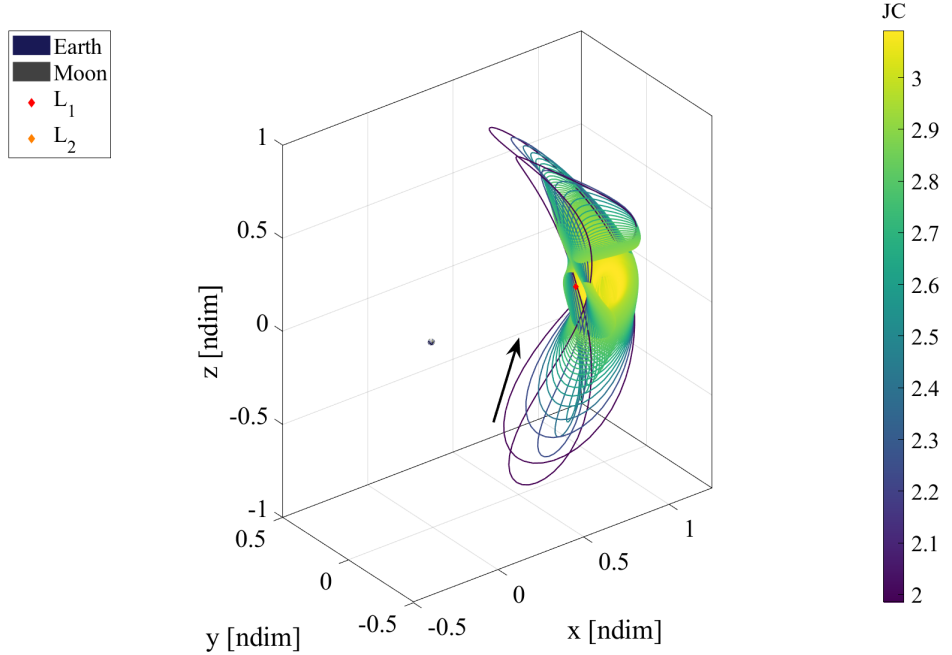


**Figure 3.10.** Earth-Moon butterfly family.

### 3.2.5 Axial Orbits

#### An Axial Targeter

Another spatial orbit family, the axial orbits, comes from a different tangent bifurcation in the Lyapunov families. These orbits have symmetry only about the  $x$ -axis; therefore, the perpendicular crossings must lie on the  $x$ -axis, unlike the halo orbits:

$$\bar{X} = \begin{bmatrix} x_0 & \dot{y}_0 & \dot{z}_0 & \tau \end{bmatrix}^T, \quad (3.35)$$

$$\bar{F}(\bar{X}) = \begin{bmatrix} y_f & z_f & \dot{x}_f & C - C_d \end{bmatrix}^T = \bar{0}, \quad (3.36)$$

$$DF(\bar{X}) = \begin{bmatrix} \phi_{21} & \phi_{25} & \phi_{26} & \dot{y}_f \\ \phi_{31} & \phi_{35} & \phi_{36} & \dot{z}_f \\ \phi_{41} & \phi_{45} & \phi_{46} & \ddot{x}_f \\ 2x_0 - \frac{2(x_0 + \mu)(1 - \mu)}{d^3} - \frac{2\mu(x_0 - 1 + \mu)}{r^3} & -2\dot{y}_0 & -2\dot{z}_0 & 0 \end{bmatrix}. \quad (3.37)$$

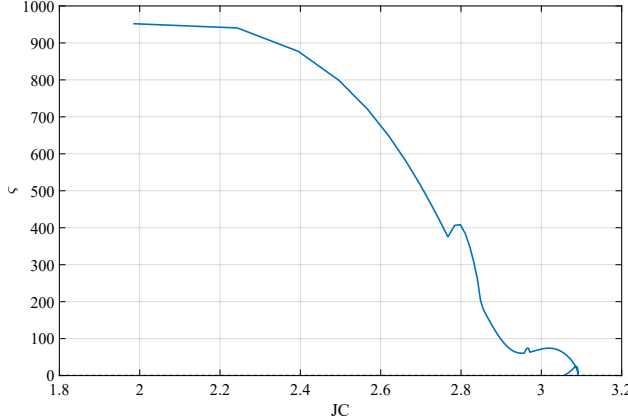


**Figure 3.11.** Earth-Moon butterfly family stability index evolution.

The result of this targeting will provide the initial state ( $y_0 = z_0 = \dot{x}_0 = 0$ ) and half of the propagation time for a periodic axial orbit.

### Converged Axial Families

From the methods used to obtain the halo families, the  $L_1$  and  $L_2$  axial families can also be obtained, shown in Figure 3.12 and Figure 3.13 respectively. Similar to the halo orbits, two halves to the family can be obtained by bifurcating above or below the  $xy$ -plane, making these the  $L_1$  northeast and  $L_2$  northwest axial families. Their stability indices follow in Figure 3.14. Again, there is an  $L_3$  axial family, but it is not used in this investigation.

#### 3.2.6 Vertical Orbits

##### A Vertical Targeter

Vertical orbits benefit from double symmetry about both the  $xz$ - and  $xy$ -planes. This allows for targeting only a quarter of the orbit, with a perpendicular crossing of the  $xz$ -plane on one end of the arc and a perpendicular crossing of the  $x$ -axis on the other. Starting from the  $xz$ -plane crossing:

$$\bar{X} = \begin{bmatrix} x_0 & z_0 & \dot{y}_0 & \tau \end{bmatrix}^T, \quad (3.38)$$

$$\bar{F}(\bar{X}) = \begin{bmatrix} y_f & z_f & \dot{x}_f & C - C_d \end{bmatrix}^T = \bar{0}, \quad (3.39)$$

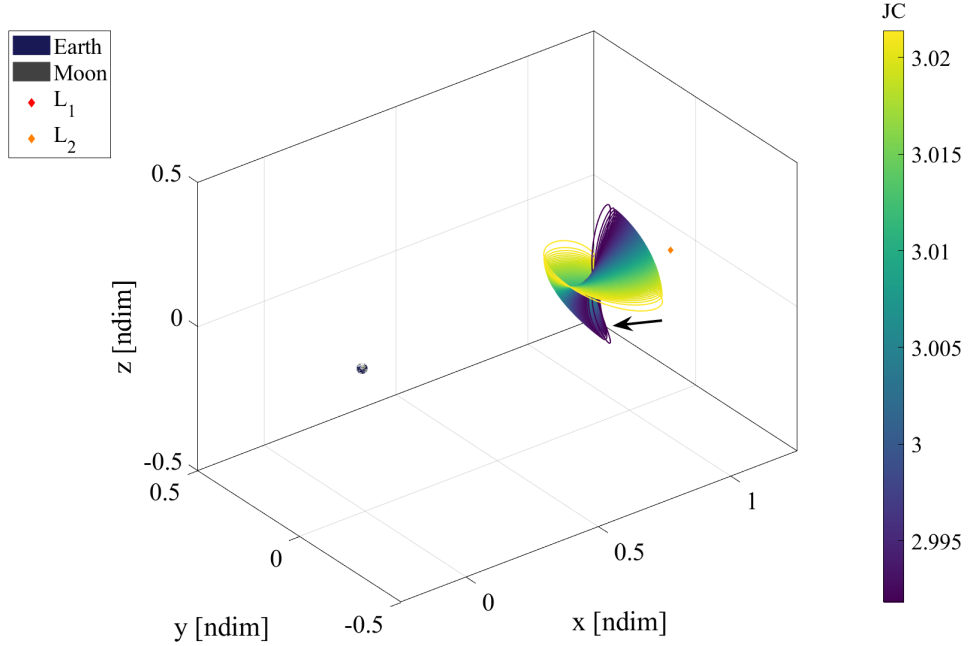


**Figure 3.12.** Earth-Moon  $L_1$  northeast axial orbit family.

$$DF(\bar{X}) = \begin{bmatrix} \phi_{21} & \phi_{23} & \phi_{25} & \dot{y}_f \\ \phi_{31} & \phi_{33} & \phi_{35} & \dot{z}_f \\ \phi_{41} & \phi_{43} & \phi_{45} & \ddot{x}_f \\ 2x_0 - \frac{2(x_0 + \mu)(1 - \mu)}{d^3} - \frac{2\mu(x_0 - 1 + \mu)}{r^3} & -\frac{2z_0(1 - \mu)}{d^3} - \frac{2z_0\mu}{r^3} & -2\dot{y}_0 & 0 \end{bmatrix}. \quad (3.40)$$

The result of this targeting will provide the initial state ( $y_0 = \dot{x}_0 = \dot{z}_0 = 0$ ) at the perpendicular crossing of the  $xz$ -plane (top/bottom of the orbit) and one-quarter of the propagation time for a periodic vertical orbit.

### Converged Vertical Families

The vertical orbit family bifurcates from the end of the axial family when the axial orbit intersects itself and resembles a figure-eight. Stepping in one direction shrinks the orbits as the family collapses down to its origin Lagrange point. The other direction expands the orbits until they look like clam shells, demonstrated for the  $L_1$  family in Figure 3.15. Similar

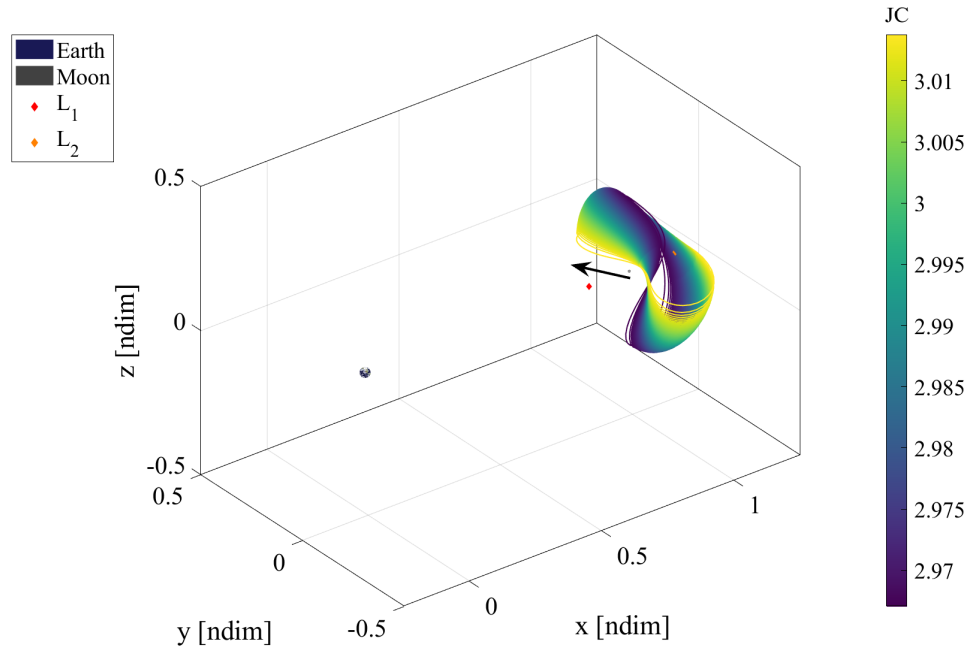


**Figure 3.13.** Earth-Moon  $L_2$  northwest axial orbit family.

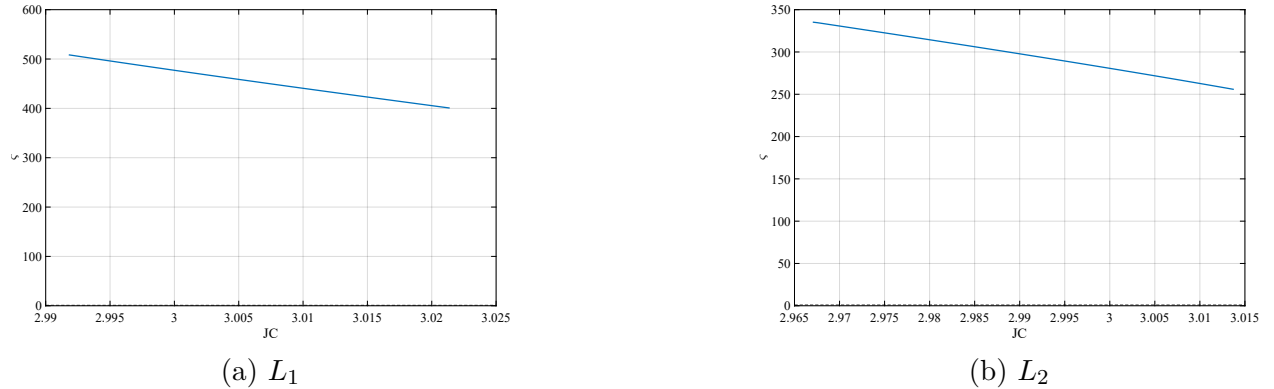


**Figure 3.14.** Earth-Moon axial family stability index evolution.

behavior occurs with the  $L_2$  vertical family in Figure 3.16. Figure 3.17 shows the stability indices for these two families;  $L_3$  verticals are not used in this investigation.

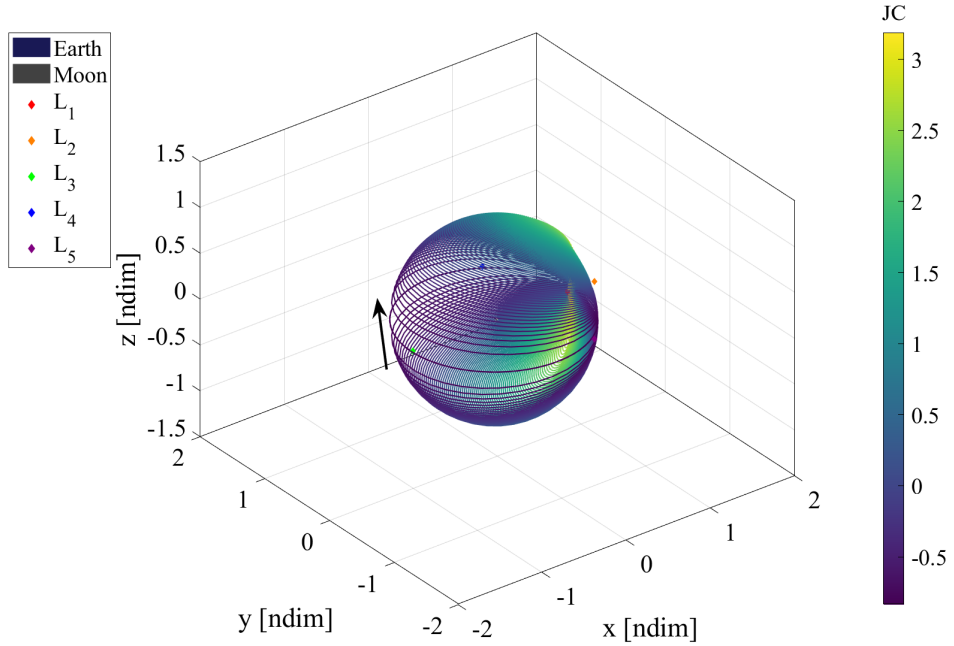


**Figure 3.15.** Earth-Moon  $L_1$  vertical orbit family.

### 3.2.7 Equilateral Long Period Orbits

#### A Planar Equilateral Orbit Targeter

Similar to the Lyapunov orbits around the colinear equilibrium points, there are planar orbits around the equilateral equilibrium points  $L_4$  and  $L_5$ ; however, they do not have symmetry that can be exploited. Therefore, the full period of the orbit needs to be targeted, constraining periodicity between the propagation start and end points. Note that since the Jacobi constant of a propagated trajectory is naturally constrained, constraining periodicity only requires constraining five out of the six states (three out of the four for a planar problem):

$$\bar{X} = \begin{bmatrix} x_0 & \dot{x}_0 & \dot{y}_0 & \tau \end{bmatrix}^T, \quad (3.41)$$

$$\bar{F}(\bar{X}) = \begin{bmatrix} x_f - x_0 & y_f - y_0 & \dot{x}_f - \dot{x}_0 & C - C_d \end{bmatrix}^T = \bar{0}, \quad (3.42)$$

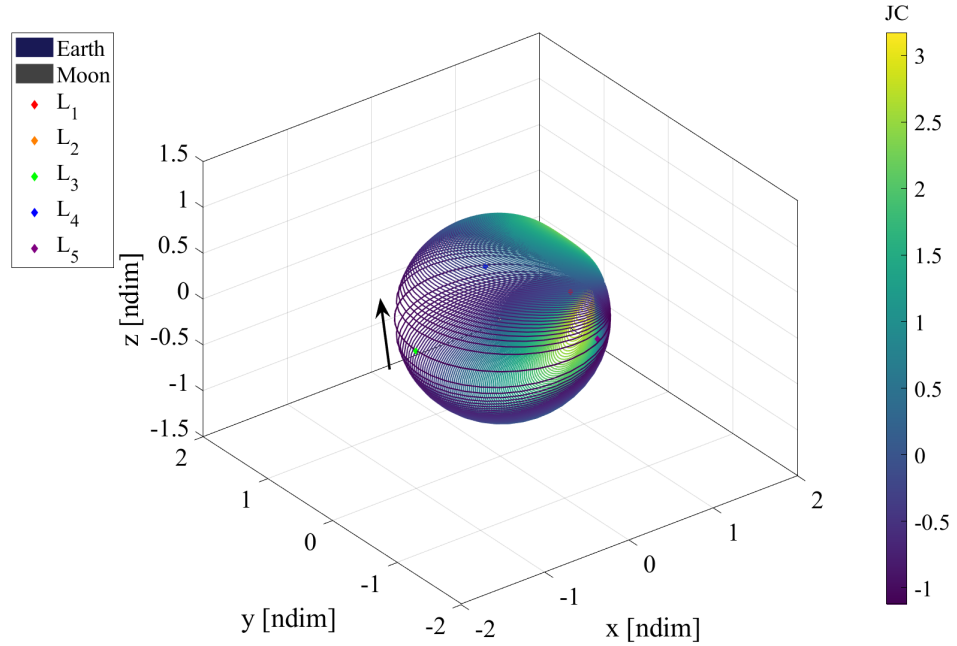


**Figure 3.16.** Earth-Moon  $L_2$  vertical orbit family.

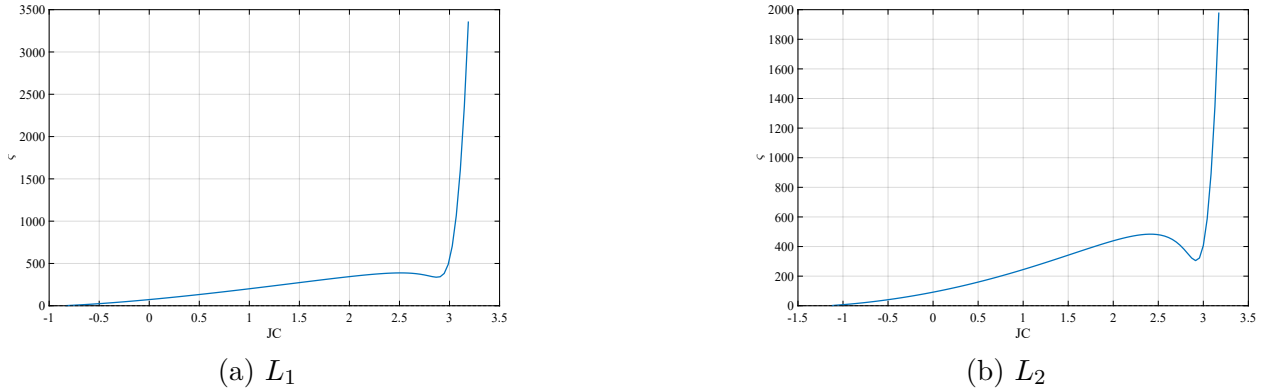


**Figure 3.17.** Earth-Moon vertical family stability index evolution.

$$DF(\bar{X}) = \begin{bmatrix} \phi_{11} - 1 & \phi_{14} & \phi_{15} & \dot{x}_f \\ \phi_{21} & \phi_{24} & \phi_{25} & \dot{y}_f \\ \phi_{41} & \phi_{44} - 1 & \phi_{45} & \ddot{x}_f \\ 2x_0 - \frac{2(x_0 + \mu)(1 - \mu)}{d^3} - \frac{2\mu(x_0 - 1 + \mu)}{r^3} & -2\dot{x}_0 & -2\dot{y}_0 & 0 \end{bmatrix}. \quad (3.43)$$

Since  $z = \dot{z} = 0$ , this targeter provides five of the six initial state variables and the full period for the planar equilateral orbit.

## Equilateral Long Period Orbit Initial Guess

Initial guesses for the planar equilateral orbits close to the Lagrange point can come from linear variational equations of motion about the equilibrium point:

$$x_0 = x_L + \xi, \quad (3.44)$$

$$y_0 = y_L + \eta, \quad (3.45)$$

$$\dot{x}_0 = \alpha s, \quad (3.46)$$

$$\dot{y}_0 = \beta s, \quad (3.47)$$

where  $\xi$  and  $\eta$  are chosen variations from the Lagrange point,

$$s = \text{Im}(\lambda), \quad (3.48)$$

$$\alpha = \frac{\xi \frac{\partial U}{\partial x \partial y} + \eta \left( \frac{\partial u}{\partial y \partial y} + s^2 \right)}{2s}, \quad (3.49)$$

$$\beta = -\frac{\xi \left( \frac{\partial U}{\partial x \partial x} + s^2 \right) + \eta \frac{\partial U}{\partial x \partial y}}{2s}. \quad (3.50)$$

The linearization has two frequencies, short and long, and the choice of frequency determines  $\lambda$ . The short period orbits are not used in this investigation, so for long period orbits:

$$\lambda = \sqrt{\frac{\sqrt{1 - 27\mu(1 - \mu)} - 1}{2}}. \quad (3.51)$$

For consistency,  $y_0$  is chosen to be the  $y$ -value of the Lagrange point  $y_L$  with  $\eta = 0$ . The initial guess for the period is also determined by the choice of frequency:

$$\tau = 2\pi s. \quad (3.52)$$

## Converged Equilateral Long Period Orbit Families

Since the CR3BP is symmetric about the  $xz$ -plane, all  $L_4$  orbit families can be mirrored across that plane to find the  $L_5$  families and vice versa. This is done by flipping the signs of  $y$ ,  $\dot{x}$ , and  $\dot{z}$ . Therefore, Figure 3.18 shows portions of both equilateral long period orbit families in the Earth-Moon system and Figure 3.19 shows their stability indices.

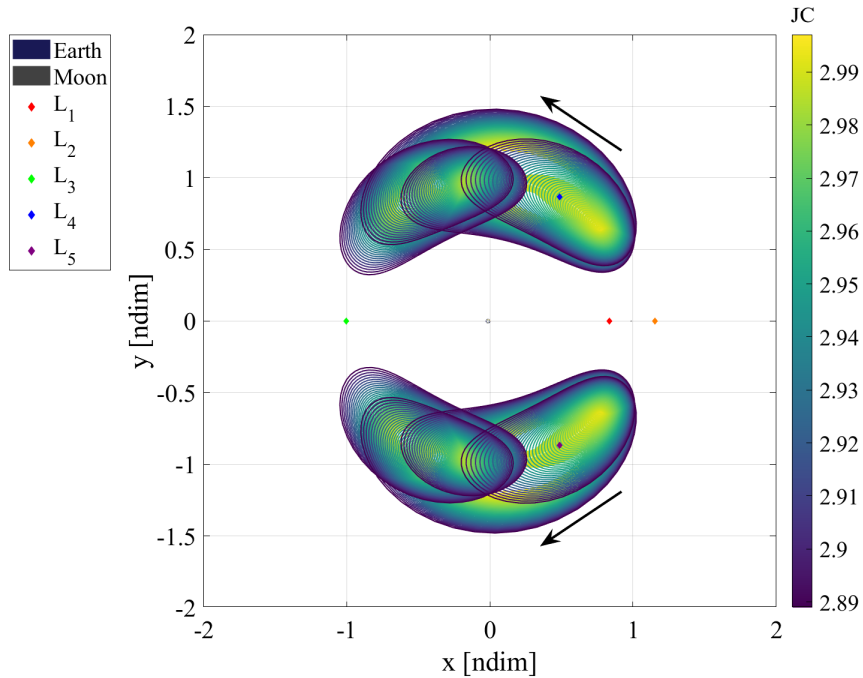


**Figure 3.18.** Earth-Moon  $L_4$  and  $L_5$  equilateral long period orbit families.

### 3.2.8 Equilateral Axial Orbits

#### A Spatial Equilateral Orbit Targeter

While axial orbits exist around  $L_4$  and  $L_5$ , unlike their colinear counterparts, these axial families bifurcate from the  $L_1$  halo family. Like the planar equilateral orbits, symmetry cannot be exploited to aid the targeting process, so periodicity must be targeted instead:

$$\bar{X} = \begin{bmatrix} x_0 & y_0 & \dot{x}_0 & \dot{y}_0 & \dot{z}_0\tau \end{bmatrix}^T, \quad (3.53)$$

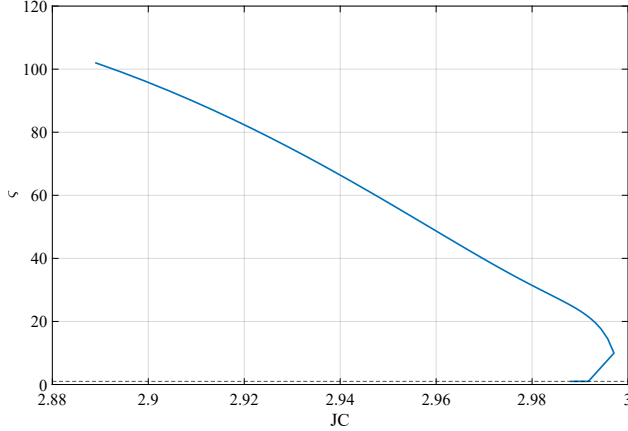


**Figure 3.19.** Earth-Moon equilateral long period orbit family stability index evolution.

$$\bar{F}(\bar{X}) = \begin{bmatrix} x_f - x_0 & y_f - y_0 & \dot{x}_f - \dot{x}_0 & \dot{y}_f - \dot{y}_0 & \dot{z}_f - \dot{z}_0 & C - C_d \end{bmatrix}^T = \bar{0}, \quad (3.54)$$

$$DF(\bar{X}) = \begin{bmatrix} \phi_{11} - 1 & \phi_{12} & \phi_{14} & \phi_{15} & \phi_{16} & \dot{x}_f \\ \phi_{21} & \phi_{22} - 1 & \phi_{24} & \phi_{25} & \phi_{26} & \dot{y}_f \\ \phi_{41} & \phi_{42} & \phi_{44} - 1 & \phi_{45} & \phi_{46} & \ddot{x}_f \\ \phi_{51} & \phi_{52} & \phi_{54} & \phi_{55} - 1 & \phi_{56} & \ddot{y}_f \\ \phi_{61} & \phi_{62} & \phi_{64} & \phi_{65} & \phi_{66} - 1 & \ddot{z}_f \\ 2x_0 - \frac{2(x_0 + \mu)(1 - \mu)}{d^3} - \frac{2\mu(x_0 - 1 + \mu)}{r^3} & 2y_0 - \frac{2y_0(1 - \mu)}{d^3} - \frac{2y_0\mu}{r^3} & -2\dot{x}_0 & -2\dot{y}_0 & -2\dot{z}_0 & 0 \end{bmatrix}. \quad (3.55)$$

### Converged Equilateral Axial Families

The pseudo-arc length method can be used to obtain the initial guess for the equilateral axial family. Stepping in one direction will produce the  $L_4$  family while stepping in the other produces the  $L_5$  family. These are both shown in Figure 3.20. Figure 3.21 shows the stability indices for these families. As hinted at by the end of these axial families,  $L_4$  and  $L_5$  vertical families also exist in the Earth-Moon system but are not used in this investigation.

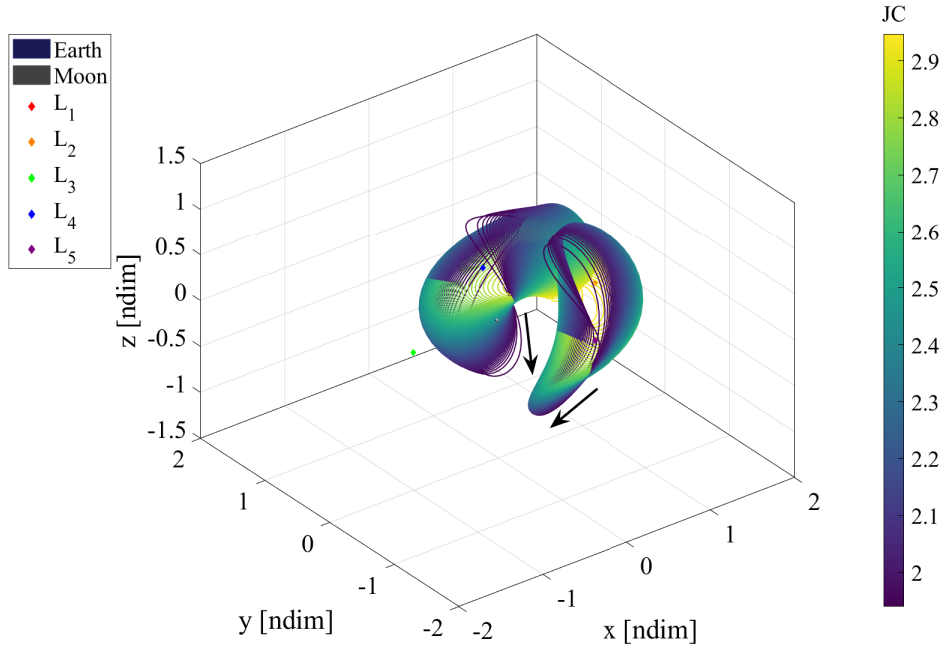


**Figure 3.20.** Earth-Moon  $L_4$  and  $L_5$  equilateral axial families.

### 3.2.9 Resonant Orbits

Many other types of CR3BP orbits are not associated with a Lagrange point. Some of these orbit families are known as resonant orbits because their periods are resonant or close to resonant with the Moon's' period. These orbits are still periodic in the rotating frame but are also periodic or close to periodic in an inertial frame. Individual orbits also tend to span more of the Earth-Moon system than the Lagrange point orbits. For more details on how to determine initial guesses and correct these orbits, Gupta[45] and Sadaka[46] provide extensive overviews and initial conditions. A couple of unstable resonant orbit families are used in this investigation and so they are shown here.

#### Converged 2:1a Resonant Orbit Family

The unstable section of the 2:1 resonant orbit family (denoted the 2:1a resonant orbit family by Sadaka) is shown in Figure 3.22[46]. These orbits travel around the Earth roughly twice for every time the Moon revolves around it, which becomes more evident when the

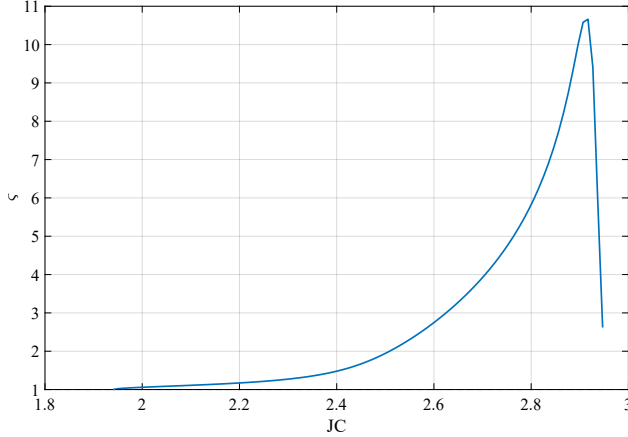


**Figure 3.21.** Earth-Moon equilateral axial family stability index evolution.

trajectories are viewed in an inertial frame. Figure 3.23 shows the stability index evolution for this family.

### Converged 3:4 Resonant Orbit Family

Another unstable family is the 3:4 resonant orbits, shown in Figure 3.24. These orbits go around the Earth three times for every time the Moon goes around. Their stability indices are given in Figure 3.25.

### 3.3 Invariant Manifolds

Dynamically unstable periodic orbits in the CR3BP have useful structures called invariant manifolds that represent a combination of the hyperbolic and oscillatory local flow near the orbit. With applications for transfer design, trajectories along these manifold surfaces asymptotically arrive at or depart from the periodic orbit ballistically. Perko provides the following theorem for stable/unstable manifolds for periodic orbits[47]:

Let  $f \in C^1(E)$  where  $E$  is an open subset of  $R^n$  containing a periodic orbit,

$$\Gamma : \bar{x} = \gamma(t), \quad (3.56)$$

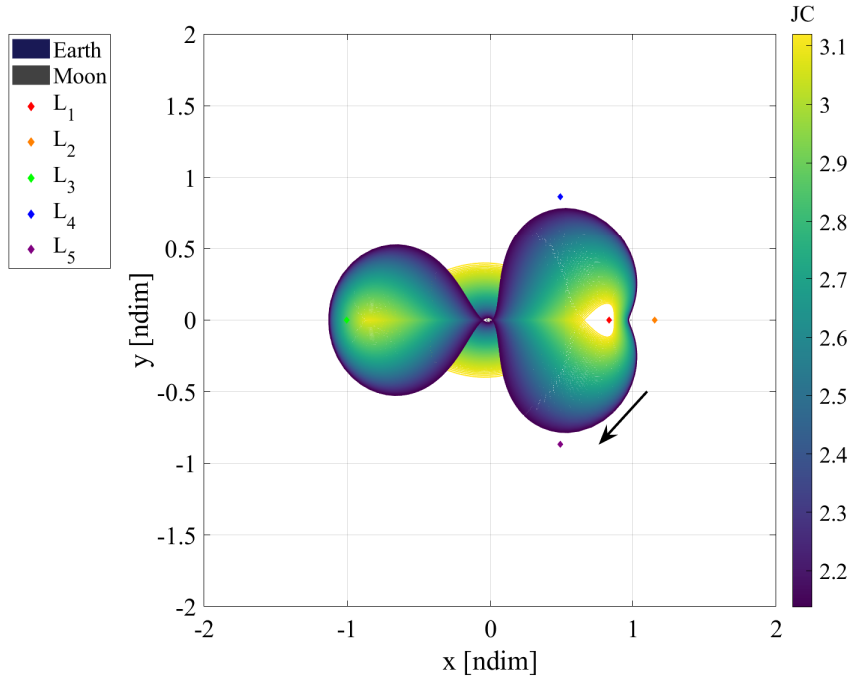


**Figure 3.22.** Earth-Moon 2:1a resonant orbit family.

of  $\dot{\bar{x}} = f(\bar{x})$  of period  $T$ . Let  $\phi_t$  be the flow of  $\dot{\bar{x}} = f(\bar{x})$  and  $\gamma(t) = \phi_t(\bar{x}_0)$ . If  $k$  of the characteristic exponents of  $\gamma(t)$  have negative real part where  $0 \leq k \leq n - 1$  and  $n - k - 1$  of them have positive real part then there is a  $\delta > 0$  such that the stable manifold of  $\Gamma$ ,

$$S(\Gamma) = \{\bar{x} \in N_\delta(\Gamma) | d(\phi_t(\bar{x}), \Gamma) \rightarrow 0 \text{ as } t \rightarrow \infty \text{ and } \phi_t(\bar{x}) \in N_\delta(\Gamma) \text{ for } t \geq 0\}, \quad (3.57)$$

is a  $(k + 1)$ -dimensional, differentiable manifold which is positively invariant under the flow  $\phi_t$  and the unstable manifold of  $\Gamma$ ,

$$U(\Gamma) = \{\bar{x} \in N_\delta(\Gamma) | d(\phi_t(\bar{x}), \Gamma) \rightarrow 0 \text{ as } t \rightarrow -\infty \text{ and } \phi_t(\bar{x}) \in N_\delta(\Gamma) \text{ for } t \leq 0\}, \quad (3.58)$$

is an  $(n - k)$ -dimensional, differentiable manifold which is negatively invariant under the flow  $\phi_t$ . Furthermore, the stable and unstable manifolds of  $\Gamma$  intersect transversally in  $\Gamma$ .

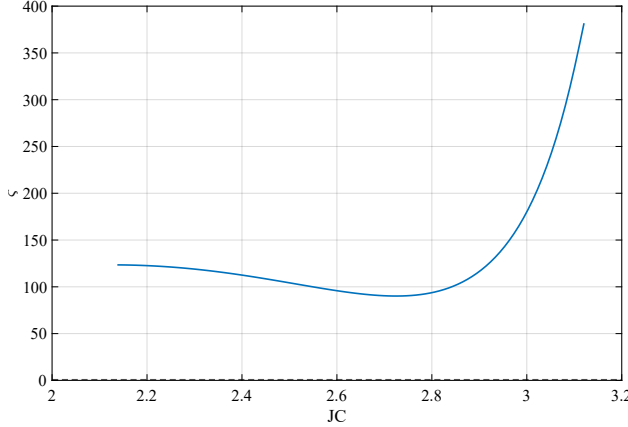


**Figure 3.23.** Earth-Moon 2:1a resonant orbit family stability index evolution.

In layman's terms, if a periodic orbit is unstable (has eigenvalues greater than and lesser than 1), then stable/unstable manifold surfaces exist that approach/leave the orbit asymptotically in forward time.

### 3.3.1 Approximating a Manifold Arc

Since these manifold structures asymptotically depart the orbit structure, no deterministic maneuver is required to transfer onto them. However, a consequence of this is that it is not possible to identify the exact location along the orbit from where a manifold trajectory departs. Therefore, a numerical process is necessary to approximate the stable/unstable subspace of the orbit to determine an appropriate initial condition for an arc along the manifold surface.

Near the periodic orbit, the manifolds are tangent to their corresponding eigenspaces of the orbit. For a selected point on the periodic orbit:

$$\bar{\nu}(t_0 + t) = \Phi(t_0 + t, t_0)\bar{\nu}(t_0), \quad (3.59)$$

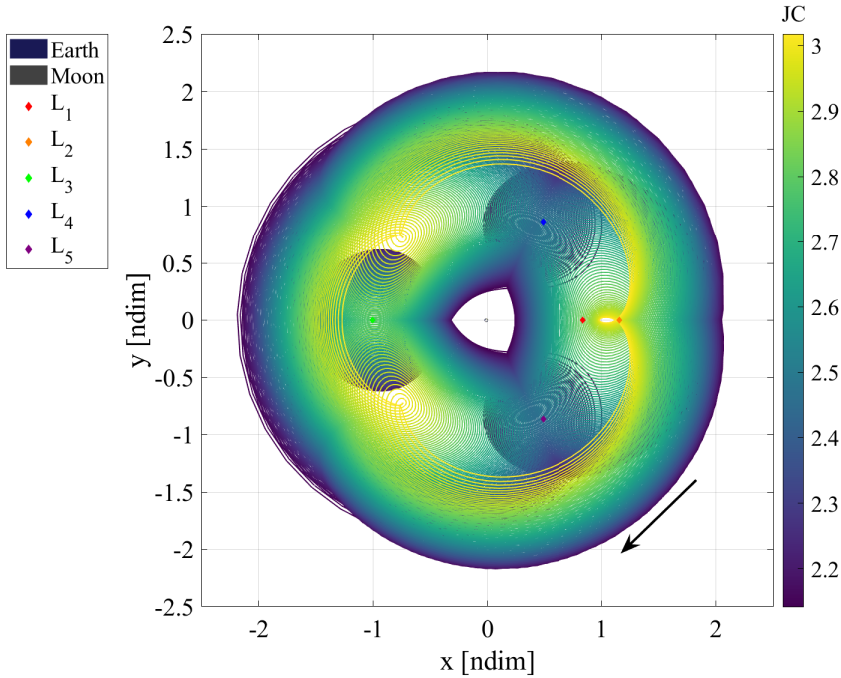


**Figure 3.24.** Earth-Moon 3:4 resonant orbit family.

where  $\bar{\nu}(t_0)$  is the eigenvector at the initial condition corresponding to the stable or unstable eigenvalue of the monodromy matrix. Once the stable/unstable eigenvector at the selected point has been obtained:

$$\bar{\nu}_n = \frac{\bar{\nu}}{\sqrt{\nu_x^2 + \nu_y^2 + \nu_z^2}}, \quad (3.60)$$

where  $\nu_x$  is the  $x$ -component of the eigenvector and  $\bar{\nu}_n$  is the eigenvector normalized by the nondimensional distance from the selected point. Using the normalized stable eigenvector to approximate the initial condition for a stable manifold arc:

$$\bar{q}^S = \bar{q}_\Gamma \pm d\bar{\nu}_n^S, \quad (3.61)$$

where  $\bar{q}_\Gamma$  is the state vector at the selected point along the periodic orbit and  $d$  is a step-off distance, generally chosen based on the specific CR3BP system. The scaled eigenvector can be either added to or subtracted from the periodic state as the eigenspace is bi-directional, creating two half-manifolds for each stability. To compute an initial condition for an unsta-

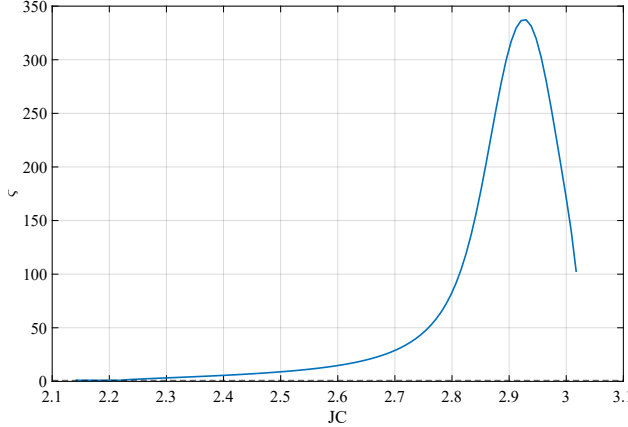


**Figure 3.25.** Earth-Moon 3:4 resonant orbit family stability index evolution.

ble manifold arc, use Equation (3.59)-Equation (3.61), replacing the stable components for unstable ones. Stable manifold arcs are then propagated backward in time from the initial condition (arriving at the orbit in forward time) while unstable arcs are propagated forward in time from their initial condition.

As mentioned, the value for  $d$  depends on the CR3BP system in use. This parameter needs to be sufficiently small to approximate the manifold structure well. However, if  $d$  is too small, the trajectory will take longer than reasonable to arrive at/depart from the orbit since the dynamics are asymptotic[34]. Table 3.1 shows the values of  $d$  used for the systems in this investigation. As some examples of manifold structures, Figure 3.26 and Figure 3.27 show the stable and unstable manifolds for a planar Lyapunov orbit and a spatial halo orbit, respectively, in the Earth-Moon system. Each figure also shows a single manifold arc overlayed on the full structure for reference. A more thorough explanation of manifold theory can be found in Perko[47].

**Table 3.1.** Manifold-related values of relevant CR3BP systems.

CR3BP System	$d$ [km]	$\Delta MI$ Threshold
Earth-Moon	25	$1 \times 10^{-3}$
Sun-Earth	1000	$5 \times 10^{-5}$
Sun-Mars	1000	$1 \times 10^{-5}$

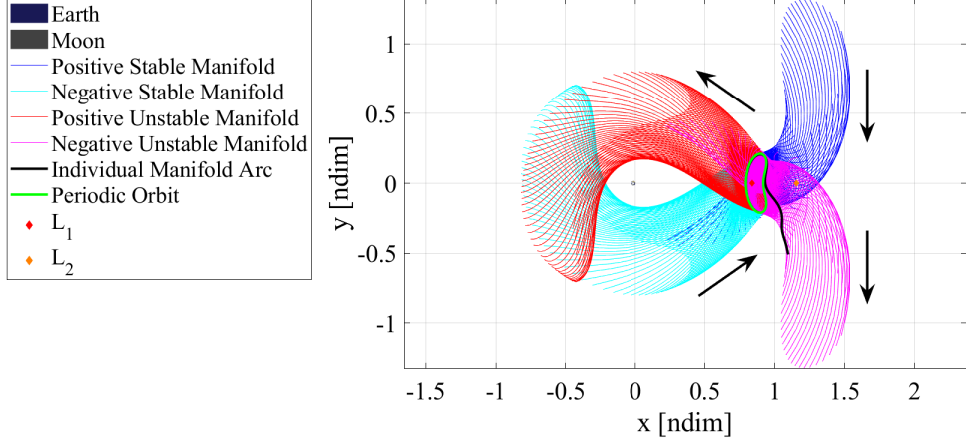


**Figure 3.26.** Earth-Moon  $L_1$  Lyapunov Manifolds ( $C = 3.05$ ).

### 3.3.2 Manifold Time-of-Flight

Since manifolds asymptotically arrive at/depart from their orbit, even with a reasonable step-off distance, they can take a long time to depart from the orbit vicinity. Under higher-fidelity dynamics, this period of time would be eliminated from the mission design, so it would be useful to have a metric to determine when the manifold has departed the orbit vicinity. In this investigation, the momentum integral, or more specifically the momentum integral difference, is used to indicate orbit departure:

$$MI = \int_{t_0}^t (x\dot{x} + y\dot{y} + z\dot{z}) d\tau, \quad (3.62)$$

where all of the values are nondimensional. Starting from  $MI_0 = 0$  at the step-off location, the momentum integral is calculated for both the orbit and the manifold arc and the difference between the two values measures the similarity of the two trajectories:

$$\Delta MI = |MI - MI_\Gamma|. \quad (3.63)$$

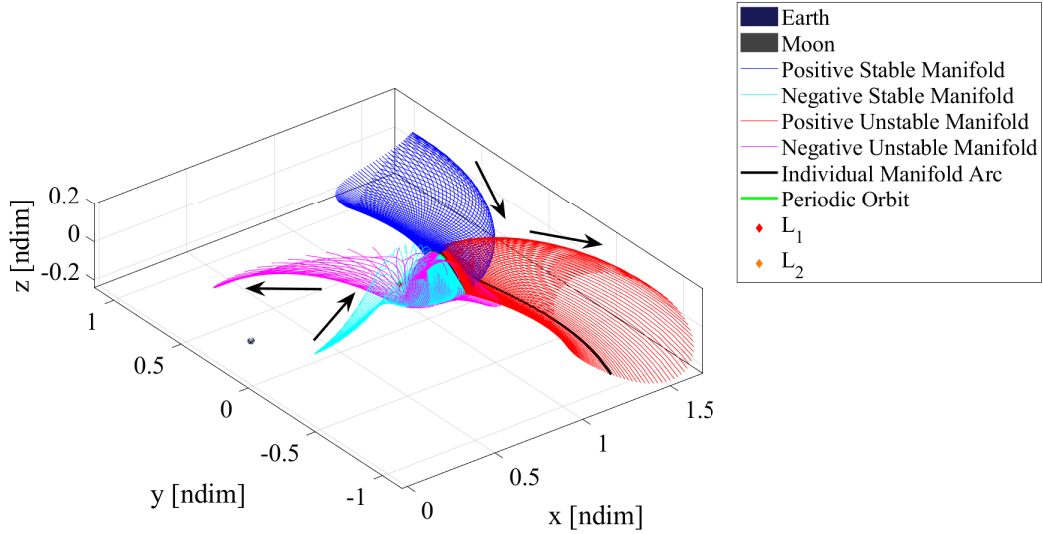


**Figure 3.27.** Earth-Moon  $L_2$  Halo Manifolds ( $C = 3.08$ ).

Once  $\Delta MI$  has reached a threshold value (determined for each system), the trajectory is considered departed from the orbit[48]. Thus, the time it takes for the manifold to depart can be subtracted from the time-of-flight along the manifold arc starting from the step-off. Table 3.1 shows the threshold values chosen for each system in this investigation.

### 3.4 Poincaré Maps

Since plots of invariant manifolds in configuration space can be complex and do not display any velocity information about the trajectories, a different visualization technique is advantageous. Poincaré maps are an approach that concisely visualizes trajectories by reducing the dimension of the problem through a hyperplane. These hyperplanes can be physical surfaces, like a plane or sphere in configuration space, or more abstract, like an apse or velocity map. As initial conditions are propagated, whenever a trajectory passes through the hyperplane, its crossing is marked on the Poincaré map. A simple example is shown in Figure 3.28.

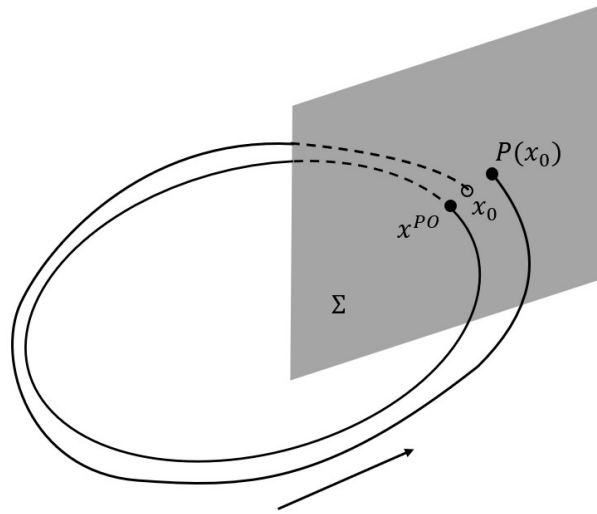


**Figure 3.28.** Poincaré map.

Starting from an initial condition  $x_0$  on the hyperplane  $\Sigma$ , after propagating the trajectory returns to the hyperplane at  $P(x_0)$ . If the trajectory is precisely periodic, the trajectory will return to the same point,  $x^{PO}$ . The Poincaré map then is the 2-dimensional representation of the hyperplane, displaying only the trajectory crossings. Note that the axes of the map need not be position components but could also be velocity, energy, etc. Similar mappings are used in this investigation to more efficiently analyze and compare manifold trajectories of different orbits.

## 4. CISLUNAR-MARS TRAJECTORY CONSTRUCTION

Many of the techniques introduced in the previous chapter are used in this investigation to design end-to-end transfers between orbits in the Earth-Moon and Sun-Mars CR3BP systems. Two categories of transfers are designed and compared: trajectories that include an intermediate Sun-Earth staging halo orbit and those that do not. For the transfers utilizing a staging orbit, a strategy is adapted from Kakoi to compute near-ballistic transfer solutions between Earth-Moon unstable orbits and Sun-Earth halos via invariant manifolds[34]. Both sets of transfers then use a variation of the moon-to-moon analytical transfer methodology developed by Canales to bridge the gap between the Sun-Earth trajectories (either Sun-Earth manifolds or Earth-Moon manifolds propagated under Sun-Earth dynamics) and the Sun-Mars manifolds[33]. Note that this transfer design process may not result in optimized interplanetary transfers, but instead provides families of low-energy solutions to facilitate the comparison between cislunar departure orbits. As a baseline comparison metric, a Keplerian Hohmann transfer with a built-in plane change is also introduced here to represent the current standard for non-coplanar direct Earth-Mars transfers.

### 4.1 Near-Ballistic Transfers between the Earth-Moon and Sun-Earth Systems

While both categories of trajectories travel through the Sun-Earth CR3BP region, only those with an intermediate staging orbit have a constrained path. For these trajectories, the Earth-Moon unstable manifold arc, propagated under the Sun-Earth CR3BP dynamics once it reaches the lunar sphere of influence, must intersect with a stable manifold arc from the Sun-Earth staging  $L_2$  halo orbit. An unstable manifold arc from this orbit is then used to depart the Sun-Earth system (compared to the more direct transfer type that uses the Earth-Moon manifold to depart the system). Kakoi developed a design methodology for maneuver-free transfers between orbits in the two systems, treating them as non-coplanar, where the required respective initial orientations of the three bodies (the Sun, Earth, and Moon) are represented by angles and the interface between the CR3BP systems occurs at the intersection of the manifolds[21], [34]. This methodology inspired the approach used in

this investigation, where the orientations are determined by a specified epoch date and the two systems interface before the arc intersection.

#### 4.1.1 Methodology

To find a connection between the orbits in the two different CR3BP systems, discretized arcs of the manifold surface of the Earth-Moon departure orbit are propagated to the SoI of the Moon, as defined in Equation (2.46). At this distance from the Moon, its gravitational influence becomes negligible compared to those of the Earth and the Sun. At this interface of the two CR3BP systems, the Earth-Moon barycentric rotating frame state of each arc is transformed to a Sun-Earth barycentric rotating frame state by rotation to the Earth-centered Ecliptic J2000 inertial frame and back as described in Section 2.5.2. This rotation depends on the epoch date when the state reaches the SoI, as this determines the relative orientations of the celestial bodies. While the orientations change slightly month-to-month due to the different planes, the transfer characteristics tend to repeat each month, so this study only investigates transfers during January 2026[41].

Note that although these states all had the same Earth-Moon Jacobi constant value, now that they are in the Sun-Earth system, their Jacobi constant values will vary. Since these new values will remain constant as the states are now propagated with the Sun-Earth CR3BP equations of motion, it is necessary that the Jacobi constant of the Sun-Earth staging halo lies within that range of values. The manifold arcs are now propagated until they reach the manifold intersect hyperplane, chosen as an angle measured from the  $x$ -axis in the Sun-Earth rotating frame. According to Kakoi, hyperplane angles between  $-85^\circ$  and  $70^\circ$  are desirable for transfers between Earth-Moon  $L_2$  and Sun-Earth  $L_2$  orbits, with  $-80^\circ$  being used in this investigation[34]. At the same time, the discretized stable manifold surface from the Sun-Earth  $L_2$  halo orbit is propagated to the same hyperplane, as shown in Figure 4.1.

At the hyperplane, mappings of both manifolds are used to form phase plots that inform the transfer initial guess selection. Following Kakoi's approach, the plots represent  $\dot{x}$  vs.  $x$ ,  $z$  vs.  $x$ , and  $\dot{z}$  vs.  $z$ . The  $y$ -value is defined by the  $x$ -value and the hyperplane angle, while the  $\dot{y}$ -value is determined by the Jacobi constant[34]. A black dot along the Earth-

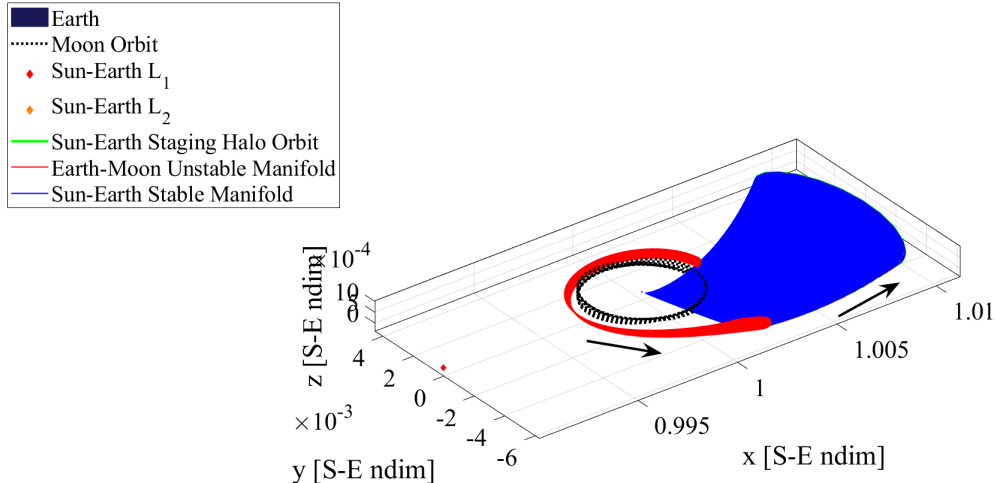


**Figure 4.1.** Earth-Moon and Sun-Earth manifolds intersecting at the hyperplane in the Sun-Earth rotating frame.

Moon manifold curve is also used to denote the arc that matches the Sun-Earth manifold in Jacobi constant. The two sets of manifold arcs form curves on the plots and the goal is to find an intersection between the curves in all three phase plots that occurs at the black point. Figure 4.2 shows an example of these phase plots, where the red curve is the unstable Earth-Moon manifold and the blue curve is the stable Sun-Earth manifold. Note that there are two black markers representing two arcs that match the Sun-Earth Jacobi constant.

The initial epoch of the Earth-Moon manifold departure, the hyperplane angle, and the Sun-Earth halo Jacobi constant can all be varied to shift the curves on the phase plots and find an intersection; Kakoi provides some guidelines on how to do so[34]. Once a suitable point is determined, like the black circle marker in Figure 4.3, this information can be used to generate an initial guess for the transfer between the systems, which is shown in Figure 4.4.

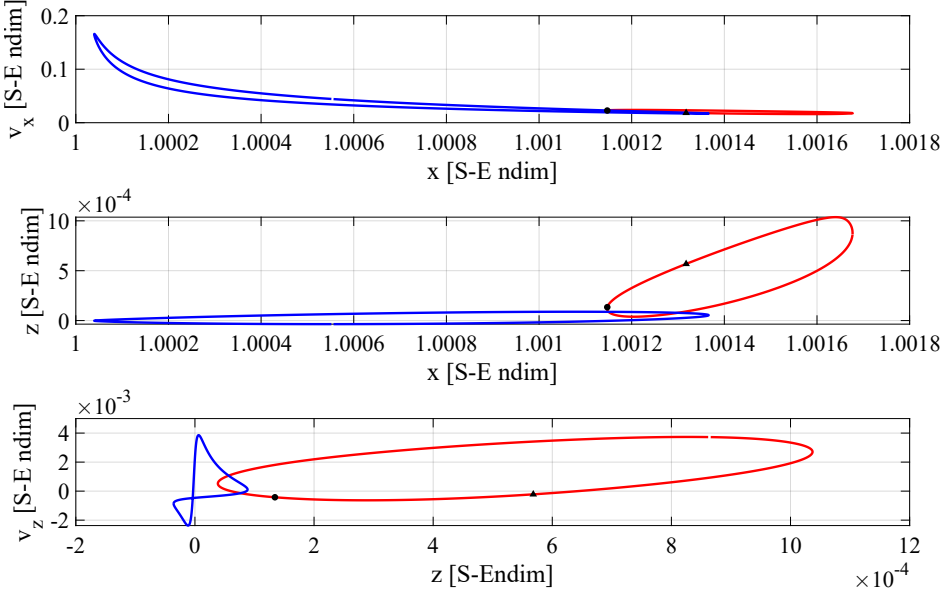


**Figure 4.2.** The hyperplane phase plots for Figure 4.1.

This initial guess is then corrected to find a position intersection (a maneuver is allowed at the intersection) using an iterative Newton-Raphson scheme:

$$\bar{X} = \begin{bmatrix} T_0 & \tau_1 & t_1 & \tau_2 & t_2 \end{bmatrix}^T, \quad (4.1)$$

$$\bar{F}(\bar{X}) = \begin{bmatrix} \bar{r}_2 - \bar{r}_1 & \|\bar{v}_2 - \bar{v}_1\| \end{bmatrix}^T. \quad (4.2)$$

where  $T_0$  is the initial epoch,  $\tau_1$  and  $\tau_2$  are the phase along the Earth-Moon and Sun-Earth orbits, respectively, where the manifold steps-off,  $t_1$  and  $t_2$  are the times-of-flight along each manifold arc, respectively,  $\bar{r}_1$  and  $\bar{r}_2$  are the manifold arc positions at the end of the propagation, and  $\bar{v}_1$  and  $\bar{v}_2$  are the velocity vectors at those points. The central difference method from Section 3.1.3 is used to determine the  $DF$  Jacobian matrix. Note that the magnitude of the maneuver is included as the second constraint in the targeting problem. For the first implementation of the targeter, the  $\Delta v$  of the initial guess is used as the constraint. Then, each time a solution is converged, this constraint value is decreased and the targeting problem is repeated to find a near-ballistic solution with a local minimum in  $\Delta v$ . Also note that during this process, the intersection location of the two manifold arcs

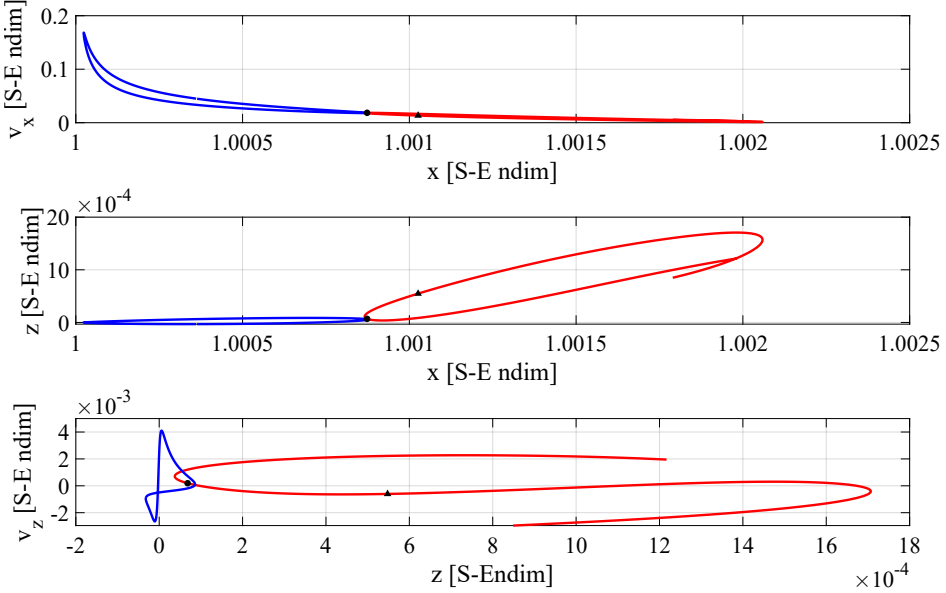


**Figure 4.3.** Hyperplane phase plots with a near intersection after varying the parameters.

is free to shift from the designated hyperplane. The result of this process is a near-ballistic transfer between an Earth-Moon orbit and a Sun-Earth halo orbit utilizing their invariant manifolds. These transfers have low enough maneuver costs that will likely be rendered negligible once the solution is transferred to a higher-fidelity dynamical model.

#### 4.1.2 Example

As an example, consider the phase plots in Figure 4.3 and the resulting initial guess in Figure 4.4. The unstable manifold arc departs from an Earth-Moon northern halo orbit with an Earth-Moon Jacobi constant of 3.13 on January 2, 2026 at 07:12:00, while the stable manifold arc arrives at a Sun-Earth northern halo orbit with a Sun-Earth Jacobi constant of 3.0008189. At the hyperplane intersection, these two arcs have a position discontinuity of  $8.768 \times 10^{-6}$  Sun-Earth nondimensional units (1312 km) and a  $\Delta v$  of 57.4 m/s. The iterative corrections process outlined above produces a position continuous trajectory with a  $\Delta v$  of 14.6 m/s, a negligible amount in comparison to the rest of the end-to-end transfer. The initial departure epoch has also shifted slightly, to January 2, 2026 at 07:32:35. This corrected trajectory is shown in Figure 4.5. Note that the location of the maneuver has shifted

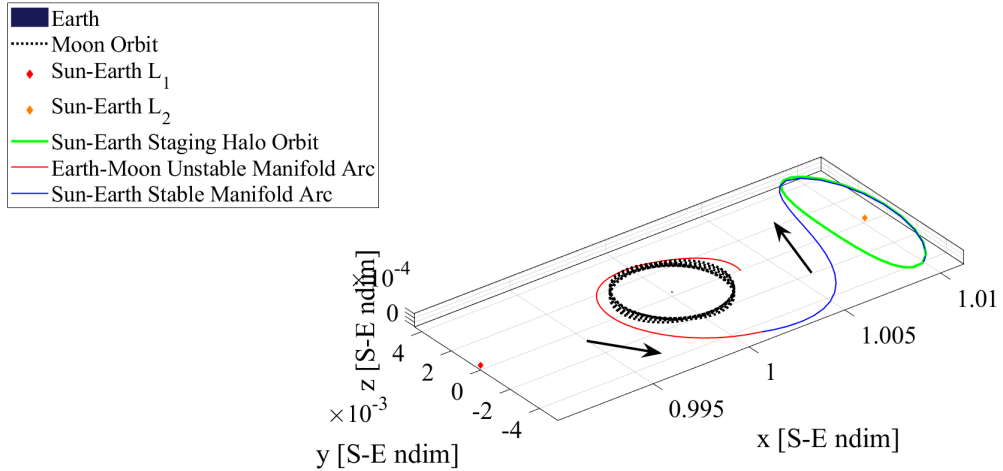


**Figure 4.4.** Initial guess for near-ballistic Earth-Moon to Sun-Earth transfer using phase plots in the Sun-Earth rotating frame.

from the defined hyperplane to earlier along the Earth-Moon manifold arc. While this exact solution is only available for the given epoch, every month a similar solution presents itself, so this one can be used to represent the potential near-ballistic transfer solutions.

## 4.2 The Moon-to-Moon Analytical Transfer Method

The MMAT method was created to design tours between the moons of a planet such as Jupiter or Saturn. However, Canales also showed that it could similarly be used for interplanetary transfers by treating the planets as "moons" of the Sun. He provides detailed derivations, analyses, and examples of the basic MMAT strategy, as well as some extensions relevant to this investigation[24], [25], [33]. More specifically, the end-to-end cislunar-Mars transfer methodology presented here uses a distant, two-burn MMAT with a plane change. This accounts for bridging the gap between manifolds of Sun-planet CR3BP systems and the true orbital plane inclinations of the planets.

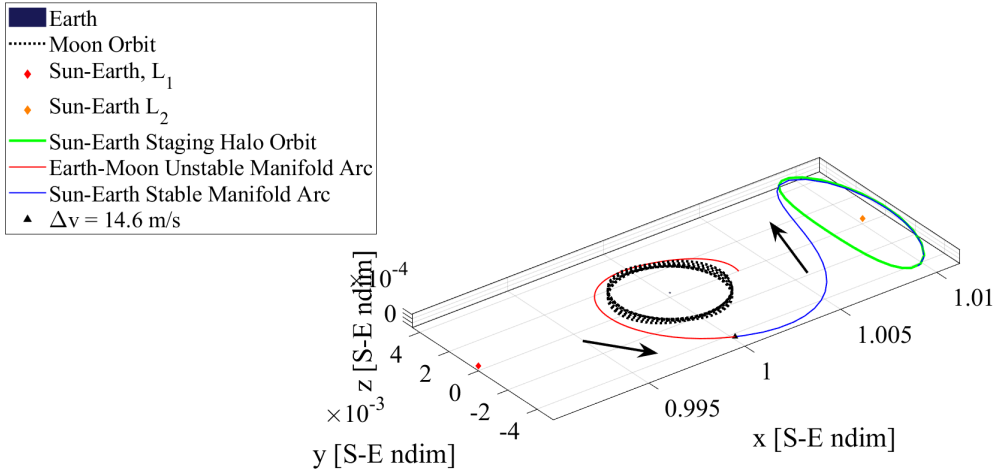


**Figure 4.5.** Converged near-ballistic tranfer between Earth-Moon and Sun-Earth halo orbits in the Sun-Earth rotating frame.

#### 4.2.1 Methodology

First, a departure and an arrival CR3BP arc are needed. In this investigation, the departure CR3BP arc is either a Sun-Earth halo orbit unstable manifold trajectory or an Earth-Moon orbit unstable manifold arc propagated with the Sun-Earth dynamics, depending on the transfer category. Either the departure epoch or the chosen manifold arc are varied to determine the departure CR3BP arc respectively. The arrival CR3BP arc is a Sun-Mars halo orbit stable manifold trajectory. Since an interplanetary transfer from Earth to Mars is an outward journey, to minimize the  $\Delta v$  of the MMAT transfer, the Sun-Mars stable manifold with the smallest periapsis (relative to the Sun) is used[33]. (For an inward journey, say to Venus, the manifold with the largest apoapsis is chosen.) This minimizes the Keplerian angular momentum and energy difference between the departure and arrival CR3BP arcs.

These arcs are propagated under the CR3BP dynamics until they reach a specified distance from their smaller primary (Earth or Mars), their sphere of influence. Various defini-

tions exist, but for the MMAT method, the SoI radius is defined as the distance for which the ratio of the gravitational accelerations of the two primaries  $d_{SoI}$  is equal to a chosen small quantity (see Equation (2.45))[33]. To ensure that the SoI encompasses most of the Lyapunov family but also accurately represents when that body's gravitational effects can be neglected, the values of  $d_{SoI}$  in Table 4.1 are chosen, resulting in their corresponding radii. Canales provides more details on selecting of appropriate values for  $d_{SoI}$ [33].

**Table 4.1.** MMAT sphere of influence radii of relevant CR3BP systems.

CR3BP System	$d_{SoI}$	$r_{SoI}$
Sun-Earth	$2.5 \times 10^{-4}$	0.09877
Sun-Mars	$1 \times 10^{-4}$	0.05375

Once the CR3BP arc has reached the edge of the SoI, it can be treated as a 2BP trajectory with the Sun as its focus (refer to the patched 2BP-CR3BP model introduced in Section 2.4.1). The barycentric rotating frame state that intersects the SoI is transformed to a heliocentric Ecliptic J2000 inertial frame state using the procedure outlined in Section 2.5.2. The resulting inertial state now defines a Keplerian heliocentric ellipse in the instantaneous plane of motion of the trajectory at the SoI, the path for either the departure or arrival conic arc. Equation (2.13)-Equation (2.21) can be used to retrieve the equivalent Keplerian orbital elements.

In the distant, two-burn MMAT strategy, the first maneuver is placed at the periapsis of the departure conic. Given that the true anomaly  $\theta = 0$  at periapsis, Equation (2.22)-Equation (2.28) are used to compute the inertial state at periapsis while Equation (2.29) and Equation (2.30) are used to compute the time-of-flight along the departure conic:

$$TOF_d = \mathbb{P}_d - (t - t_p), \quad (4.3)$$

where  $\mathbb{P}_d$  is the period of the departure conic and  $(t - t_p)$  is the time since periapsis of the inertial SoI state.

As mentioned previously, a bridge arc is needed to connect the departure and arrival conic arcs, with a maneuver at both ends. The distant, two-burn MMAT bridge arc has the

same periapsis radius as the departure conic arc and the same apoapsis as the arrival conic arc. These values form a bridge ratio which can then be used to compute the semimajor axis and eccentricity of the bridge conic:

$$\mathcal{P}_b = \frac{r_{p_b}}{r_{a_b}} = \frac{1 - e_b}{1 + e_b}, \quad (4.4)$$

$$e_b = \frac{1 - \mathcal{P}_b}{1 + \mathcal{P}_b}, \quad (4.5)$$

$$a_b = \frac{r_{p_b}}{1 - e_b}. \quad (4.6)$$

The remaining three angles of the bridge conic ( $i$ ,  $\Omega$ ,  $\omega$ ) are identical to those of the departure conic, implying that the bridge arc lies in the same plane as the departure conic arc. Since only the semimajor axis and eccentricity change between the departure and bridge conics, this first maneuver is tangential to the motion (only changing the energy) at periapsis and can be calculated by the difference in the velocity states at periapsis.

The non-coplanar MMAT methodology revolves around the following analytical constraint derived by Canales[33]:

As long as the geometrical properties of two conics located in different planes fulfill the inequality constraint represented by

$$a_a(1 - e_a) \leq \frac{a_b(1 - e_b^2)}{1 + e_b \cos(\theta_{b_{int}} + n\pi)} \leq a_a(1 + e_a), \text{ being } n = 0, 1, \quad (4.7)$$

either one of the two conics can be reoriented such that they intersect in space. Consequently, the ideal phase of the arrival [planet] at arrival,  $\theta_{5_{Mars}}$ , for the moon-to-moon transfer to occur is obtained considering that the departure epoch,  $\theta_{0_{Earth}}$ , is fixed.

In this constraint,  $\theta_{5_{Mars}}$  and  $\theta_{0_{Earth}}$  correspond to  $T_0$  and  $T_5$  in Figure 4.6. This figure is a schematic of the distant, two-burn MMAT transfer with a plane change, where the departure and bridge conics are on the same plane but the arrival conic is not. With the semimajor axes and eccentricities of the bridge and arrival arcs already determined, the only value still

needed for Equation (4.7) is  $\theta_{b_{int}}$ , the bridge conic true anomaly at the bridge-arrival conic intersection location ( $T_3$  in Figure 4.6):

$$\theta_{b_{int}} = u_b - \omega_b, \quad (4.8)$$

$$\sin u_b = \frac{\sin(\pi - i_a) \sin \Delta\Omega}{\sin \psi}, \quad (4.9)$$

$$\cos u_b = \frac{\frac{\sin i_a \cos \Delta\Omega}{\cos i_b} - \cos \psi \tan i_b}{\sin \psi}, \quad (4.10)$$

$$\cos \psi = \cos i_a \cos i_b + \sin i_a \sin i_b \cos \Delta\Omega, \quad (4.11)$$

where  $\Delta\Omega = \Omega_a - \Omega_b$ . Note that the value of  $n$  used to satisfy the inequality defines the orientation of the bridging conic and will be used later to properly orient the arrival conic. The center of the inequality in Equation (4.7) is the intersection distance from the Sun:

$$r_{int} = \frac{a_b(1 - e_b^2)}{1 + e_b \cos(\theta_{b_{int}} + n\pi)} = \frac{a_a(1 - e_a^2)}{1 + e_a \cos(\theta_{a_{int}} + o\pi)}, \text{ being } o = 0, 1, \quad (4.12)$$

Unfortunately, if the arrival conic arc is not in the same plane as the orbital plane of the arrival planet,  $i_a$  and  $\Omega_a$  cannot be determined prior to the MMAT phasing (yet to come). As a result, the arrival phasing needs to be iteratively targeted, making this approach now only semi-analytical. For an initial guess to check the MMAT constraint in Equation (4.7), the inclination and RAAN of the arrival planet's orbital plane are used.

The arrival conic true anomaly at the intersection is computed similarly from  $r_{int}$ , with the caveat that it is dependent on the arrival phasing and needs to be targeted:

$$\theta_{a_{int}} = 2\pi o + (-1)^o \arccos\left(\frac{\frac{a_a(1-e_a^2)}{r_{int}} - 1}{e_a}\right), \text{ being } o = 0, 1. \quad (4.13)$$

For every feasible  $\theta_{b_{int}}$ , there are then two possible phasing solutions ( $\theta_{a_{int}}$ ) that correspond to the two arrival ellipse orientations ( $\omega_a$ ) that intersect the bridge ellipse at the line of nodes. A schematic representing these two orientations is shown in Figure 4.7, where the

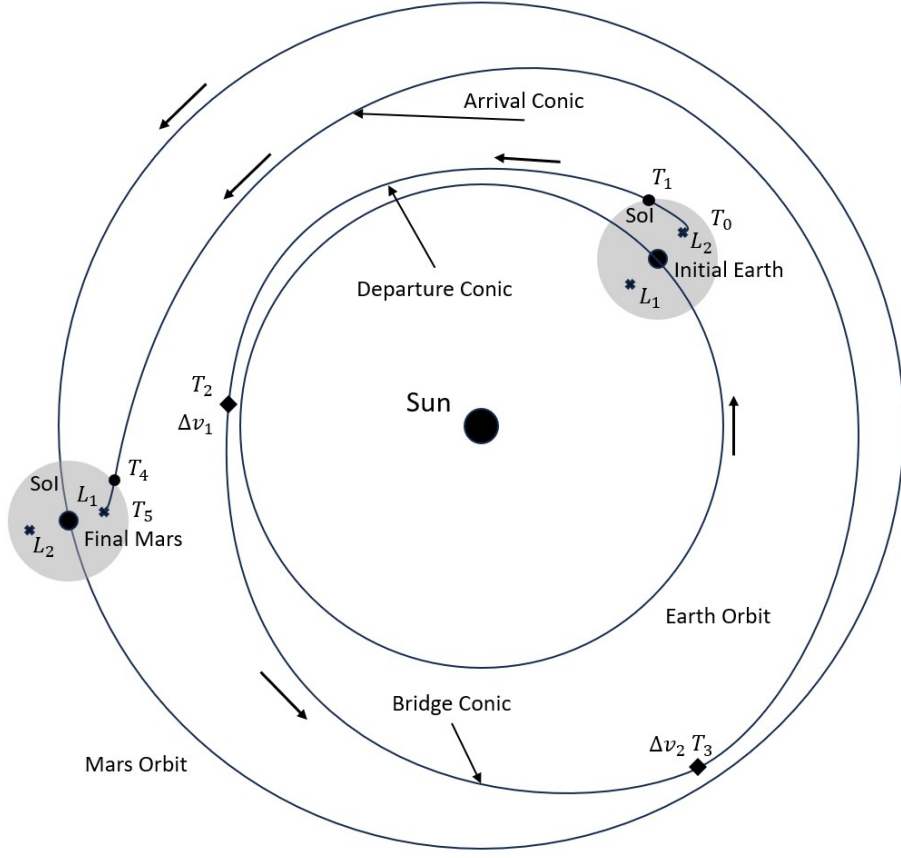


**Figure 4.6.** Representation of the distant, two-burn MMAT with a plane change (adapted from Canales[33]).

dashed part of the ellipses are under the  $XY$ -plane and the arrows show the direction of motion along each ellipse. The angles for the orientation are calculated similarly to before:

$$\omega_a = u_a - (\theta_{a_{int}} + n\pi), \quad (4.14)$$

$$\sin u_a = \frac{\sin i_b \sin \Delta\Omega}{\sin \psi}, \quad (4.15)$$

$$\cos u_a = \cos \Delta\Omega \cos u_b + \sin \Delta\Omega \sin u_b \cos i_b. \quad (4.16)$$

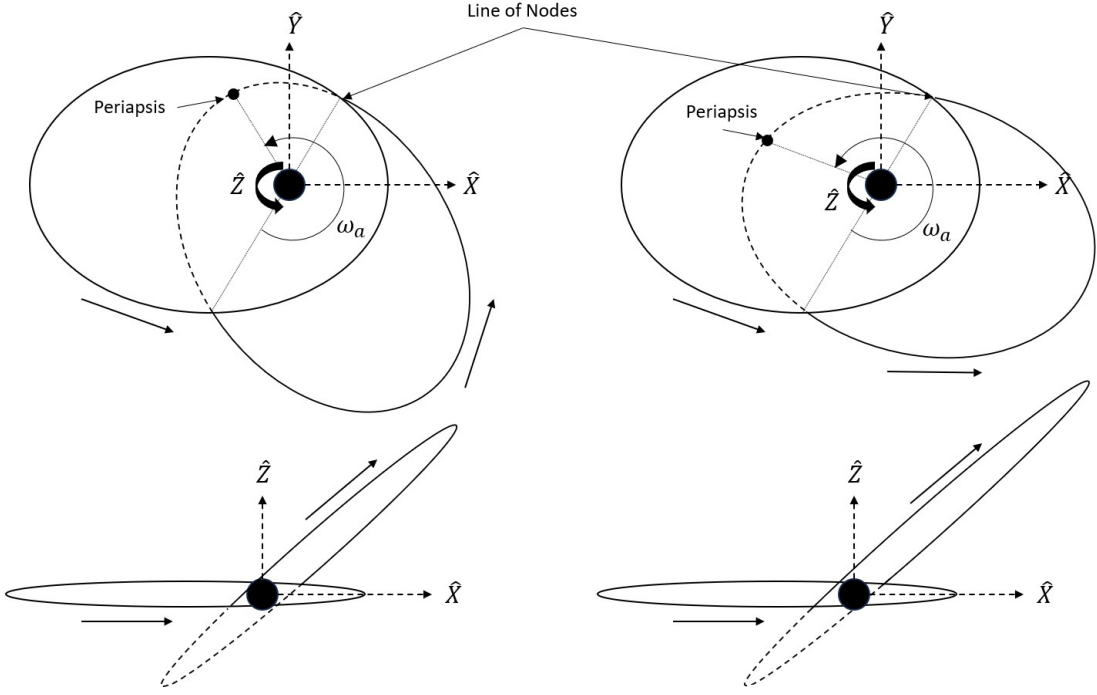


**Figure 4.7.** Representation of the two feasible arrival ellipse orientations. The top images are  $XY$ -plane views while the bottom are  $XZ$ -plane views.

Equation (4.14) is dependent on the orientation of the arrival CR3BP arc, which in turn depends on a properly phased arrival. Therefore, to solve for the proper phasing and orientation, an iterative Newton-Raphson differential corrections scheme is applied:

$$\bar{X} = \begin{bmatrix} \theta_{b_{int}} & \theta_{4_{Mars}} & \theta_{a_{int}} \end{bmatrix}^T, \quad (4.17)$$

$$\bar{F}(\bar{X}) = \bar{r}_a - \bar{r}_b, \quad (4.18)$$

where  $\theta_{4_{Mars}}$  corresponds to Mars' true anomaly when the trajectory intersects the Mars SoI. For an initial guess:

$$\theta_{4_{Mars}} = \arctan(\cos i_{Mars} \tan \Omega_{Mars}) + \omega_a + \theta_a - (\Omega_{Mars} + \omega_{Mars} + \theta_{Mars,J2000}) - \arctan\left(\frac{y_4}{|x_4|}\right), \quad (4.19)$$

where  $\theta_a$  is the true anomaly of the arrival conic at the SoI intersection,  $\theta_{Mars,J2000}$  is Mars' true anomaly when the J2000 inertial frame is defined, and  $x_4$  and  $y_4$  are the rotating frame

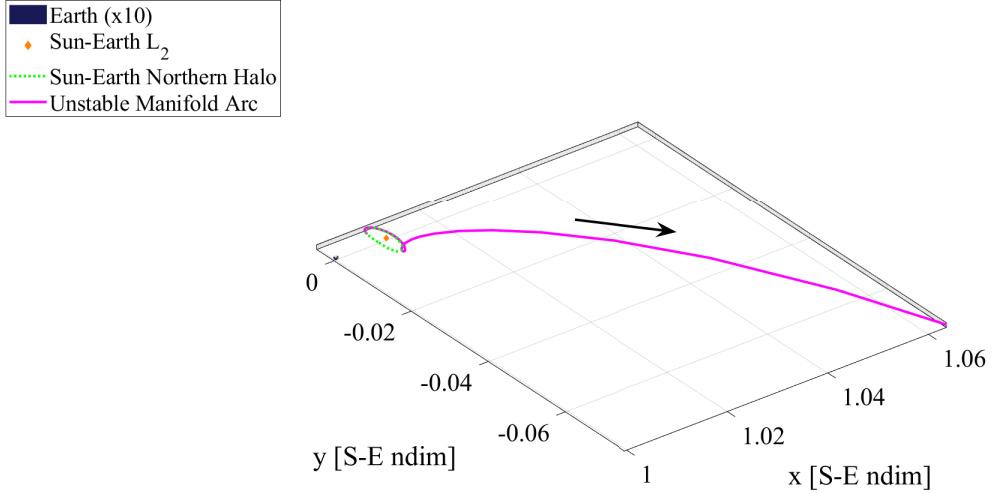
coordinates of the trajectory at the SoI intersection. For this targeting problem, the  $DF$  Jacobian matrix is determined using the central difference method (see Section 3.1.3).

Once  $\bar{X}$  has been solved, these true anomaly angles can be used to compute the Cartesian inertial states at each location and the times-of-flight of each segment as was done for the departure conic arc. At the intersection of the bridge and arrival conics, the second maneuver applies an inclination change on top of the energy change so it is not tangential like the first burn. This  $\Delta v$  can still be calculated from the difference in the velocity states at the intersection.

The MMAT transfer between the Sun-Earth CR3BP arc and the Sun-Mars CR3BP arc is now completed. The trajectory should be position-continuous throughout, with a maneuver at the beginning and end of the bridge arc to account for the velocity discontinuities. For every feasible  $\theta_{b_{int}}$ , there will be two corresponding  $\theta_{a_{int}}$  that provide transfers. These two solutions will have different maneuver costs and times-of-flight. By continuing in the departure epoch or the chosen manifold arc as discussed, a family of MMAT solutions can be obtained and compared.

#### 4.2.2 Example

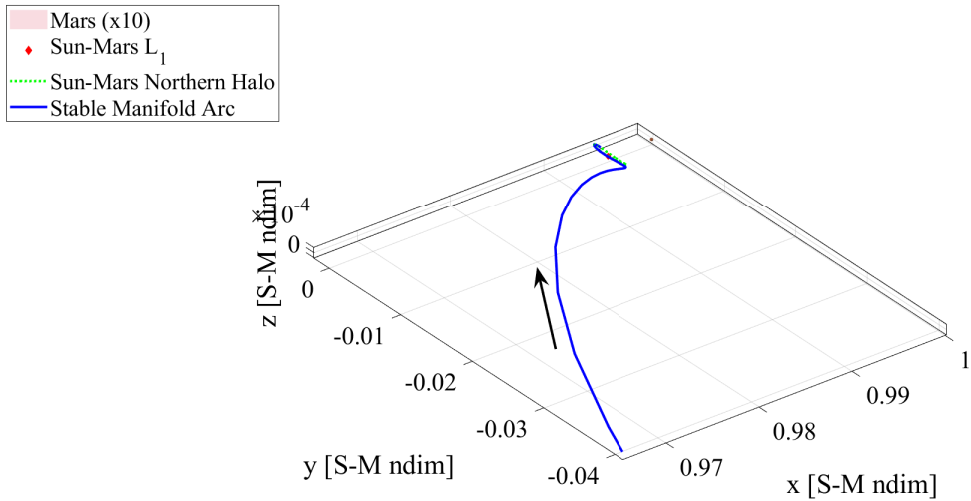
What follows is an example MMAT family between a Sun-Earth CR3BP northern halo orbit at a Jacobi constant of 3.0008189 and a Sun-Mars CR3BP northern halo orbit at a Jacobi constant of 3.0001857. Each transfer in the family starts at a different initial epoch, each day in an Earth year. These initial epochs correspond to  $\theta_{0_{Earth}}$  values (which spans  $0^\circ$ - $360^\circ$  in a year). All of the trajectories use the same departure CR3BP arc, which is the Sun-Earth halo unstable manifold with the largest apoapsis, shown in Figure 4.8. Similarly, all of the trajectories use the same Sun-Mars halo stable manifold with the smallest periapsis as the arrival CR3BP arc, shown in Figure 4.9. In both figures, the trajectory is propagated and displayed to the edge of the sphere of influence. In between, the departure and arrival conic arcs are determined by the osculating Keplerian orbital elements when the manifolds reach their respective SoIs and the bridge conic arc joins them as described above.



**Figure 4.8.** MMAT departure CR3BP arc in the Sun-Earth barycentric rotating frame.

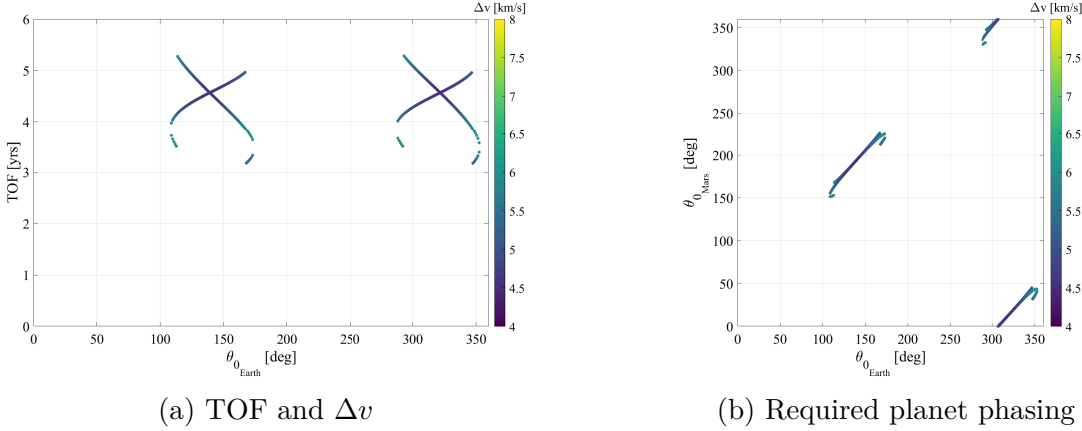
In Figure 4.10(a), the times-of-flight and maneuver magnitudes of the family members are shown with respect to their initial phasing. Note that there are areas of initial epochs where transfers could not be computed because the inequality in Equation (4.7) was not satisfied with those orientations. Each successful epoch also has two transfer solutions corresponding to the two arrival phasing solutions described above. The two groups of transfers in the figure correspond to the solutions where  $n = 0$  or  $n = 1$  satisfy Equation (4.7) and are similar due to the symmetry of the possible bridge conic orientations for an intersection. The full time-of-flight for the transfers is generally bounded between 3 and 5.5 years, while the magnitude of the two maneuvers combined is between 4 and 6 km/s.

Figure 4.10(b) shows the same transfers, now with the required initial Mars phasing  $\theta_{0_{Mars}}$ . This plot can be used to associate each transfer with an actual launch date where the Earth and Mars are in the specified locations in their respective orbits. Varying the chosen manifold departure arc while keeping the initial epoch fixed creates families that would appear as vertical lines in Figure 4.10(b), providing additional launch date flexibility but potentially at the cost of maneuver  $\Delta v$ .



**Figure 4.9.** MMAT arrival CR3BP arc in the Sun-Mars barycentric rotating frame.

The minimum- $\Delta v$  transfer from this family is shown in Figure 4.11. The total TOF of the transfer is 1670 days or 4.57 years, with a total  $\Delta v$  of 4.537 km/s. In the figure, the various arcs of the MMAT method are color-coded and the maneuvers are marked at the beginning and end of the bridge conic arc. Note that the magenta departure CR3BP arc and the blue arrival CR3BP arc are the same trajectories from Figure 4.8 and Figure 4.9 respectively, just portrayed in the inertial frame. This transfer can be compared with the minimum-TOF transfer in Figure 4.12. This transfer has a different initial epoch, which shifts all of the arcs, and a much shorter arrival conic arc. The total TOF has decreased to 1160 days or 3.18 years, but the  $\Delta v$  has increased to 5.298 km/s. Note that the first maneuver has the same magnitude; the increase comes from the second maneuver where the minimum-TOF burn is less tangential to the bridge arc than the minimum- $\Delta v$  burn to shorten the arrival conic arc time-of-flight. All of the other transfers in this family have similar geometries and characteristics.



**Figure 4.10.** Evolution along the MMAT family continued by the initial epoch.

### 4.3 End-to-End Transfers

All of the transfers used in this investigation arrive into the same Sun-Mars northern halo orbit ( $JC = 3.0001857$ ) using the smallest periapsis stable manifold as the MMAT example in Figure 4.9. The end-to-end methodology for constructing both categories of transfers is as follows:

#### 4.3.1 "Direct" Transfers

1. Starting from the Earth-Moon CR3BP departure orbit, both unstable half-manifolds are propagated to the edge of the Earth's SoI (ignoring those that crash into the Earth or Moon), where they are transformed into heliocentric inertial states and propagated under Keplerian dynamics. This is repeated for several different epochs during January 2026.
2. Each of these feasible manifold arcs then serves as a departure CR3BP arc and departure conic arc for the MMAT methodology introduced in Section 4.2. If they meet the MMAT inequality constraint (Equation (4.7)), then they produce two end-to-end "direct" transfers between an Earth-Moon and Sun-Mars orbit.

An example "direct" transfer is shown in Figure 4.13 and Figure 4.14. The departure CR3BP arc originates from an Earth-Moon northern  $L_2$  halo with a Jacobi constant of

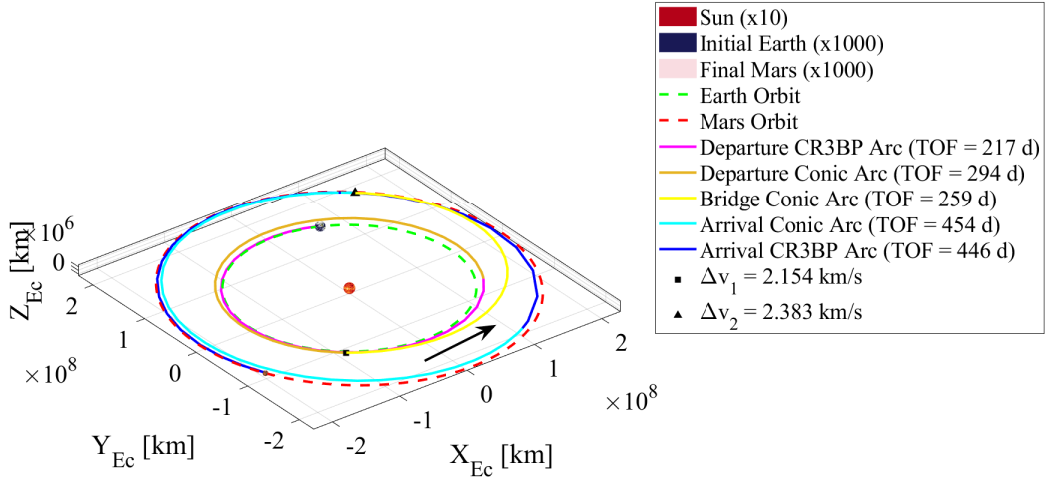


**Figure 4.11.** Minimum- $\Delta v$  MMAT in the Sun-centered Ecliptic J2000 frame.

3.13 in Figure 4.13(a), shown in the Earth-Moon rotating frame, and continues under the Sun-Earth dynamics "directly" until it reaches the Earth SoI in Figure 4.13(b). While two transfers can be computed, only one is shown in Figure 4.14.

Note that this trajectory is not optimized, nor is it the minimum-TOF or minimum- $\Delta v$  solution in the MMAT family originating from that Earth-Moon departure orbit. This particular "direct" transfer has a total maneuver cost of 5.544 km/s with a total time-of-flight of 3.26 years.

### 4.3.2 Transfers with Staging Orbit

- Starting from the Earth-Moon CR3BP departure orbit, a near-ballistic transfer to a Sun-Earth northern halo orbit is computed using the methodology introduced in Section 4.1. The particular Sun-Earth halo is free to change to decrease the  $\Delta v$  of this maneuver. This sets the initial epoch of the transfer.

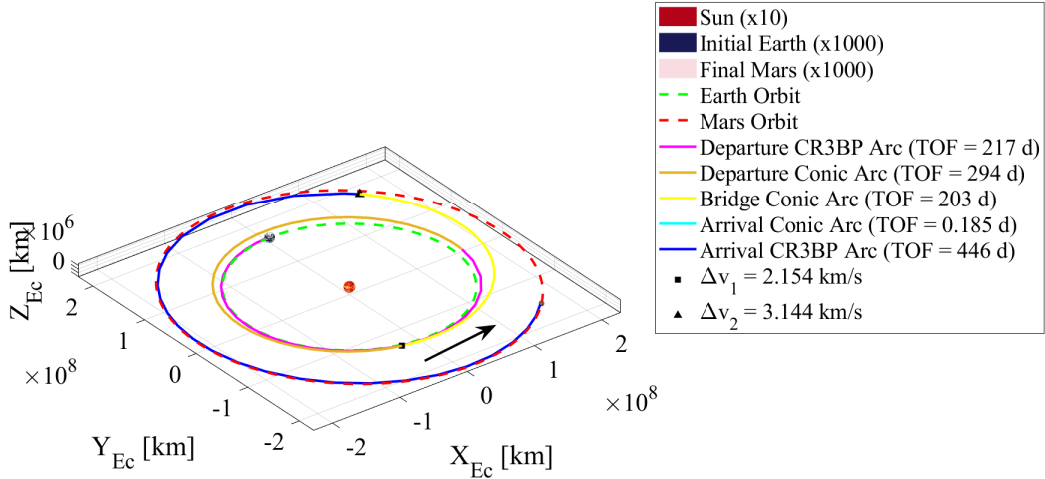
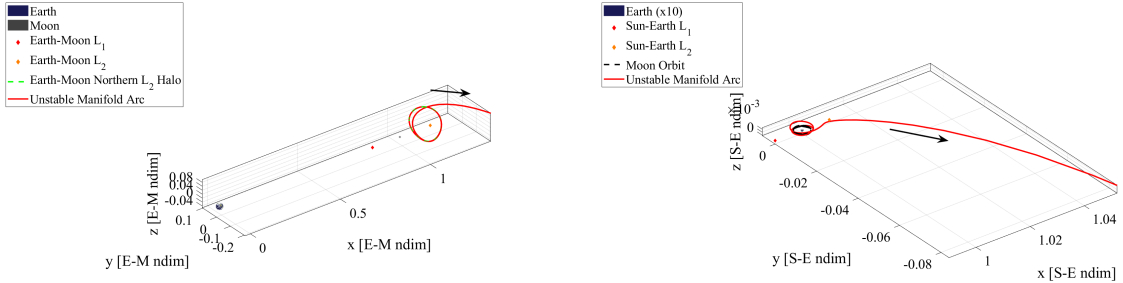


**Figure 4.12.** Minimum-TOF MMAT in the Sun-centered Ecliptic J2000 frame.

2. Once in the Sun-Earth orbit, since the phase along the orbit is determined by the arrival onto the orbit, unstable manifold arcs of the Sun-Earth halo are propagated to the edge of the Earth's SoI according to the time-correspondent location along the orbit. Each departure CR3BP arc is then associated with a departure epoch from the Sun-Earth orbit.
3. Now similar to the "direct" transfers, these arcs serve as a departure CR3BP arc and departure conic arc for the MMAT methodology (Section 4.2). This produces two end-to-end transfers between an Earth-Moon and Sun-Mars orbit with an intermediate staging Sun-Earth halo orbit for each feasible manifold arc.

Figure 4.15-Figure 4.17 show a sample transfer with an intermediate Sun-Earth staging halo orbit. The departure from the Earth-Moon orbit in Figure 4.15 is similar to the "direct" transfer example, using the same  $L_2$  orbit. However, a different manifold arc is used for this particular transfer. The near-ballistic transfer is shown in Figure 4.16, where the Earth-Moon orbit is connected to the Sun-Earth northern halo orbit. The departure CR3BP arc is



(a) Earth-Moon barycentric rotating frame. (b) Sun-Earth barycentric rotating frame.

**Figure 4.13.** "Direct" departure CR3BP arc.

also shown leaving this orbit along the unstable manifold, which is then used in the MMAT in Figure 4.17. Once again, this is not an optimized or minimum transfer in the family, with a total maneuver cost of 5.481 km/s and time-of-flight of 4.59 years.

### 4.3.3 Transfer Tradespace

As mentioned, both categories of transfers exist in families, so the solutions will have a range of total  $\Delta v$  costs and times-of-flight. Figure 4.18 shows one such tradespace for transfers originating from a  $JC = 3.13$  Earth-Moon northern  $L_2$  halo orbit (the same used for the previous examples). In the figure, the red points represent the family of transfers that include a staging orbit, while the blue points represent the family of "direct" transfers. The black "Hohmann" transfer line serves as a  $\Delta v$  baseline for comparison (this will be detailed further in the following section).

## 4.4 Keplerian Hohmann Transfer

Since the orbits of Earth and Mars are assumed to be circular in this investigation, the lowest maneuver cost transfer between the two bodies using Keplerian dynamics is a Hohmann transfer, shown in Figure 4.19. However, this only applies if the orbits are coplanar. Hence, a plane change maneuver must be introduced to account for the difference in the orbital planes. These inclination change maneuvers are cheapest at apoapsis, so this is

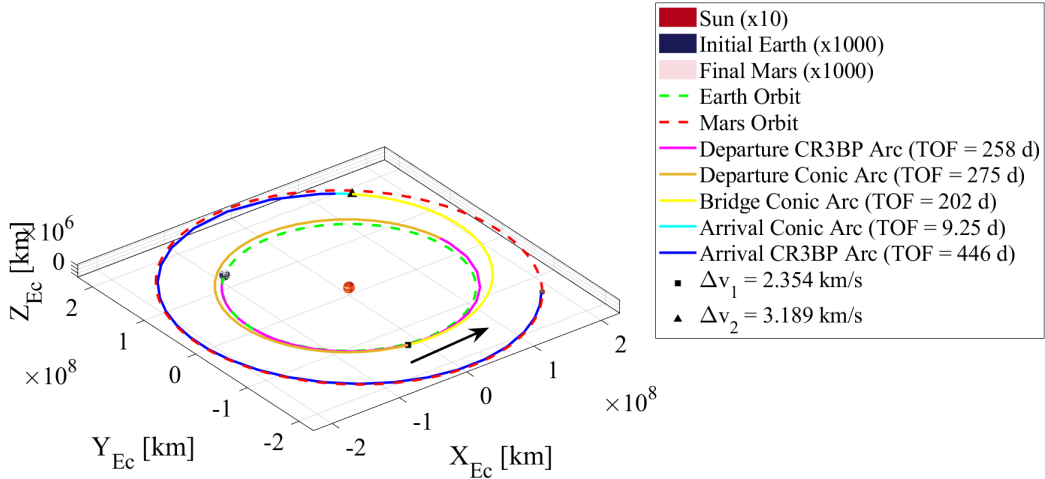


**Figure 4.14.** "Direct" MMAT in the Sun-centered Ecliptic J2000 frame.

achieved by including the plane change in the maneuver cost of the second Hohmann burn ( $\Delta v_2$  in Figure 4.19) to form a modified Hohmann transfer that serves as the baseline  $\Delta v$  cost for direct transfers between Earth and Mars.

To serve as a baseline transfer between cislunar orbits and a Sun-Mars  $L_1$  halo orbit for this investigation, a Hohmann transfer between the Earth's orbit (assumed circular at a radius of  $1.49598 \times 10^8$ ) and the Sun-Mars  $L_1$  distance ( $2.26858 \times 10^8$ ) is constructed. The following equations are used to calculate the modified Hohmann transfer combined with a plane change:

$$\Delta v_1 = \sqrt{\frac{\mu_{2BP}}{r_1}} \left( \sqrt{\frac{2r_2}{r_1 + r_2}} - 1 \right), \quad (4.20)$$

$$\Delta v_2 = \sqrt{v_H^2 + v_2^2 - 2v_H v_2 \cos \Delta i}, \quad (4.21)$$

$$v_H = \sqrt{\frac{\mu_{2BP}}{r_2} \left( \frac{2r_1}{r_1 + r_2} \right)}, \quad (4.22)$$

$$v_2 = \sqrt{\frac{\mu_{2BP}}{r_2}}, \quad (4.23)$$

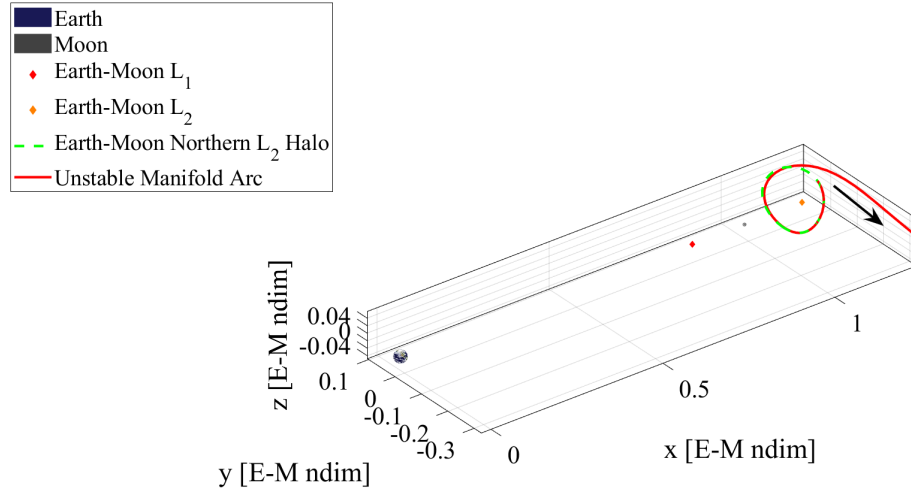


**Figure 4.15.** Departure unstable manifold arc in the Earth-Moon barycentric rotating frame.

where  $\Delta v_1$  and  $\Delta v_2$  are the two burns of the transfer,  $\mu_{2BP}$  is the Sun's gravitational parameter,  $r_1$  and  $r_2$  are the Earth's orbit and Sun-Mars  $L_1$  radii, respectively,  $v_H$  is the velocity at apoapsis of the Hohmann transfer ellipse,  $v_2$  is the circular velocity at Sun-Mars  $L_1$ , and  $\Delta i$  is the difference in inclination between the two planes. This results in a total  $\Delta v$  for the modified Hohmann transfer of 5.639 km/s. This value can be directly compared to the total maneuver costs of the two categories of transfers developed in this investigation to find lower-cost transfers.

As stated previously, the minimum-cost modified Hohmann transfer has the plane change maneuver occur at the apoapsis of the transfer ellipse. This also implies that the lowest cost MMAT transfers occur when the second burn is located at the apoapsis of the bridge conic arc. The TOF of the Hohmann transfer arc can be calculated analytically:

$$TOF = \pi \sqrt{\frac{(r_1 + r_2)^2}{7\mu_{2BP}}}, \quad (4.24)$$

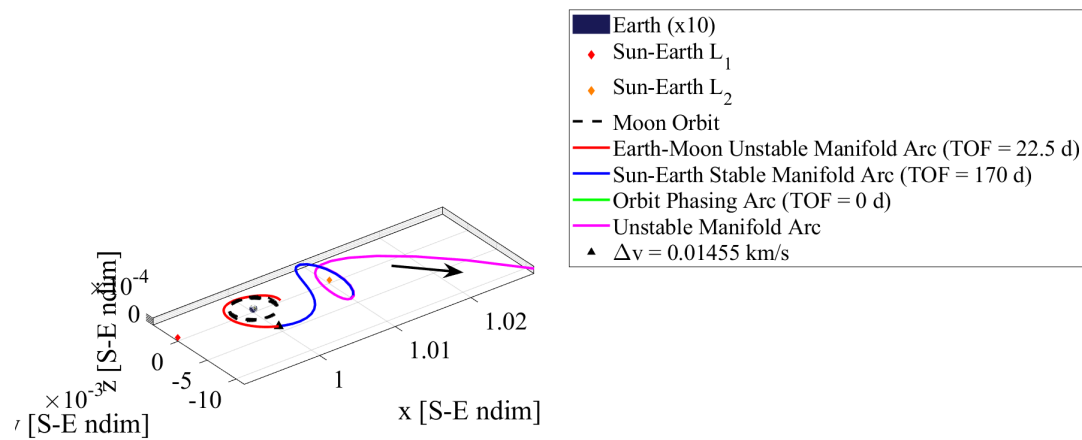


**Figure 4.16.** Departure CR3BP arc with staging orbit in the Sun-Earth barycentric rotating frame.

which is analogous to the times-of-flight of the MMAT bridge conic arcs. The minimum- $\Delta v$  transfer has a TOF of 258 days.

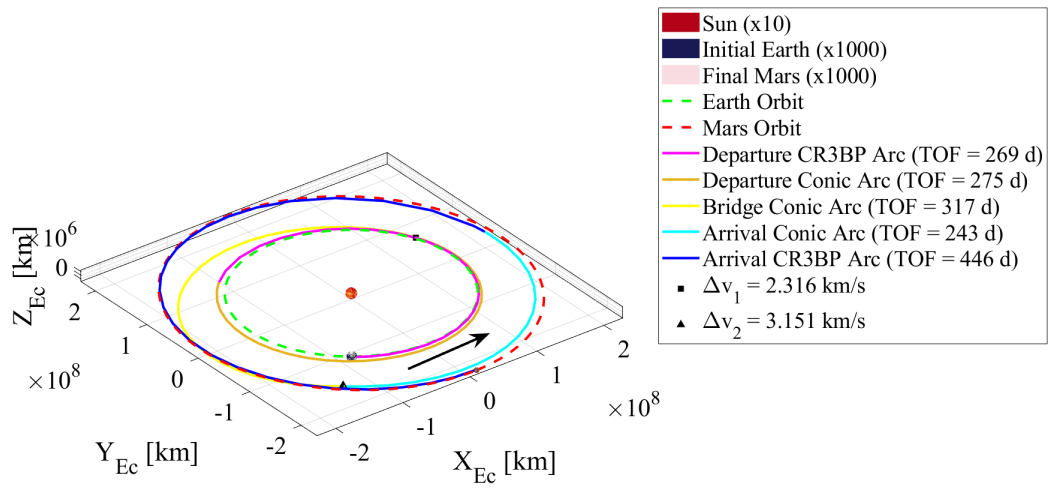


**Figure 4.17.** MMAT with staging orbit in the Sun-centered Ecliptic J2000 frame.

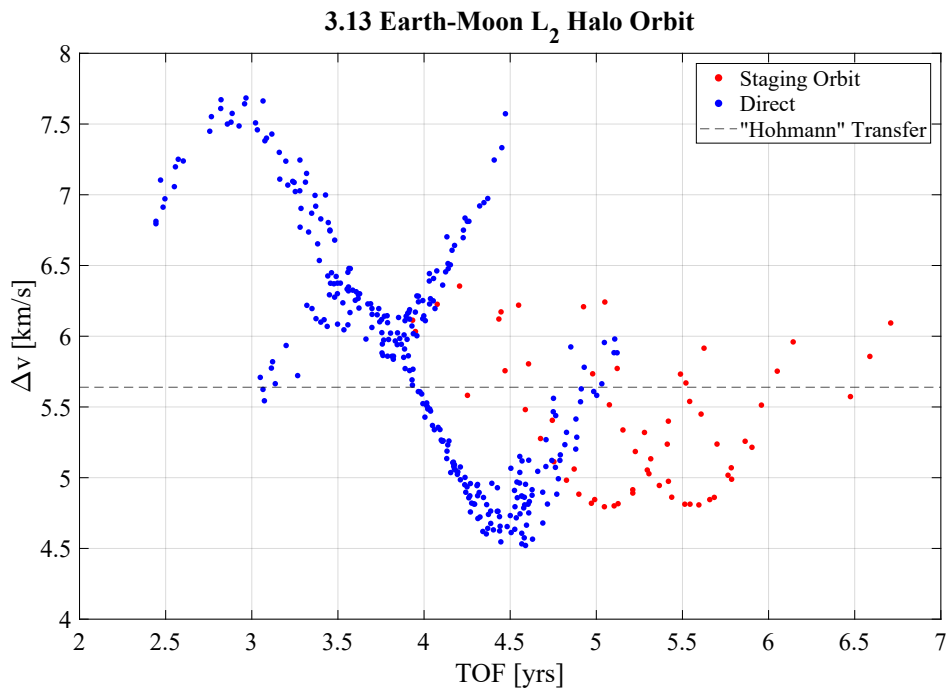


**Figure 4.18.** Tradespace of both solution categories originating from the same Earth-Moon departure orbit.

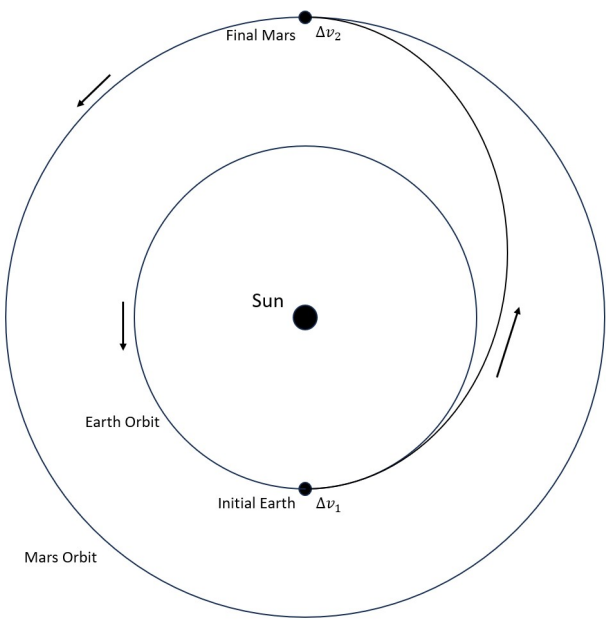


**Figure 4.19.** Hohmann transfer between Earth and Mars.

## 5. CISLUNAR DEPARTURE ORBIT COMPARISON

The two approaches introduced in the previous chapter for designing end-to-end transfers from the cislunar region to Mars are used to generate families of transfers from various departure periodic orbits in Earth-Moon CR3BP unstable families. For given departure orbits, the transfers that stage in an intermediate Sun-Earth halo orbit are compared to the "direct" transfers to determine the usefulness of a staging orbit. A cost function is introduced to select desirable transfers in each family. Then these are compared across the various cislunar departure orbits to analyze trends in the departure characteristics across orbit families and energy levels. Finally, the maneuver  $\Delta v$  and TOF costs of the transfer strategies developed in this investigation are compared to existing literature and methodologies to show that this approach reduces the maneuver costs for a Mars mission.

### 5.1 Comparing Transfers via Intermediate Sun-Earth Halos to Direct Transfers

Just like the example tradespace provided in Section 4.3.3, with Figure 4.18, for a given cislunar departure orbit, the "direct" transfers are compared to those that stage in an intermediate Sun-Earth unstable halo orbit. Tradespaces for all of the departure orbits used in this investigation are provided in Appendix A, but a few will be introduced in this section to better facilitate the comparison.

In all of the cases examined in this investigation, the family of "direct" transfers overall has lower times-of-flight than the staging transfers. As an example, in Figure 4.18, the blue points representing the "direct" transfers mostly lie to the left of the red transfers that utilize a staging orbit. The transfers with the lowest times-of-flight generally have much higher  $\Delta v$  costs, but there are some cases where the  $\Delta v$  lies below the baseline of the "Hohmann" transfer.

#### 5.1.1 Cost Function

In the example of Figure 4.18, the "direct" transfer family also contains the minimum- $\Delta v$  solutions, which also have lower times-of-flight than the staging orbit transfers. However,

this is not always the case, as shown in Figure 5.1. As a result, often a choice needs to be made balancing TOF and maneuver  $\Delta v$  cost. A cost function can help select desirable transfers that balance these two parameters.

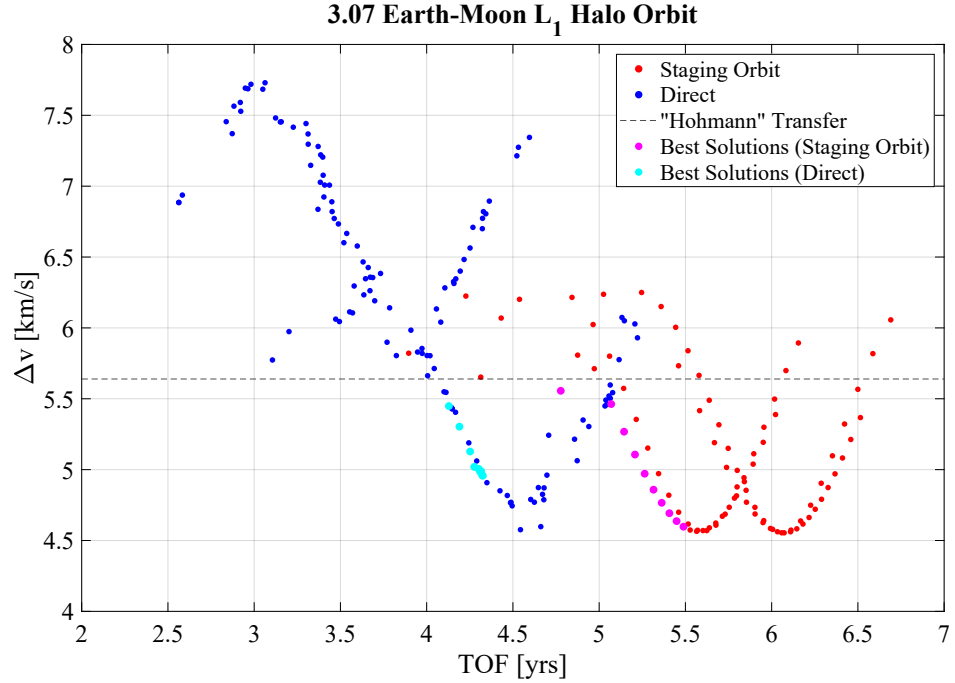


**Figure 5.1.** Transfer tradespace departing from an Earth-Moon  $L_1$  northern halo orbit ( $JC = 3.07$ ).

If total TOF and total maneuver  $\Delta v$  are considered to have units of years and km/s, respectively, then these values have similar orders of magnitude for these transfers. Therefore, an appropriate cost function needs to place weights on the two parameters depending on desired transfer characteristics that are mission-dependent:

$$J = \alpha T\text{OF} + \beta \Delta v, \quad (5.1)$$

where  $J$  is the cost function value and  $\alpha$  and  $\beta$  are design variables to adjust the cost function.  $\alpha$  and  $\beta$  can be adjusted to put higher priority on TOF or  $\Delta v$ , depending on the particular application. This investigation uses  $\alpha = 5$  and  $\beta = 2$  to prioritize lower TOF while still looking for decreased maneuver costs. This cost function is applied to the transfers in the tradespace that are below the "Hohmann" transfer  $\Delta v$  baseline, and the ten transfers from

each transfer category that have the lowest  $J$ -value are determined to be the best transfers for this application. For the case of the  $L_1$  halo with  $J_C = 3.07$  in Figure 5.1, these are the cyan ("direct") and magenta ("staging") points.

### 5.1.2 Comparison of Selected Transfers

In Figure 5.1, among the transfers selected using the cost function, the "direct" options still have lower times-of-flight, while the transfers with staging orbits achieve lower  $\Delta v$  costs. This contrasts with the earlier example from Figure 4.18, now shown with the best solutions from the cost function in Figure 5.2, where the "direct" options have both lower times-of-flight and maneuver costs.

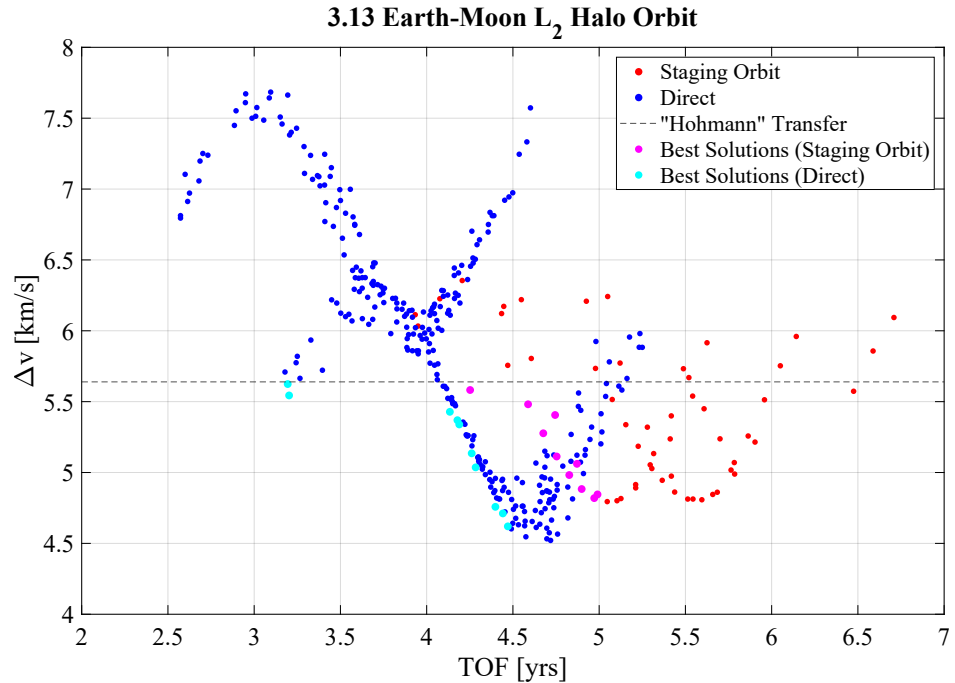


**Figure 5.2.** Transfer tradespace departing from an Earth-Moon  $L_2$  northern halo orbit ( $J_C = 3.13$ ).

## 5.2 Comparing Cislunar Departure Families

### 5.3 Comparison to Previous Work

## **6. CONCLUSION**

## REFERENCES

- [1] B. R. Zamora, *Gateway Space Station*, 2024. [Online]. Available: <https://www.nasa.gov/reference/gateway-about/>.
- [2] National Aeronautics and Space Administration, *NASA Strategic Plan 2022*, 2022. [Online]. Available: <https://www.nasa.gov/wp-content/uploads/2023/09/fy-22-strategic-plan-1.pdf?emrc=ff1a1e>.
- [3] National Aeronautics and Space Administration, *Moon to Mars Objectives September 2022*, 2022. [Online]. Available: <https://www.nasa.gov/wp-content/uploads/2022/09/m2m-objectives-exec-summary.pdf?emrc=119caf>.
- [4] B. G. Drake, “Human exploration of Mars design reference architecture 5.0,” NASA Lyndon B. Johnson Space Center, Tech. Rep., 2009. [Online]. Available: <https://www.ecosia.org/search?addon=chrome&addonversion=6.0.3&q=human%20exploration%20of%20mars%20design%20reference%20architecture>.
- [5] W. S. Koon, M. W. Lo, J. E. Marsden, and S. D. Ross, “Heteroclinic connections between periodic orbits and resonance transitions in celestial mechanics,” *Chaos: An Interdisciplinary Journal of Nonlinear Science*, vol. 10, no. 2, pp. 427–469, 2000. DOI: [10.1063/1.166509](https://doi.org/10.1063/1.166509).
- [6] D. F. Landau and J. M. Longuski, “Trajectories for human missions to Mars, Part 1: Impulsive transfers,” *Journal of Spacecraft and Rockets*, vol. 43, no. 5, pp. 1035–1042, 2006. DOI: [10.2514/1.18995](https://doi.org/10.2514/1.18995).
- [7] S. Fritz and K. Turkoglu, “Optimal trajectory determination and mission design for asteroid/deep space exploration via multi-body gravity assist maneuvers,” in *2016 IEEE Aerospace Conference*, Big Sky, Montana, USA, 2016.
- [8] J. Barrow-Green, *Poincaré and the Three Body Problem*. Providence, Rhode Island, USA: American Mathematical Society, 1997.
- [9] R. Farquhar, D. Muhonen, and L. C. Church, “Trajectories and orbital maneuvers for the ISEE-3/ICE comet mission,” in *AIAA/AAS Astrodynamics Conference*, Seattle, Washington, USA, 1984.

- [10] M. W. Lo, B. G. Williams, W. E. Bollman, *et al.*, “Genesis mission design,” *The Journal of the Astronautical Sciences*, vol. 49, no. 1, pp. 169–184, 2001. DOI: [10.1007/BF03546342](https://doi.org/10.1007/BF03546342).
- [11] M. Woodard, D. Folta, and D. Woodfork, “ARTEMIS: The first mission to the lunar libration orbits,” in *21st International Symposium on Space Flight Dynamics*, Toulouse, France, 2009.
- [12] B. Cheetham, T. Gardner, and A. Forsman, “Cislunar Autonomous Positioning System Technology Operations and Navigation Experiment (CAPSTONE),” in *ASCEND 2021*, 2021.
- [13] K. K. Boudad, K. C. Howell, and D. C. Davis, “Departure and escape dynamics from the near rectilinear halo orbits in the Earth-Moon-Sun system,” *The Journal of the Astronautical Sciences*, vol. 69, pp. 1076–1114, 2022. DOI: [10.1007/s40295-022-00328-w](https://doi.org/10.1007/s40295-022-00328-w).
- [14] E. M. Zimovan-Spreen, “Dynamical structures nearby NRHOs with applications to transfer design in cislunar space,” *The Journal of the Astronautical Sciences*, vol. 69, pp. 718–744, 2022. DOI: [10.1007/s40295-022-00320-4](https://doi.org/10.1007/s40295-022-00320-4).
- [15] A. Miele and T. Wang, “Optimal transfers from an Earth orbit to a Mars orbit,” *Acta Astronautica*, vol. 45, no. 3, pp. 119–133, 1999. DOI: [10.1016/S0094-5765\(99\)00109-5](https://doi.org/10.1016/S0094-5765(99)00109-5).
- [16] D. Conte, M. Di Carlo, H. Koki, D. B. Spencer, and M. Vasile, “Earth-Mars transfers through Moon distant retrograde orbits,” *Acta Astronautica*, vol. 143, pp. 372–379, 2017. DOI: [10.1016/j.actaastro.2017.12.007](https://doi.org/10.1016/j.actaastro.2017.12.007).
- [17] J. Esper and B. Aldrin, “Mars small-spacecraft human exploration resource prospector with aero-braking (SHERPA): Demonstrating an end-to-end mission to Phobos distant retrograde orbit,” in *International Astronautical Conference (IAC) 2019*, Washington, D.C., USA, 2019.
- [18] F. Topputo, M. Vasile, and F. Bernelli-Zazzera, “Low energy interplanetary transfers exploiting invariant manifolds of the restricted three-body problem,” *The Journal of the Astronautical Sciences*, vol. 53, no. 4, pp. 353–372, 2005. DOI: [10.1007/BF03546358](https://doi.org/10.1007/BF03546358).

- [19] M. Nakamiya, H. Yamakawa, D. J. Scheeres, and M. Yoshikawa, “Interplanetary transfers between halo orbits: Connectivity between escape and capture trajectories,” *Journal of Guidance, Control, and Dynamics*, vol. 33, no. 3, pp. 803–813, 2010. DOI: [10.2514/1.46446](https://doi.org/10.2514/1.46446).
- [20] S. Haibin, W. Shuai, and C. Pingyuan, “Fast low-energy halo-to-halo transfers between Sun-planet systems,” *Chinese Journal of Aeronautics*, vol. 27, no. 2, pp. 338–348, 2014. DOI: [10.1016/j.cja.2014.02.005](https://doi.org/10.1016/j.cja.2014.02.005).
- [21] M. Kakoi, K. C. Howell, and D. Folta, “Access to Mars from Earth-Moon libration point orbits: Manifold and direct options,” *Acta Astronautica*, vol. 102, pp. 269–286, 2014. DOI: [10.1016/j.actaastro.2014.06.010](https://doi.org/10.1016/j.actaastro.2014.06.010).
- [22] I. Cavallari, R. Petitdemange, and S. Lizy-Destrez, “Transfer from a lunar distant retrograde orbit to Mars through Lyapunov orbits,” in *International Symposium on Space Flight Dynamics*, Melbourne, Australia, 2019.
- [23] E. Scantamburlo, M. Guzzo, and R. I. Paez, “Interplanetary transfers using stable and unstable manifold tubes originating at L1 and L2 in the elliptic restricted three-body problems,” *Acta Astronautica*, vol. 200, pp. 97–110, 2022. DOI: [10.1016/j.actaastro.2022.07.036](https://doi.org/10.1016/j.actaastro.2022.07.036).
- [24] D. Canales, K. C. Howell, and E. Fantino, “Transfer design between neighborhoods of planetary moons in the circular restricted three-body problem: The moon-to-moon analytical transfer method,” *Celestial Mechanics and Dynamical Astronomy*, vol. 133, no. 36, pp. 1–44, 2021. DOI: [10.1007/s10569-021-10031-x](https://doi.org/10.1007/s10569-021-10031-x).
- [25] D. Canales, K. C. Howell, and E. Fantino, “A versatile moon-to-moon transfer design methodology for applications involving libration point orbits,” *Acta Astronautica*, vol. 198, pp. 388–402, 2022. DOI: [10.1016/j.actaastro.2022.06.010](https://doi.org/10.1016/j.actaastro.2022.06.010).
- [26] Y. Lu, H. Li, J. Che, Y. Yang, Y. Yang, and Y. Sun, “Design and optimization of low-energy transfer orbit to Mars with multi-body environment,” *Science China*, vol. 58, no. 10, pp. 1660–1671, 2015. DOI: [10.1007/s11431-015-5847-7](https://doi.org/10.1007/s11431-015-5847-7).
- [27] Y. Shimane and K. Ho, “Gravity-assist low-thrust inter-system trajectory design with manifold captures,” *The Journal of the Astronautical Sciences*, vol. 69, pp. 193–217, 2022. DOI: [10.1007/s40295-022-00319-x](https://doi.org/10.1007/s40295-022-00319-x).

- [28] S. K. Singh and K. Negi, “Earth-Mars halo to halo low thrust manifold transfers using variable specific impulse engine,” *Acta Astronautica*, vol. 220, pp. 1–11, 2024. DOI: [10.1016/j.actaastro.2024.03.049](https://doi.org/10.1016/j.actaastro.2024.03.049).
- [29] J. J. Masdemont, G. Gomez, L. Lei, and H. Peng, “Global analysis of direct transfers from lunar orbits to Sun-Earth libration point regimes,” *Celestial Mechanics and Dynamical Astronomy*, vol. 133, no. 15, 2021. DOI: [10.1007/s10569-021-10011-1](https://doi.org/10.1007/s10569-021-10011-1).
- [30] Q. Guo and H. Lei, “Families of Earth-Moon trajectories with applications to transfers towards Sun-Earth libration point orbits,” *Astrophysics and Space Science*, vol. 364, no. 43, 2019. DOI: [10.1007/s10509-019-3532-1](https://doi.org/10.1007/s10509-019-3532-1).
- [31] A. Pasquale, M. Lavagna, and F. Renk, “Cislunar escape trajectories through patched Sun-Earth/Earth-Moon three-body problem,” in *72nd International Astronautical Congress*, Dubai, UAE, 2021.
- [32] K. Boudad, K. Howell, and D. Davis, “Energy and phasing considerations for low-energy transfers from cislunar to heliocentric space,” in *31st AAS/AIAA Spaceflight Mechanics Meeting*, Charlotte, North Carolina, USA, 2021.
- [33] D. C. Garcia, “Transfer design methodology between neighborhoods of planetary moons in the circular restricted three-body problem,” Ph.D. Dissertation, Purdue University, West Lafayette, IN, USA, 2021.
- [34] M. Kakoi, “Design of transfers from Earth-Moon  $L_1/L_2$  libration point orbits to a destination object,” Ph.D. Dissertation, Purdue University, West Lafayette, IN, USA, 2015.
- [35] B. Semenov, *SPICE: An observation geometry system for space science missions*, 2023. [Online]. Available: <https://naif.jpl.nasa.gov/naif/>.
- [36] D. A. Vallado, *Fundamentals of Astrodynamics and Applications*, Fourth Edition. Hawthorne, CA, USA: Microcosm Press, 2013.
- [37] E. M. Zimovan, “Characteristics and design strategies for near rectilinear halo orbits within the Earth-Moon system,” M.S. Thesis, Purdue University, West Lafayette, IN, USA, 2017.
- [38] K. K. Boudad, “Disposal dynamics from the vicinity of near rectilinear halo orbits in the Earth-Moon-Sun system,” M.S. Thesis, Purdue University, West Lafayette, IN, USA, 2018.

- [39] D. J. Scheeres, “The restricted Hill four-body problem with applications to the Earth-Moon-Sun system,” *Celestial Mechanics and Dynamical Astronomy*, vol. 70, pp. 75–98, 1998. DOI: [10.1023/A:1026498608950](https://doi.org/10.1023/A:1026498608950).
- [40] M. A. Andreu, “Dynamics in the center manifold around L2 in the quasi-bicircular problem,” *Celestial Mechanics and Dynamical Astronomy*, vol. 84, pp. 105–133, 2002. DOI: [10.1023/A:1019979414586](https://doi.org/10.1023/A:1019979414586).
- [41] J. S. Parker and R. L. Anderson, *Low-Energy Lunar Trajectory Design*. Pasadena, CA, USA: NASA Jet Propulsion Laboratory, 2013.
- [42] R. Park, *Three-body periodic orbits*. [Online]. Available: [https://ssd.jpl.nasa.gov/tools/periodic\\_orbits.html](https://ssd.jpl.nasa.gov/tools/periodic_orbits.html).
- [43] E. M. Zimovan Spreen, “Trajectory design and targeting for applications to the exploration program in cislunar space,” Ph.D. Dissertation, Purdue University, West Lafayette, IN, USA, 2021.
- [44] R. J. Power, “Characterization of lunar access relative to cislunar orbits,” M.S. Thesis, Purdue University, West Lafayette, IN, USA, 2019.
- [45] M. Gupta, “Finding order in chaos: Resonant orbits and Poincaré sections,” M.S. Thesis, Purdue University, West Lafayette, IN, USA, 2020.
- [46] N. I. Sadaka, “There and back again: Generating repeating transfers using resonant structures,” M.S. Thesis, Purdue University, West Lafayette, IN, USA, 2023.
- [47] L. Perko, *Differential Equations and Dynamical Systems*, Third Edition. New York City, NY, USA: Springer, 1991.
- [48] D. Guzzetti, E. M. Zimovan, K. C. Howell, and D. C. Davis, “Stationkeeping analysis for spacecraft in lunar near rectilinear halo orbits,” in *27th AAS/AIAA Space Flight Mechanics Meeting*, 2017.

## A. End-to-End Transfer Tradespaces

### A.1 Lyapunov Orbits

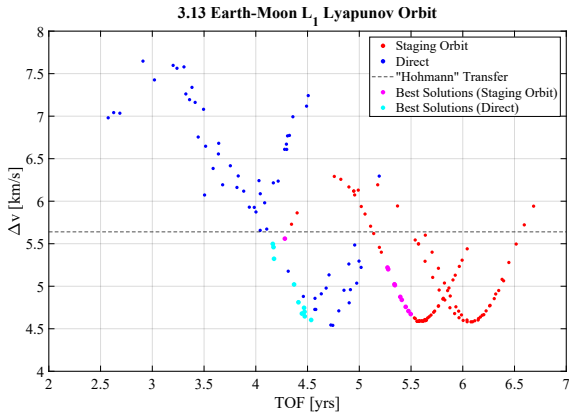


**Figure A.1.** Transfer tradespace departing from an Earth-Moon  $L_1$  Lyapunov orbit ( $JC = 3.13$ ).

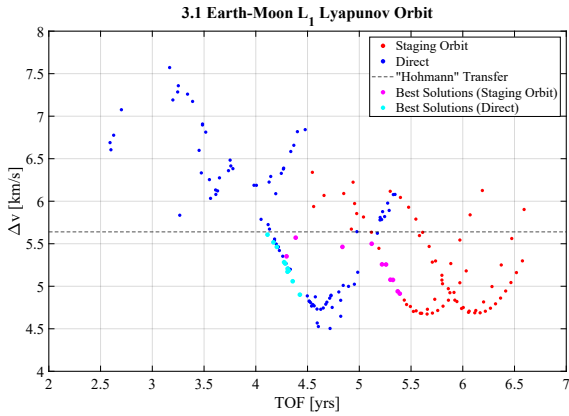


**Figure A.2.** Transfer tradespace departing from an Earth-Moon  $L_1$  Lyapunov orbit ( $JC = 3.1$ ).

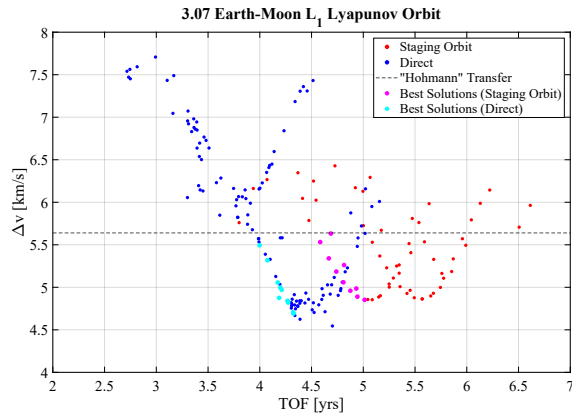


**Figure A.3.** Transfer tradespace departing from an Earth-Moon  $L_1$  Lyapunov orbit ( $JC = 3.07$ ).

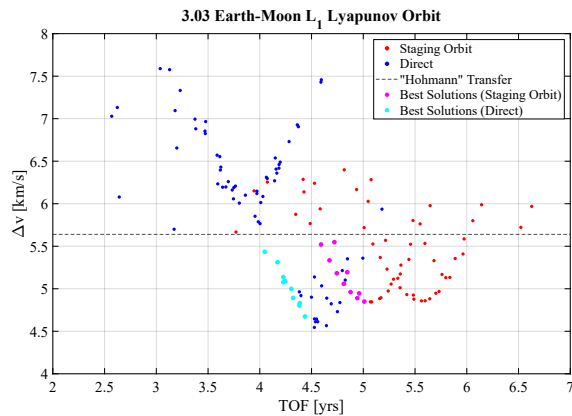


**Figure A.4.** Transfer tradespace departing from an Earth-Moon  $L_1$  Lyapunov orbit ( $JC = 3.03$ ).

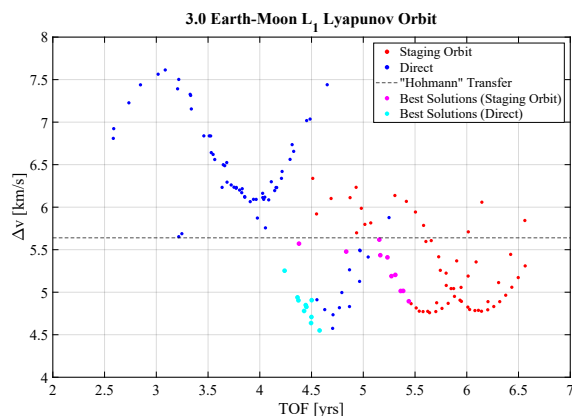


**Figure A.5.** Transfer tradespace departing from an Earth-Moon  $L_1$  Lyapunov orbit ( $JC = 3.0$ ).

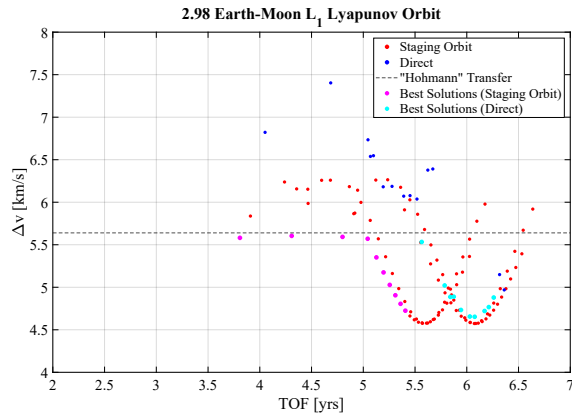


**Figure A.6.** Transfer tradespace departing from an Earth-Moon  $L_1$  Lyapunov orbit ( $JC = 2.98$ ).

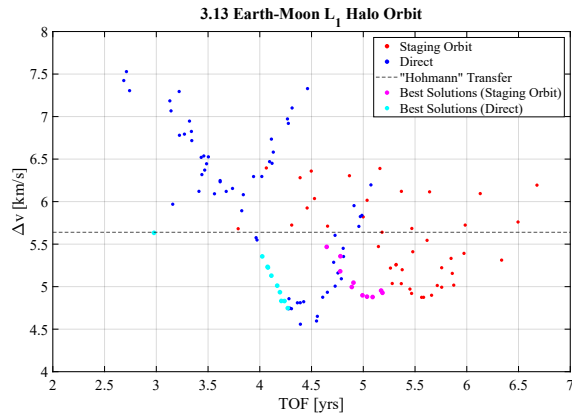


**Figure A.7.** Transfer tradespace departing from an Earth-Moon  $L_1$  northern halo orbit ( $JC = 3.13$ ).

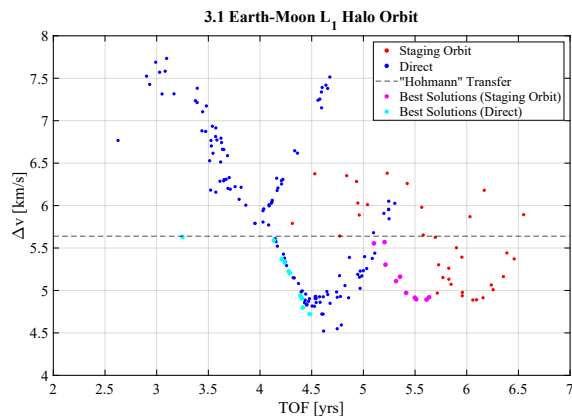


**Figure A.8.** Transfer tradespace departing from an Earth-Moon  $L_1$  northern halo orbit ( $JC = 3.1$ ).

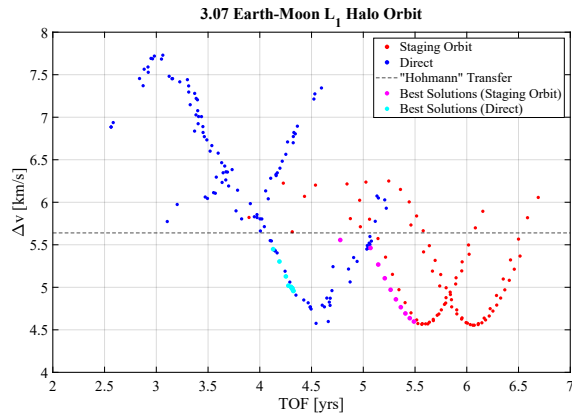


**Figure A.9.** Transfer tradespace departing from an Earth-Moon  $L_1$  northern halo orbit ( $JC = 3.07$ ).

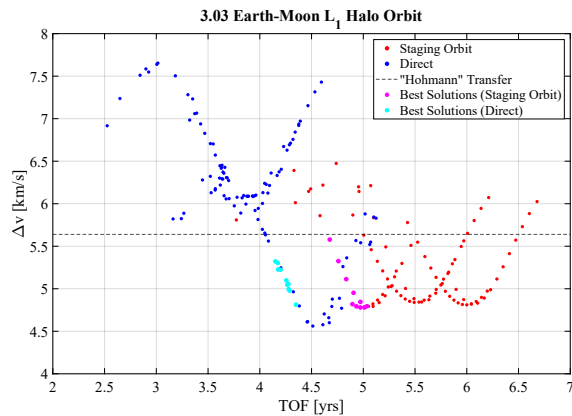


**Figure A.10.** Transfer tradespace departing from an Earth-Moon  $L_1$  northern halo orbit ( $JC = 3.03$ ).

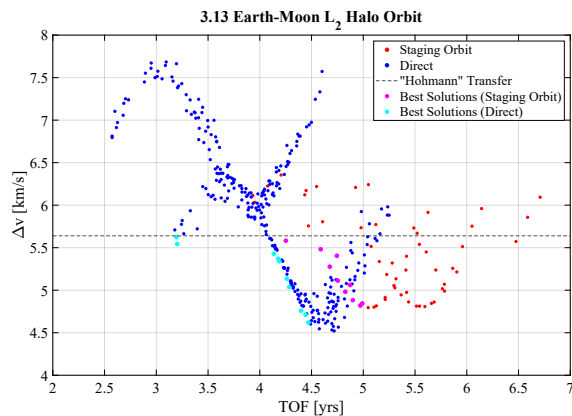


**Figure A.11.** Transfer tradespace departing from an Earth-Moon  $L_2$  northern halo orbit ( $JC = 3.13$ ).

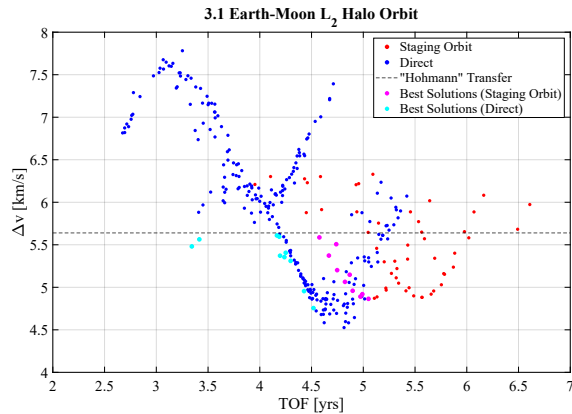


**Figure A.12.** Transfer tradespace departing from an Earth-Moon  $L_2$  northern halo orbit ( $JC = 3.1$ ).

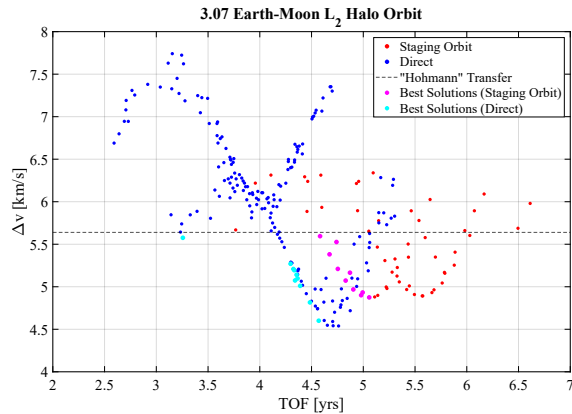


**Figure A.13.** Transfer tradespace departing from an Earth-Moon  $L_2$  northern halo orbit ( $JC = 3.07$ ).

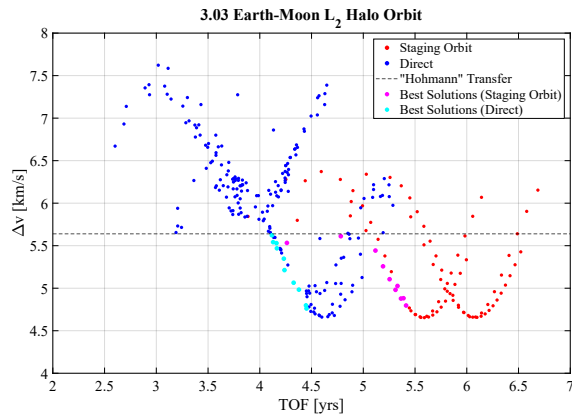


**Figure A.14.** Transfer tradespace departing from an Earth-Moon  $L_2$  northern halo orbit ( $JC = 3.03$ ).